



**STABILITY OF THE
LARGE LOW SHEAR VELOCITY PROVINCES:
NUMERICAL MODELING OF THERMOCHEMICAL
MANTLE CONVECTION**

Dissertation
zur Erlangung des Doktorgrades
“doctor rerum naturalium”
(Dr. rer. nat.)
in der Wissenschaftsdisziplin “Geophysik”

eingereicht an der
Mathematisch-Naturwissenschaftlichen Fakultät
der Universität Potsdam

vorgelegt von
Elvira Mulyukova

am März 2014

This work is licensed under a Creative Commons License:
Attribution 4.0 International
To view a copy of this license visit
<http://creativecommons.org/licenses/by/4.0/>

Published online at the
Institutional Repository of the University of Potsdam:
URN [urn:nbn:de:kobv:517-opus4-82228](http://nbn-resolving.org/urn:nbn:de:kobv:517-opus4-82228)
<http://nbn-resolving.org/urn:nbn:de:kobv:517-opus4-82228>

Acknowledgements

You know those evenings when you sit down in front of your computer, you look at the simulation results on your screen, and the simulation results look back at you as if saying: “It’s not me, it’s you”. Your finite elements are painfully deformed, their edges all crooked and cutting through their faces, markers are flying all over the place, Maxwell’s demons had a go at your thermal field, and invited their friends other demons to desecrate your velocity and compositional fields, gravity points wherever it pleases, as long as it’s not towards the center of the Earth, and the laws of physics generally don’t seem to apply to whatever magical frame of reference you’re in. Well, you think, the colormap is really pretty though... Then you close these esthetic figures and take a quick look across your shoulder, hoping not a single soul witnessed the madness on your screen.

It is especially in times like these that it really helps to know that you are not facing this awful screen on your own. First, you get a good laugh out of it with Andrey and Alexey, who will quickly point out all your embarrassing flaws as a scientist, suggest alternative career paths, but somehow end up motivating you not to give up the fight. You go home and tell Øystein to prepare for a completely unprovoked and unreasonable battle with a PhD-student in distress. Then, you pack your bags and go to Wrocław, where Marcin applies First Aid to your poor sickly code, and opens the world of opportunities for other codes that you can potentially abuse and ruin. By the time you’re back in Potsdam, you finally have a working tool that stands a chance at running models that get more than a polite smile and a ‘...hm, it’s nice, but perhaps...’ from Bernhard. If you’re really lucky, Bernhard may award you with a ‘This is interesting!’, followed by a discussion that triggers an avalanche of ideas in your brain: “so many parameters, so little time, so few CPUs...” Once Stephan enters the scene, you know this is getting serious. Your black-and-white and red-and-blue plots suddenly get all kinds of geological terminology thrown at them. Before you know it - your results look sexy and worthy of being rolled out to the public.

I have been extremely lucky with the support I got throughout this PhD-project. More than that, I got a taste of how exciting and fun it can be to do science, and I am extremely grateful for that.

...I also got a taste of how head-banging-against-the-wall frustrating science can be, and am even more grateful to Øystein, my sister and my mom for putting up with this roller-coaster, and for pulling me out of the office to see that, who would've thought, there are all kinds of other joys in life than markers correctly communicating their properties to the nodes of the finite elements.

Abstract

We study segregation of the subducted oceanic crust (OC) at the core mantle boundary and its ability to accumulate and form large thermochemical piles (such as the seismically observed Large Low Shear Velocity Provinces - LLSVPs). Our high-resolution numerical simulations suggest that the longevity of LLSVPs for up to three billion years, and possibly longer, can be ensured by a balance in the rate of segregation of high-density OC-material to the CMB, and the rate of its entrainment away from the CMB by mantle upwellings.

For a range of parameters tested in this study, a large-scale compositional anomaly forms at the CMB, similar in shape and size to the LLSVPs. Neutrally buoyant thermochemical piles formed by mechanical stirring - where thermally induced negative density anomaly is balanced by the presence of a fraction of dense anomalous material - best resemble the geometry of LLSVPs. Such neutrally buoyant piles tend to emerge and survive for at least 3Gyr in simulations with quite different parameters. We conclude that for a plausible range of values of density anomaly of OC material in the lower mantle - it is likely that it segregates to the CMB, gets mechanically mixed with the ambient material, and forms neutrally buoyant large scale compositional anomalies similar in shape to the LLSVPs.

We have developed an efficient FEM code with dynamically adaptive time and space resolution, and marker-in-cell methodology. This enabled us to model thermochemical mantle convection at realistically high convective vigor, strong thermally induced viscosity variations, and long term evolution of compositional fields.

Abstract

Stabilität der basalen Melange im untersten Erdmantel: Numerische Modellierung thermochemischer Mantelkonvektion

Es wird allgemein akzeptiert, dass Mantelkonvektion - das langsame Fließen der Mantelgesteine, das mutmaßlich ein wichtiger Antrieb der Plattentektonik ist - von Dichteunterschieden verursacht wird, die thermischen aber auch chemischen Ursprungs sind. Es fehlen aber Kenntnisse über die thermochemischen Prozesse im Erdinneren, vor allem wegen Schwierigkeiten bei der Beobachtung. Eines der zuverlässigsten Resultate von tomographischen Beobachtungen ist die Existenz von zwei Haufen einer basalen Melange (BAM, LLSVP auf Englisch), die sich auf gegenüber liegenden Seiten in 3000 km Tiefe am Boden des Mantels unter Afrika bzw dem Pazifik befinden. Die niedrige Scherwellengeschwindigkeit in der BAM scheint einen thermischen (hei) sowie einen chemischen (Material mit hoher Dichte) Ursprung zu haben. Aufgrund von plattentektonischen Rekonstruktionen wird angenommen dass die BAM langlebig und stabil sind, und dass sie von überwiegend von ihren Rändern hochquellenden Manteldiapiren beprobt werden. Die Hauptfrage meiner Doktorarbeit ist, wie solche großen chemischen Speicher wie die BAM sich bilden und über hunderte von Millionen Jahren überleben können, ohne dass sie von der Mantelkonvektion zerstört werden. Was sind die physikalischen Eigenschaften des BAM-Materials, z.B. Dichte, die dazu beitragen?

Ich benutze numerische Modellierung um zu erforschen, wie sich eine dichte Bodenschicht bildet und wie die Mantelkonvektion Material daraus mitnimmt. Mein Ziel ist, die langfristige thermochemische Entwicklung des Erdmantels zu verstehen, insbesondere die Rolle der Dichteheterogenitäten Viskosität im untersten Mantel.

Contents

1	Introduction	11
1.1	Large Low Shear Velocity Provinces: Observations and Inferences . .	11
1.2	Primordial Dense Basal Layer	13
1.3	Accumulated MORB at the CMB	14
1.4	Previous Models	16
1.5	This study	19
2	Physics of Segregation and Entrainment	23
2.1	Governing Forces	23
2.2	Large Scale	24
2.3	Small Scale	25
3	Mathematical Model	27
3.1	Mathematical Model	27
4	Numerical Modelling	33
4.1	Numerical Methodology	33
4.2	Numerical Challenges	39
4.2.1	Time-Discretization	39
4.2.2	Incompressible Stokes Equation for Multicomponent Flow . .	43
4.2.3	Thermal Advection Equation	44
4.2.4	Compositional Advection Equation	46
4.3	Communication from Markers to Grids	51
4.3.1	Voronoi Diagram and Delaunay Triangulation	51
4.3.2	Binning	55
4.3.3	Ghost Mesh Methods	58
4.3.4	Communication from Markers to Grids: Our Algorithm	70
4.4	Benchmark-Results	70
4.4.1	Rayleigh-Taylor Benchmark	70
4.4.2	Thermal Convection Benchmark	74

4.4.3	Thermochemical Convection Benchmark	78
5	Rheological Model	83
5.1	Factorization of Temperature- and Depth-Dependence of Viscosity . .	83
5.2	Radial Temperature Profile	86
5.3	Implementing Depth- and Temperature-Dependence of Viscosity . . .	88
6	Simulation Results	89
6.1	Model Description	89
6.2	Results	91
6.2.1	Global Scale Time Evolution	92
6.2.2	Pile Scale Time Evolution	106
6.2.3	Models Featuring Primitive Dense Basal Layer	112
6.3	Discussion	117
6.4	Model Limitations	121
6.4.1	Boussinesq Approximation	121
6.4.2	Cylindrical Geometry	121
6.4.3	Prescribed Surface Velocity	123
6.4.4	Internal Heating	123
6.4.5	Stress Exponent	124
6.5	Conclusions and Outlook	124

Chapter 1

Introduction

In this chapter, we present an overview of the previously published observational and modelling studies which contributed to the current understanding of the thermal and chemical composition of the Earth’s mantle. In particular, we focus on the studies which investigate the geometrical structure, material properties, and thermochemical evolution scenarios of the observed large-scale compositional anomaly in the lowermost mantle: the Large Low Shear Velocity Provinces. This overview points to some of the remaining questions about lower mantle structure and evolution, and serves as motivation for our numerical study, of which an outline is presented at the end of this chapter.

1.1 Large Low Shear Velocity Provinces: Observations and Inferences

One of the most robust results from deep seismic tomography studies is the existence of two antipodally located Large Low Shear Velocity Provinces (LLSVPs) at the base of the mantle: one beneath Africa and the other beneath the Pacific Ocean (*Garnero and McNamara, 2008; Dziewonski et al., 2010; Ritsema et al., 2011*). Reconstructions of the eruption sites of large igneous provinces (LIPs), hotspot volcanoes, and kimberlites of the last 350 Ma have shown that these project radially downward to the margins of the LLSVPs (*Torsvik et al., 2006*). This has led to inferences that plumes of arguably deep origin are generated from the margins of the LLSVPs, and that the LLSVPs are stable, long-lived and affect the geometry of flow in the deep mantle and that of plate tectonics at the surface (*Dziewonski et al., 2010*). In the remainder

of this section, we first present a brief overview of the main LLSVPs-characteristics, mainly derived from observational studies, and then an overview of the proposed models for the LLSVPs time and process of formation.

Seismic studies have shown that the boundaries between the LLSVPs and surrounding mantle are sharp, with an outward tilt (overhanging) of the edge observed for the African anomaly (*Ni et al.*, 2002). The peak height above CMB of the LLSVPs is estimated to be about 1000 – 1800 km for the African anomaly and 500 – 1400 km for the Pacific anomaly (*Burke et al.*, 2008; *Garnero and McNamara*, 2008). The upper bounds are derived according to the definition of LLSVPs as regions bounded by the -1% contour of the shear wave velocity anomaly (*Burke et al.*, 2008). This definition does not necessarily coincide with the one where LLSVPs are piles of compositionally distinct material, as will be discussed shortly. The two LLSVPs appear to cover nearly 20% of the CMB (*Burke et al.*, 2008). They get narrower with greater distance above the CMB, with their uppermost parts shaped as narrow cones (> 2 cones topping off each of the LLSVPs). According to *Burke et al.* (2008)’s definition of LLSVPs, they occupy ~ 1.6 volume % of the mantle, of which the larger African LLSVP accounts for ~ 0.9 volume %. Similarly, *Hernlund and Houser* (2008) find that the large scale robustly observed low shear waves velocity features in the lower mantle occupy about $2.0 \pm 0.4\%$ of the total mantle volume.

The negative correlation between the bulk sound and shear velocity within the LLSVPs suggests that these anomalies are of chemical origin (*Masters et al.*, 2000; *Trampert et al.*, 2004; *Steinberger and Holme*, 2008). This hypothesis is supported by the normal-mode data, which indicate an increased density in the locations of LLSVPs (*Ishii and Tromp*, 1999). Further, seismic data in conjunction with available mineral physics data, which makes it possible to discern chemical and thermal contributions to buoyancy - reveals the dominant role of chemically induced density variations in the lowermost 1000 km of the mantle (*Trampert et al.*, 2004; *Mosca et al.*, 2012). The sharp and steeply dipping edges of the African LLSVP are also best explained as compositionally controlled (*Ni et al.*, 2002). Finally, the long-term stability of LLSVPs, as inferred from geological reconstructions of eruptions caused by arrival of deep mantle plumes (*Torsvik et al.*, 2006), is, from a geodynamic point of view, more readily satisfied by their thermochemical, rather than purely thermal, origin.

Although there is substantial evidence for the compositionally anomalous nature of the LLSVPs, there is yet no consensus on the origin of their constituting dense material. While the bottommost (up to 300 km above CMB) parts of LLSVPs may, at least partially, be explained by the occurrence of phase transitions (e.g. the post-perovskite (pPv) phase), their extent higher up above CMB (where pPv is no longer stable) requires another explanation (*Hernlund and Houser*, 2008). Suggestions from previous studies for the origin of the dense material constituting the LLSVPs gen-

erally fall within three categories: (i) a primordial layer that formed early in the Earth’s history (e.g. *Labrosse et al.*, 2007; *Lee et al.*, 2010), (ii) accumulation of a dense eclogitic component from the subducted MORB that segregates at the CMB (*Hofmann and White*, 1982; *Christensen and Hofmann*, 1994; *Tackley*, 2011), and (iii) outer core material leaking into the lower mantle (*Hayden and Watson*, 2007). In this study, we explore the feasibility, from a geodynamic point of view, of scenarios (i) and (ii), which is thus the focus of following discussion.

1.2 Formation Scenario(i): Primordial Dense Basal Layer

What is usually understood by a primitive material is a silicate material that formed after the core-mantle differentiation, and that has never been to shallow depths, where it could undergo mantle-crust differentiation. Consequently, this material is relatively undegassed, and enriched in incompatible elements, compared to the mantle from which melt forming the oceanic crust has been extracted.

Models of mantle-composition that include existence of a primitive reservoir in the deep mantle are mainly motivated by the observations from geochemical studies (*Zindler and Hart*, 1986; *Allègre et al.*, 1987; *Jackson et al.*, 2010; *Mukhopadhyay*, 2012; *Petř et al.*, 2013). The elevated ratios of radiogenic to non-radiogenic isotopes in noble gases (e.g. He, Ar, Xe) found in ocean island basalts (OIBs), compared to those found in mid-ocean ridge basalts (MORB), suggest that the lavas of OIBs are sourced by a less degassed mantle reservoir than the shallow upper mantle from which MORBs are extracted (*Allègre et al.*, 1987). If, indeed, the LLSVPs are compositionally anomalous features that formed early (> 3.5 Gyr ago) in the Earth’s history, have had little material exchange with the ambient mantle, and have plumes forming at their edges and sampling its material - they provide an elegant explanation for the source of primitive signature in the OIBs.

Examples of scenarios for formation of a compositionally distinct layer with primitive geochemical signature are presented in *Labrosse et al.* (e.g. 2007); *Lee et al.* (e.g. 2010). Specifically, *Lee et al.* (2010) suggest that early in the Earth’s history (> 3.5 Gyr ago) iron-rich melt was being produced within the transition zone and lowermost upper mantle, and sinking into and accumulating in the lower mantle upon crystallization. The iron-enrichment would then be responsible for the excess density (by $\sim 4\%$) of the resulting basal layer, ensuring its gravitational stability. The layer was estimated to be 120-240 km thick, and consistent with the volumes of the two LLSVPs proposed in other studies (e.g. *Garnero and McNamara*, 2008). *Lee et al.*

(2010) suggest that iron-enrichment is also responsible for the decrease of the seismic shear velocity within the anomalous material.

1.3 Formation Scenario(ii): Accumulated MORB at the CMB

Oceanic crust enters the lower mantle through deeply penetrating subducting slabs (*Van der Hilst et al.*, 1998) - a process that has been taking place for 3-4 billion years (*Nutman*, 2006; *Shirey and Richardson*, 2011). The amount of oceanic crust that has been produced over the period of time (which itself is uncertain by ~ 1 Gyr) when subduction was active shows that 7 – 53% of the mantle volume today may be occupied by MORB material (*Xie and Tackley*, 2004; *Stixrude and Lithgow-Bertelloni*, 2012). Even the lower limit of this range is sufficient to make up the total volume of the LLSVPs, recalling that they occupy about 2.0% of the total mantle volume (*Burke et al.*, 2008).

Intrinsic density of the subducted oceanic crust may be 0.5 – 5.3% higher than that of the ambient lower mantle (e.g. *Hirose et al.*, 2005; *Ricolleau et al.*, 2010). Given that the density variations due to thermal anomalies, which drive the lower mantle flow, are less than 1%, presence of material derived from the subducted slabs can have significant effects on lower mantle dynamics. To what degree the anomalously dense material perturbs the thermally driven mantle flow depends mainly on the size of this chemical anomaly, as well as the viscosity and flow-velocity of the ambient material.

The lower than average seismic shear velocities in LLSVPs can be, at least partially, explained by their elevated temperatures, compared to the surrounding mantle. Evidence for higher than average temperature in LLSVPs is supported by the correlation of the LLSVP-locations with the restored eruption sites of hotspots and Large Igneous Provinces (*Torsvik et al.*, 2006), as well as the anti-correlation with regions of long term subduction. There is a controversy about the effect that MORB component, accumulated from the subducted slabs, has on the shear wave seismic velocity anomaly associated with the LLSVPs. Ab initio modelling calculations of *Tsuchiya* (2011) infer a decrease in seismic shear wave velocity (by $\sim 2\%$) due to the presence of MORB. The seismic sensitivity study of *Deschamps et al.* (2012) shows that the presence of MORB, on the contrary, leads to an increase in shear wave velocity. Both studies agree, however, that MORB alone cannot explain the compositionally induced excess density of LLSVPs: in *Tsuchiya* (2011) the additional thermal anomaly in LLSVPs would lead to much stronger decrease in shear wave velocity than what is observed, while in *Deschamps et al.* (2012) LLSVPs would require an unrealistically high excess

temperature in order to satisfy seismic constraints. Evidence that supports presence of MORB component in LLSVPs is given in *Ohta et al.* (2008), who performed seismological analysis of the shear wave velocity discontinuities in the LLSVP interior. Authors argue that phase transitions that occur in MORB in the lowermost ~ 400 km of the mantle can explain the negative and a subsequent (i.e. deeper) positive jumps in the observed shear wave velocities. In particular, a 50/50 mix of MORB and pyrolite is proposed as a plausible LLSVP-composition.

Besides the geodynamic motivation for the hypothesis of high density basaltic oceanic crust component segregating and accumulating at the CMB, there is also geochemical evidence to support this notion. *Hofmann and White* (1982) proposed recycling of previously subducted oceanic crust into plumes responsible for the formation of OIBs as a mechanism to explain some of the observed difference in geochemical signature between OIBs and MORB. The former is enriched in incompatible elements, compared to the latter, yet is not compatible with the composition expected for a primitive mantle source.

Analysis of olivines from the Hawaiian lavas reveals contribution of the recycled oceanic crust to the observed geochemical heterogeneity (*Kobayashi et al.*, 2004; *Sobolev et al.*, 2005), and suggests that its content in Hawaiian plume (*Sobolev et al.*, 2005) and in many other plumes (*Sobolev et al.*, 2007) may exceed 10%. Further, recent estimates for the plume responsible for the formation of the Siberian Flood Basalts give about 15% of entrained dense recycled oceanic crust (*Sobolev et al.*, 2011).

Strongly degassed oceanic crust which has segregated and pooled at the CMB is typically invoked as the explanation for the HIMU isotopic end-member, i.e. one of several mantle-sources that may contribute to OIBs (HIMU stands for *high μ* , which in turn stands for high U to Pb ratio) (*Hofmann and White*, 1982; *Zindler and Hart*, 1986; *Hofmann*, 1997). While oceanic crust recycling is a geochemically plausible source (albeit not the only one) of compositional heterogeneity in the mantle (*Coltice and Ricard*, 1999; *van Keken et al.*, 2002; *Davies*, 2011), as implied by the diversity of geochemical signatures found in OIBs (e.g. *Zindler and Hart*, 1986), it remains unclear how long the dense oceanic crust is stored in the mantle before resurfacing. A recent analysis of sulfur isotopes from Mangaia lavas by *Cabral et al.* (2013) proposes a lower limit of 2.45 Gyr for the formation of HIMU isotopic end-member. This can be interpreted as a requirement for existence of oceanic crust material in the lower mantle, which has been subducted and stored there for at least 2.45 Gyr.

1.4 Previous Models

Some of the uncertainty associated with the origin of LLSVPs derives from the lack of understanding of mantles evolution, which in turn stems from the uncertainty of its constituting materials and their physical properties. Geodynamic studies of thermochemical mantle convection typically attempt to find the range of material properties that allows generation and/or sustainability of high-topography thermochemical piles at the base of the mantle, which are laterally stable, manage to survive billions of years of entrainment by ambient flow, and have hot thermal plumes generated predominantly at their edges (e.g. *Tan et al.*, 2011; *Bower et al.*, 2013; *Li et al.*, 2014). Numerous numerical and experimental studies have investigated the influence of physical parameters of a compositionally heterogeneous material, e.g. the degree of density and viscosity variations, on its stability and survival time. In general, results of these studies indicate that chemically distinct material with an intrinsic density elevated by a few percent can form piles that can be maintained in the deeper mantle for billions of years, with thermally or compositionally induced viscosity variations promoting the long-term stability (e.g. *Kellogg et al.*, 1999; *Davaille*, 1999; *Davaille et al.*, 2002; *Tackley*, 2002; *Zhong and Hager*, 2003). To exemplify, the experimental studies of thermochemical convection presented in *Davaille* (1999); *Davaille et al.* (2002), accompanied by a quantitative scaling law for the rate of entrainment of a dense basal layer by hot upwellings, conclude that increase in compositionally induced density and viscosity variations prolong the survival time of the dense layer. The authors suggest that existence of long-lived geochemical reservoirs in the lower mantle is consistent with several plausible regimes of mantle convection - both ‘stratified’ and ‘doming’ regimes. In particular, a 100 km thick dense basal layer (consistent with the combined volumes of the two LLSVPs) was shown to be able to survive over the age of the Earth if its density contrast exceeds 2%. Further supporting this argument, results from geodynamic modelling demonstrate that a layer that is compositionally denser than the ambient material by more than $\sim 2\%$ (though this value is model-dependent, see *Tackley* (e.g. 2012) for review) can withstand homogenizing with the ambient mantle for over 4.5 Gyr (e.g. *Kellogg et al.*, 1999; *Tackley*, 2002; *Zhong and Hager*, 2003) . Results from geodynamic modelling suggest that in order to satisfy both long-term survival and geometrical (e.g. topography) constraints of the LLSVPs, their thermal and compositional buoyancies must be roughly balanced (*Garnero and McNamara*, 2008). If compositionally induced density elevation is too high, the structures flatten out, while a too low value results in excessive entrainment into upwellings (*Garnero and McNamara*, 2008). A high topography yet gravitationally stable thermochemical pile was obtained in the numerical models of *Tan and Gurnis* (2005), using a model where compositional density difference decreases with depth. The compositional density difference between the materials depends on their bulk moduli. The study of

Tan and Gurnis (2005) reveals a specific range of values of bulk modulus and density contrast for which a stable, high topography, neutrally buoyant pile is formed at the base of the mantle. Values outside this range result in either too much entrainment, or a layer at the base that is too heavy to be swept into a pile. Numerical study by *Bower et al.* (2013), however, points out that such neutrally buoyant piles may get destabilized by arrival of cold, dense and highly viscous slabs, which were not part of the model in *Tan and Gurnis* (2005).

Three-dimensional numerical models of mantle convection where the shapes of thermochemical piles resemble those of the LLSVPs are presented in *McNamara and Zhong* (2005); *Bower et al.* (2013); *Bull et al.* (2014), where authors used velocities inferred from subduction history models as surface boundary conditions. Geometry of the piles consistent with observations includes a sharp-edged linear, ridge-like morphology for the African anomaly and a more rounded pile-shape for the Pacific anomaly. Typical models incorporate an initial layer of dense material at the base of the mantle, which is swept into piles in the course of a simulation. The thickness of the layer determines the areal extent and the height of the resulting thermochemical piles. The study of *McNamara and Zhong* (2005) emphasises the importance of a depth- and temperature-dependent rheology of the mantle model together with a realistic plate history as surface boundary conditions. Results of the simulations with an isochemical model of the mantle are shown to be inconsistent with observational constraints, such as seismic tomography images. *Bower et al.* (2013) demonstrate how a high bulk modulus material at the base of the mantle can deform due to ambient convective flow, and produce thermochemical piles highly resemblant in shape of the two LLSVPs.

Perhaps the main limitation of the aforementioned numerical models is that they can only go back in time as far as the reconstructed surface velocity models allow. A three-dimensional model of thermochemical mantle convection which successfully reproduces the high topography of thermochemical piles, their long-term survival for several billion years, and plumes forming predominantly at the edges of the piles, was presented in *Tan et al.* (2011). Extending on the model presented in *Tan and Gurnis* (2005), *Tan et al.* (2011) use high bulk-modulus material for the anomalous layer at the base of the mantle, which is modelled through the prescribed depth-dependence of the compositional density anomaly. A balance between thermally and compositionally induced density anomalies that is obtained at some height above the CMB, is responsible for the high tomography and steep edges of the piles. Increase in compositional density anomaly promotes a ridge-like, rather than a dome-like, shape of the piles. Their most successful cases in terms of pile-shapes have compositional density anomaly in the range of $\sim 1.5 - 2.0\%$ of the ambient mantle density at CMB. Authors report that the lateral stability of the piles is compromised by the downwelling flow, which tends to push the piles around along the CMB. In more recent

three-dimensional numerical study, *Li et al.* (2014) demonstrated at which conditions high topography piles are likely to form at the CMB, survive for several billions of years, and have plumes emanating predominantly from their edges. A moderate compositional density anomaly ($\sim 1.6 - 2.9\%$ of the ambient mantle density at CMB), and a large thermally induced viscosity variations ($> 10^4$) appear to produce most plausible results. This is in agreement with earlier three-dimensional studies of thermochemical convection in Cartesian geometry (*Deschamps and Tackley*, 2008, 2009), albeit the Cartesian models were less successful in having plumes rise from the edges of the piles, rather than their interior.

Numerical studies featuring a dense basal layer as part of their initial conditions are helpful in constraining the bulk material properties of LLSVPs (e.g. density and viscosity), as well as the ambient mantle (e.g. temperature-dependence of viscosity). Given that the volume of compositionally anomalous material is generally kept constant in these models, their results are most relevant for an anomaly formed by scenario (i) - a primitive layer formed early in the Earth's history. We now turn to the numerical studies that address formation of a large scale compositional heterogeneity over time - by segregation and accumulation of oceanic crust at the CMB (scenario (ii)).

Early numerical models of segregation of subducted oceanic crust, featuring 6-km thick oceanic crust component and an isoviscous mantle, found that with a compositional density contrast below 5%, it is unlikely for significant segregation and accumulation at the CMB to occur (*Gurnis*, 1986). However, *Gurnis and Davies* (1986a) show that despite resistance to segregation, clumps of oceanic crust material of different sizes can persist in the mantle for a few billion years, thanks to the inefficiency of stirring by large scale mantle flow. The convective mixing is even less efficient when the depth-dependence of viscosity is introduced (*Gurnis and Davies*, 1986b).

Using a more realistic model of the mantle, which incorporates both temperature- and depth-dependence of viscosity, as well as depth-variation of compositional density anomaly and thermal expansivity, *Christensen and Hofmann* (1994) showed that if the oceanic crust reaches the bottom thermal boundary layer, where the viscosity is lowered due to high temperature, it may segregate from the rest of the lithosphere and accumulate at the bottom. This result is in agreement with the more recent three-dimensional modelling studies of segregating slabs (*Tackley*, 2011).

In general, results from numerical models suggest that segregation of oceanic crust (and its persistence at the bottom - i.e. resistance to entrainment) is enhanced for larger values of compositional density anomaly (*Gurnis*, 1986; *Christensen and Hofmann*, 1994; *Davies*, 2002; *Nakagawa and Tackley*, 2005; *Brandenburg and Van Keken*, 2007; *Huang and Davies*, 2007; *Nakagawa et al.*, 2010; *Li and McNamara*, 2013; *Nakagawa and Tackley*, 2014). This is an intuitive result, and is in agreement

with the observations that an already existing dense basal layer is more stable (against overturn or stirring by ambient mantle flow) the higher is the layers intrinsic density anomaly (e.g. *Davaille, 1999; Tackley, 2012*). Different, sometimes conflicting, conclusions have been drawn from numerical studies regarding the effect of Rayleigh number (Ra - a non-dimensional parameter describing vigor of convection) and temperature-dependence of viscosity on the degree of accumulation of oceanic crust at the CMB. *Christensen and Hofmann (1994)* find that increasing temperature-dependence of viscosity significantly promotes segregation, while increasing Ra (from $Ra = 2.5 \cdot 10^5$ to $1 \cdot 10^6$) moderately suppresses it. However, numerical results of *Li and McNamara (2013)* show that increasing temperature-dependence of viscosity suppresses the formation of dense piles at the CMB, and so does increasing Ra (from $Ra = 1 \cdot 10^7$ to $5 \cdot 10^7$). It is worth noting that in no cases studied by *Li and McNamara (2013)* did significant segregation of oceanic crust occur. The most recent numerical study by *Nakagawa and Tackley (2014)* suggests that Ra (varied from $Ra = 1 \cdot 10^7$ to $1 \cdot 10^8$) plays, in fact, a more dominant role in accumulation of oceanic crust at CMB than does the thermally induced viscosity variations. In contrast to *Christensen and Hofmann (1994)* and *Li and McNamara (2013)*, *Nakagawa and Tackley (2014)* find that increasing Rayleigh number enhances pile-formation by segregated oceanic crust. *Christensen and Hofmann (1994)* also found that the amount of oceanic crust that accumulates at the bottom boundary reaches an equilibrium after some simulation time. This means that a balance is reached between the amount of new crust that gets added to the piles at CMB, and the re-entrainment of the dense material by upwelling flow. The slabs basaltic component (~ 30 km thick in their model, and 2% denser than ambient mantle at the CMB) may not separate completely, such that the accumulated dense piles are not made up of pure basalt, but a mixture with the depleted material. The dense piles in the models of *Christensen and Hofmann (1994)* have ridge-like topography, with plumes rising off the crests of the piles. In the models of *Nakagawa and Tackley (2005); Nakagawa et al. (2009, 2010)*, the segregated oceanic crust component forms large piles, which cover a significant fraction of the CMB, extend high up into the mid-mantle, and have interior oceanic crust concentration falling gently with height above CMB. Some of the piles have steep edges, which locations correlate with the upwelling flow.

1.5 This study

Comparing the features of thermochemical piles in models where they are generated by deforming an initially flat dense basal layer, and those where they are generated over time by segregation and accumulation of dense oceanic crust, it appears that the

former are more successful at reproducing the shapes observed for LLSVPs. From a modelling point of view, the bulk properties of a dense basal layer, which ultimately defines the bulk properties and shapes of resulting piles, can be straightforwardly prescribed as part of the initial conditions. This is not the case for models where the dense material accumulates self-consistently over time, because it is difficult to predict the bulk properties of the final mixture that makes up the piles. Both the interior structure of the piles (in terms of distribution of temperature and dense material in their interior), and their large-scale characteristics (shape, total volume, and buoyancy with respect to ambient mantle) are determined by processes that may be highly variable in time - rate of segregation of dense material at the CMB, rate of its subsequent re-entrainment by plumes, and the amount of stirring taking place in the interior of the piles. Seismic studies have yet to determine whether the upper boundary (if there is such) of LLSVPs is sharp, like their edges, or more diffuse. It is interesting to know, however, whether either case is geodynamically feasible with the different mechanisms by which the piles may be produced (a preexisting dense layer vs gradual accumulation). Current understanding appears to be that thermochemical piles formed from a gradually accumulating dense material can only produce a gradual upper boundary (*Garnero and McNamara, 2008; Tackley, 2012*).

Here, we present the results of thermochemical convection simulations that illustrate the dynamics and thermal and compositional evolution of large-scale compositional heterogeneities at the CMB, which develop self-consistently by segregation and accumulation of subducted oceanic crust. Guided by the results from previous studies, we use a thin (6 km) oceanic crust, to conservatively estimate its perturbation to the ambient flow and settling at the CMB, and a rheological model of the mantle that leads to realistically large thermally induced viscosity-variations.

We systematically vary two physical parameters: intrinsic density anomaly of the oceanic crust and viscosity. Dependence of viscosity on depth, temperature and composition have all been shown to play an important role in determining the rate of entrainment upwards and segregation to the bottom of an intrinsically dense compositional anomaly (e.g. *Gurnis, 1986; Gurnis and Davies, 1986b; Sleep, 1988; Solomatov et al., 1993; Davaille, 1999; Zhong and Hager, 2003; Lin and van Keken, 2006; Kumagai et al., 2007; Li and McNamara, 2013*). Unfortunately, observational and experimental data on viscosity variation and value in the deep lower mantle (within and above the thermal boundary layer overlying CMB) is uncertain to ~ 1 order of magnitude (see *Tackley (2012)* for a recent overview). Temperature, composition (i.e. presence of post-perovskite phase, or distribution of the two main phases - perovskite and magnesiowustite), grain size, deformation history, and creep mechanism (possible occurrence of dislocation creep in regions of high stress, rather than the commonly assumed diffusion creep) in the lowermost mantle may all have a say on its effective viscosity.

In our models, viscosity is varied only in the lowermost 500 km of the mantle. We don't attribute its variation to any specific mechanism, like the ones mentioned above. Rather, we treat it as a generalized uncertainty in the viscosity profile.

To perform this high-resolution numerical study, we developed an efficient FEM code, building on efficient solvers MILAMIN (*Dabrowski et al.*, 2008), together with packages MUTILS (*Krotkiewski*, 2013), and Triangle (*Shewchuk*, 1996). We employed dynamically adaptive time and space resolution, and marker-in-cell methodology. This enabled us to model thermochemical mantle convection at realistically high convective vigor, strong thermally induced viscosity variations, and long term evolution of compositional fields.

Previously published geodynamic studies, as well as our own experience, point to a number of technical challenges associated with the numerical approaches to investigate thermochemical mantle convection. Physical relevance of the obtained numerical results is largely dependent on the way these challenges are addressed. To provide an accurate degree of confidence for the results presented in this study, we accompany their physical interpretation and quantitative analysis with a critical layout of the methods with which they were obtained.

This thesis is organised in the following way. In Chapter 2, we describe the physical processes involved in the interaction of compositional anomalies with the thermally induced ambient flow. The goal is to build a framework for the qualitative and quantitative discussion of the simulation results, as well as to identify the demands (in terms of time- and space-resolution) for the numerical tools aimed at modelling these processes. In Chapter 4, we give a brief introduction to the particle-in-cell methodology, with the focus on their success and limitations in thermochemical convection simulations. The numerical method of our choice for this study is presented in this section as well. Results from our numerical simulations are presented in Chapter 6, with discussion and conclusions presented at the end of the chapter.

Chapter 2

Physics of Downward Segregation and Upward Entrainment

In this chapter, we describe the physical processes involved in the interaction of compositional anomalies with the thermally induced ambient flow. We limit the discussion to two cases: (i) long-term survival of a dense compositionally heterogeneous material in the lowermost mantle, and (ii) segregation of subducted oceanic crust to the bottom of the mantle due to its compositionally induced excess density.

2.1 Governing Forces

Processes of long-term survival of a dense compositionally heterogeneous material in the lowermost mantle, as well as segregation of subducted oceanic crust to the bottom of the mantle due to its compositionally induced excess density, revolve around the interaction, or competition, between compositionally and thermally induced buoyancy (on large, gravity force dominated lengthscale), as well as the interaction between the buoyancy and the drag (on small, shear force dominated lengthscale). The compositionally dense anomaly in a vigorously convecting system can thus be categorized into two parts: a gravitationally stable large-scale anomaly, where buoyancy forces dominate, and the thin entrained tendrils, produced on a lengthscale where viscous drag dominates. The numerical code aimed at modeling the process of thermochemical evolution must be able to capture both of these regimes.

In terms of the characteristic scales, we can express the governing forces as following:

$$F_{\text{buoyancy}} = -gV\Delta\rho \quad (2.1)$$

$$F_{\text{viscous drag}} = -L \cdot \mu \frac{v}{L} = \mu v \quad (2.2)$$

where g is the gravitational acceleration, V is the volume of the material with the anomalous density $\Delta\rho$ (induced by thermal or compositional variations, or a combination of both), μ is the viscosity, v velocity and L a characteristic length scale. The quantity v/L is representative of the velocity gradient.

2.2 Large Scale: Topography of Dense Basal Piles (Gravity Force Dominated Lengthscale)

A dense layer underlying a less dense material (think compositionally dense D" layer underlying ambient mantle) is gravitationally stable, given that its compositionally induced density anomaly is larger than the thermally induced one. Thermally induced density variations drive the flow in the less dense ambient material (i.e. hot rising plumes and cold downwelling slabs), and may deform the dense layer, such that the latter obtains larger topography, or even forms disconnected piles.

A slab sinking into the lower mantle has to displace the material ahead of it in order to proceed downwards. This induces a vertical flow which, upon reaching the impermeable bottom boundary (due to a large density contrast with the underlying outer core) is forced to turn, and further induces flow parallel to the bottom boundary. The dense layer below the region of subducting slab gets thinned, which is compensated by it getting thickened in other regions, away from the slab.

Similarly, the vertical flow of a hot mantle upwelling, or plume, induces lateral flow along the bottom boundary due to a dynamic low-pressure that is created at the plumes base. Following a streamline from a region outside of the plume (within the thermal boundary layer), where the flow is mainly parallel to the bottom boundary, and upwards into the rising plume, where the flow is mainly vertical, the horizontal component of velocity vanishes. Material subjected to such flow pattern shrinks in the horizontal direction, and, by continuity, gets stretched in the vertical direction. As the ambient material undergoes such deformation, it drags the underlying dense material along with it. This causes the dense layer to thicken beneath the rising plume, and its surface to tilt with respect to the horizontal boundary. The tilted surface of the dense layer (edge of the pile) now experiences a pure shear type of squeeze from the horizontal flow-component of the ambient material, as well as a simple shear type of smearing from the vertical flow component of the ambient material. The dynamic pressure due to pure shear part of the flow supports the enlarged topography of the dense layer. The smearing is responsible for the formation of thin tendrils, or filaments of dense material, discussed in the next section.

For a given range of material parameters of the dense material (such as density, viscosity, thermal expansivity, etc.), and its surrounding conditions (e.g. temperature

at the CMB), thermal convection may develop within the dense layer. The dynamic pressure of the interior flow may also affect the topography of the layer.

The topography of the dense layer plays an important role in its subsequent evolution, due to both thermal and mechanical feedback between the layer and the ambient material. The amount of basal heat that flows into the ambient material, and provides the excess buoyancy to drive the convective flow, depends on the topography of the dense basal layer. This is largely due to the thermally insulating effect of the latter. As outlined above, the topography of the dense layer, in turn, depends on the flow of the ambient material: the dense material is thickened beneath the upwelling flow, and thinned, or absent, beneath the downwelling flow. The amount of thickening or thinning of the dense basal material is proportional to the strength of the ambient flow.

2.3 Small Scale: Segregation and Entrainment of Thin Filaments (Shear Force Dominated Lengthscale)

The smearing action of ambient flow on the surface of the dense layer may lead to formation of thin tendrils, or filaments, made up of dense material, and their subsequent entrainment into the rising plumes. This is commonly observed in both laboratory (*Solomatov et al.*, 1993; *Kumagai et al.*, 2007; *Davaille et al.*, 2002; *Jellinek and Manga*, 2004), and numerical (*Schott et al.*, 2002; *Zhong and Hager*, 2003; *Lin and van Keken*, 2006; *Huang*, 2008) studies. The entrained tendrils undergo mechanical mixing, or stirring, with the ambient material. The initially stratified layer may eventually become completely homogenized via this process. In order for the entrainment of dense material to take place, the viscous drag (given by Equation 2.2) imposed on the surface of the layer must exceed the stabilizing buoyancy force (which is proportional to the size of the anomaly, as given by Equation 2.1). The thickness of an entrained tendril reflects the lengthscale at which this condition is satisfied.

Strong variations in thermal field, both in time and in space, of a vigorously convecting mantle, and the strong temperature-dependence of viscosity, lead to large variations in shear stresses imposed on the surface of the dense basal layer by the adjacent mantle. The shear stresses are affected by the spatial gradients of velocity of the ambient flow, as can be seen from Equation 2.2. At high temperatures, the ambient velocity may be large (both due to low viscosity and large thermally induced buoyancy). However, high temperature also means low viscosity, which reduces the shear stress imposed on the dense layer. Reversed argument holds for low temperatures. Such competition between the temperature-dependent buoyancy and drag

forces complicates the assesment of whether higher or lower temperatures lead to more or less efficient entrainment of the dense layer.

While hot rising plumes may act as a sink that entrains the dense material away from the bottom, counteracting its accumulation into larger piles, the subducting downwellings that bring compositionally dense material into the lowermost part of the domain, may act as a source of the dense material (subducted slabs bringing the dense oceanic crust into lowermost mantle). Settling velocity of an anomalously dense body relative to the vertical component of velocity of the ambient flow determines whether the body will settle at the bottom boundary, or continue circulating with the ambient flow. It is crucial to remember that the vertical component of the ambient flow velocity vanishes towards the impermeable bottom boundary. Thus, at a certain depth, the settling velocity of the anomalously dense body exceeds the vertical component of velocity of the ambient flow. Followingly, in order for the settling of anomalously dense material to take place, it needs to reach sufficient depth. If only a part of the dense material reaches such depth, it will get streched, such that a part of it may settle, while the other part gets entrained.

Summary

In summary, the relation between the rate of settling of dense material to the bottom of the domain, and the rate at which it gets entrained away by the ambient flow, determines for how long a preexisting compositional anomaly will survive, or whether a new large scale anomaly will form. The ratio between these rates also determine whether the compositional anomaly will grow in size, or reach some steady-state extent. Correct estimation of these rates in a numerical model rests upon sufficient resolution of the governing physical processes - buoyancy and drag, action of which is outlined above.

Chapter 3

Mathematical Model

In this chapter, we present the mathematical model that describes thermochemical flow, together with the approximations that we made to simplify the equations, based on some characteristic properties of the mantle. The nondimensional parameters which are commonly used for the description of the physical processes involved are also introduced here.

3.1 Equations Describing Thermochemical Mantle Flow

Equations that describe the thermochemical mantle flow are the conservation equations of momentum, mass, energy, and composition. Physical properties of the Earth materials allow some simplification of these equations, such that only the terms describing the dominant effects are left standing. Due to the high viscosity, and thus relatively low strain rates associated with the flow, the inertial forces can be ignored. This leads to a steady state Stokes equation, which describes the balance between dynamic pressure, viscous stresses, and buoyancy. Further, the Boussinesq approximation is often employed, which implies incompressibility, and thus constant density everywhere except in the buoyancy-term of Stokes equation. In their dimensional form (primes denote dimensional quantities), the resulting conservation equations

Table 3.1: Physical and geometrical parameters representative of the Earth’s deep mantle (e.g. Dziewonski and Anderson, 1981; Schubert et al., 2001; Steinberger and Calderwood, 2006; Tackley, 2012), which we use for nondimensionalization. Prime denotes dimensional quantity.

Quantity	Symbol	Values Representative of Deep Mantle	Dimensions
Gravitational acceleration	g'	10	m s^{-2}
Thermal expansivity	α'	$1 \cdot 10^{-5}$	K^{-1}
Density	ρ'	$5.5 \cdot 10^3$	kg m^{-3}
Temperature drop across mantle-depth	$\Delta T'$	3215	K
Depth of the mantle	D'	$2.9 \cdot 10^6$	m
Thermal diffusivity	κ'	$6 \cdot 10^{-7}$	$\text{m}^2 \text{s}^{-1}$
Dynamic viscosity	μ'	$5 \cdot 10^{21}$	Pa s

are:

$$-\frac{\partial p'}{\partial x'_i} + \frac{\partial \tau'_{ji}}{\partial x'_j} = \rho' g'_i \quad (3.1)$$

$$\frac{\partial v'_i}{\partial x'_i} = 0 \quad (3.2)$$

$$\frac{DT'}{Dt'} = \kappa' \frac{\partial}{\partial x'_i} \left(\frac{\partial T'}{\partial x'_i} \right) \quad (3.3)$$

$$\frac{DC}{Dt'} = 0 \quad (3.4)$$

where subscripts i and j denote the Cartesian components of vector and tensor quantities, x'_i is the position vector, v'_i the velocity vector, p' dynamic pressure, τ'_{ij} deviatoric stress tensor, ρ' density, κ' thermal diffusivity, g'_i gravity acceleration vector ($\sim 10 \text{ m/s}^2$ for the radial direction and zero for the horizontal direction), T' temperature, t' is time, and $\frac{D}{Dt'}$ is the material derivative. $C(\vec{x})$ describes spatial distribution of different materials (phases). In the presented work, we only consider immiscible fluids, and disregard cases of chemical mixtures of different materials. Thus, $C(\vec{x})$ is a discrete indicator function that can assume values 0 or 1 (since we only have two phases): $C(\vec{x}) = 1$ if \vec{x} is occupied by the compositionally dense material, and $C(\vec{x}) = 0$ otherwise.

In Equation 3.3, the source-term is omitted (i.e. set to zero), since our models don’t have any internal heating (see Section 6.4.4 for the effects of excluding internal heating

on our results).

We model materials constituting the Earth's mantle as fluids whose rate of deformation ϵ'_{ij} and deviatoric stress τ'_{ij} are linearly dependent (Newtonian fluids). We also assume them to be incompressible and isotropic. In this case, the deviatoric stress, which appears in in Equation 3.1, can be expressed in terms of rate of deformation - and thus velocity, using the following constitutive relation:

$$\tau'_{ij} = 2\mu'\epsilon'_{ij} = \mu\left(\frac{\partial v'_i}{\partial x'_j} + \frac{\partial v'_j}{\partial x'_i}\right) \quad (3.5)$$

Assuming incompressibility of the mantle across its depth is not a fully justified approximation for mantle-like thickness and material-properties (e.g. *Schubert et al.*, 2001). Some of the consequences of adopting it in our model, most important of which are the lack of depth-dependencies of various material-properties (e.g. density and thermal expansivity), are outlined in Section 6.4.1.

Equations 3.1- 3.4 are nondimensionalised using the standard transformation of variables, e.g. as in *Schubert et al.* (2001), and the reference values of the physical parameters as presented in Table 3.1. In their nondimensional form, the conservation equations are:

$$-\frac{\partial p}{\partial x_i} + \frac{\partial \tau_{ji}}{\partial x_j} = Ra(T + BrC)g_i \quad (3.6)$$

$$\frac{\partial v_i}{\partial x_i} = 0 \quad (3.7)$$

$$\frac{DT}{Dt} = \frac{\partial}{\partial x_i} \left(\frac{\partial T}{\partial x_i} \right) \quad (3.8)$$

$$\frac{DC}{Dt} = 0 \quad (3.9)$$

In Equation 3.6, Ra is the Rayleigh number, which describes the vigor of convection, and is defined as the ratio between the buoyancy forces driving convection, and the dissipative effects opposing convection:

$$Ra \equiv \frac{\alpha' g' \rho' \Delta T' D^3}{\kappa' \mu'} \approx 1.5 \cdot 10^7 \quad (3.10)$$

where the Ra -value was obtained according to the values presented in Table 3.1 (primes denote dimensional quantities). Ra -number used in our study is comparable to the ones used in similar, previously published studies: e.g. $Ra = [2.5 \cdot 10^5 - 1 \cdot 10^6]$ in *Christensen* (1984), $Ra = [1 \cdot 10^6 - 1 \cdot 10^7]$ in *Brandenburg and Van Keken* (2007), $Ra = 1 \cdot 10^7$ in *Nakagawa and Tackley* (2005); *Nakagawa et al.* (2010), $Ra = [5 \cdot 10^6 - 5 \cdot 10^7]$ in *Li and McNamara* (2013), $Ra = [1 \cdot 10^7 - 1 \cdot 10^8]$ in *Nakagawa and Tackley* (2014).

Br is the buoyancy ratio, which describes the relative strength of the compositionally and thermally induced density variations:

$$Br \equiv \frac{\Delta\rho'_C}{\alpha'\rho'\Delta T'} \quad (3.11)$$

where $\Delta\rho'_C$ stands for the compositionally induced density variations. In our simulations, Br is systematically varied from ~ 0.57 to ~ 1.1 (corresponding to 1.8% and 3.6% compositional density anomaly, respectively).

The advective component of conservation Equations 3.8 and 3.9 - the left-hand side - is expressed through the material derivative $\frac{D}{Dt}$. This is a Lagrangian fomulation, which implies a reference frame that moves with the material. Alternatively, the advective component can be expressed from the point of view of a fixed point in space - or the Eulerian reference frame. The left-hand side of Equations 3.8 and 3.9 in Eulerian formulation take the following form:

$$\frac{DT}{Dt} = \frac{\partial T}{\partial t} + v_i \frac{\partial T}{\partial x_i} \quad (3.12)$$

$$\frac{DC}{Dt} = \frac{\partial C}{\partial t} + v_i \frac{\partial C}{\partial x_i} \quad (3.13)$$

Note that in Equation 3.9 (and 3.4) the discrete indicator function C cannot assume any intermediate values between 0 and 1. This is in contrast to other fields in our model, such as temperature, which are represented by continuous functions, and in (continuum) theory can assume an infinite number of values within a given range (in nature constrained by quantum effects, and in modelling practice by numerical precision). Consequently, a physical field represented by a continuous function, albeit on a finite number of points, can be readily interpolated between the locations where the function is known (e.g. computational nodes), to locations where it is unknown (in-between the nodes). This can be done by computing some sort of weighted average (e.g. with respect to distances between the nodes and the point of interest) over the known function-values. Such procedure cannot be applied to discrete indicator functions, whose values are rather interpreted as logical statements (e.g. whether or not the location is occupied by a given material), and averaged function-values have little or no meaning.

The need for interpolation arises frequently during numerical solution of the PDEs (which are derived under the assumption of a *continuous* physical system). One example is numerical evaluation of integrals (e.g. for the weak form of the equations in FE or FV methods), where the function needs to be evaluated at the quadrature points, which generally do not coincide with the computational nodes. Another example includes mapping a function that is evaluated in one set of nodes (e.g. a computational

grid) onto another set of nodes (e.g. markers, or a new grid generated by remeshing or refinement procedures). Yet another example is modelling of advection with an Eulerian static grid method (i.e. field-method), where the field being advected needs to be evaluated in points along its trajectory, which generally do not coincide with the computational nodes.

Equation 3.6 falls within the class of elliptic equations. Such equations describe boundary value problems, solutions to which are static, or time-independent. Time-dependence of the system enters through the Equations 3.8 and 3.9 for conservation of energy and composition, respectively. The former is a parabolic equation, while the latter is a hyperbolic one, and both equations describe initial value problems. Solutions to such problems describe time-evolution of the system, and are thus time-dependent. Thus, to close the system of Equations 3.6-3.5, mechanical (velocity or traction) and thermal (temperature or heat flux) boundary conditions must be provided, together with the initial conditions for temperature and composition.

Chapter 4

Numerical Modelling of Thermochemical Convection

In this chapter, we introduce the numerical methodology that we used to solve the system of equations presented in Chapter 3, describing the thermochemical mantle flow. A detailed outline of each step of the algorithm of the code that we developed for this purpose is presented. We dedicate particular attention to the discussion of the marker-in-cell methodology, which we used for the solution of advective components of the conservation equations. Finally, a number of benchmarking results are presented at the end of the chapter, to demonstrate the ability of the new code to model thermochemical mantle convection.

4.1 Outline of Numerical Methodology

We have developed an unstructured FEM code for geodynamic modelling of thermochemical mantle convection, with particle-in-cell methodology, building on efficient MATLAB routines from MILAMIN (*Dabrowski et al.*, 2008), together with packages MUTILS (*Krotkiewski*, 2013), and Triangle (*Shewchuk*, 1996). The velocity and pressure fields, given by the coupled system of Equations 3.6, 3.7 and 3.5, are solved with the finite element method solver MILAMIN (*Dabrowski et al.*, 2008). Velocity is discretized with an unstructured triangular grid with second-order shape functions, using seven-node triangular elements. Pressure field within each element is discretized with linear shape function. The global pressure field is thus piecewise linear, discontinuous across element-edges. For the numerical solution of the thermal advection-diffusion Equation 3.8 we employ the fractional step method, or Godunov splitting (*LeVeque*,

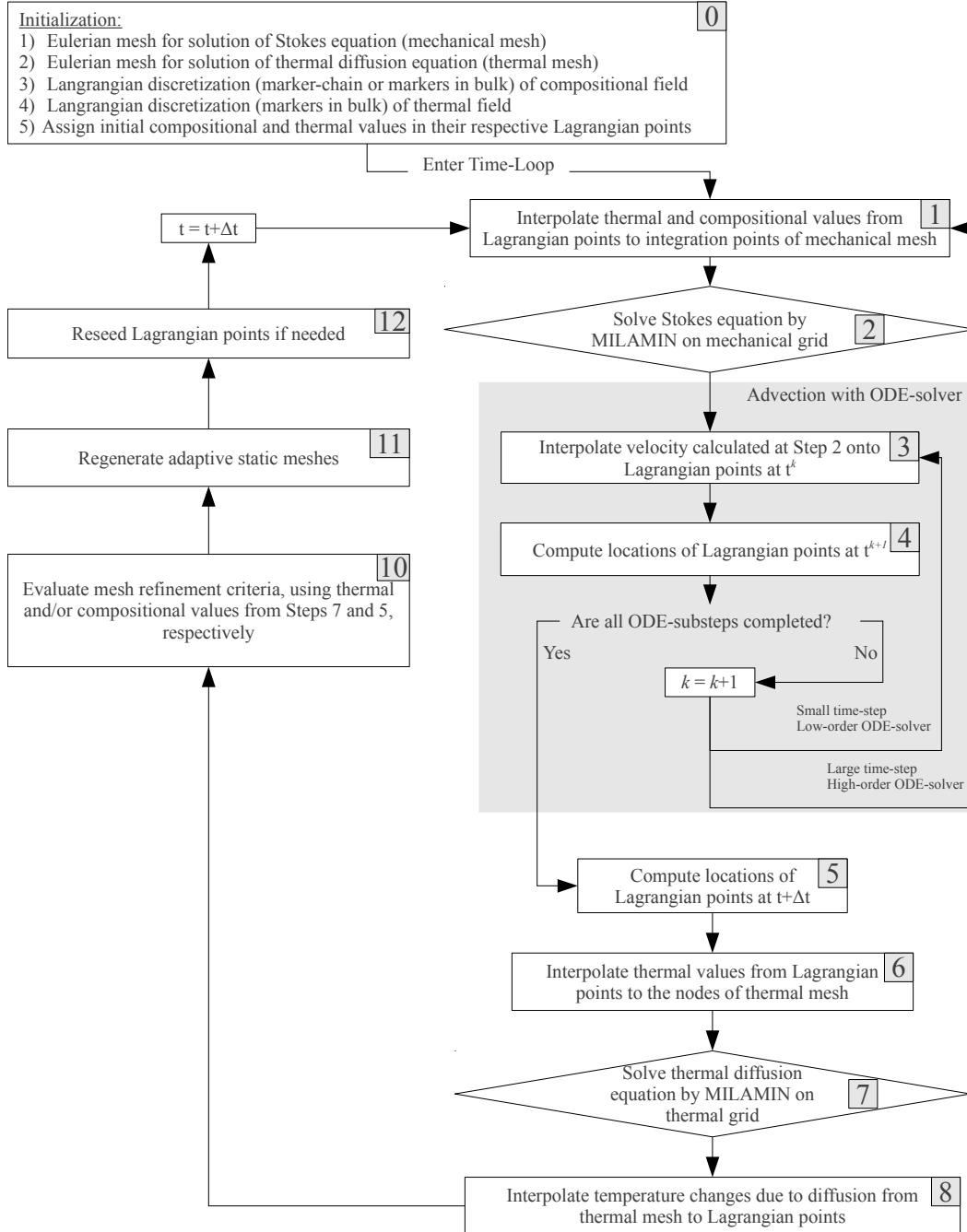


Figure 4.1: Flow chart of the general algorithm for the solution of the thermomechanical equations with presence of compositional fields.

2002), for time-discretization: pure advection is solved first, followed by the diffusion step. The diffusion equation is solved on an unstructured triangular grid with first-order (linear) shape functions. The thermal grid elements are generated by splitting each mechanical element into six triangles.

At regular time-intervals throughout the simulation, we regenerate the static meshes, on which mass and momentum conservation, as well as thermal diffusion equations are solved. The mesh is refined in regions of large thermal gradients. This refinement criteria improves the accuracy of the diffusion solver, and also that of the mechanical solver. The latter is due to the exponential dependence of viscosity on temperature, due to which regions of large thermal gradients correspond to regions of strongly varying viscosity, which require higher resolution in order to sustain some lower limit of accuracy (*Moresi et al.*, 1996; *Deubelbeiss and Kaus*, 2008; *Duretz et al.*, 2011).

The advective component of Equation 3.8, as well as Equation 3.9, are solved using the characteristics based marker-in-cell method (*Gerya and Yuen*, 2003). Markers, or tracers, are points in space in which the initial thermal and compositional field values are prescribed. During the advection step, positions of markers are updated, according to the computed velocity field, and using the second order Runge Kutta method (mid-point rule) for computing the trajectories. The number of markers is generally larger (by at least an order of magnitude) than the number of grid-nodes. The code has been thoroughly tested for thermal and thermochemical convection, against benchmarks commonly used in the geodynamic community (e.g. *Van Keken et al.*, 1997; *Blankenbach et al.*, 1989).

The general methodology goes as following (see also Figure 4.1):

1. *Initialization:*

- (a) *Spatial Discretization:* (i) generate Eulerian meshes (connected sets of points, whose positions are fixed in time irrespective of the flow) for solution of the coupled system of momentum and mass equations (mechanical mesh), and the diffusion component of the energy equation (thermal mesh); (ii) construct Lagrangian points (connected (marker-chain) or not (marker-in-cell), whose positions change in time according to flow-trajectories), for discretization of fields that are to be advected (temperature, composition).
- (b) *Initial values:* prescribe initial values for the thermal and compositional fields in the Lagrangian points.

2. *Time Loop:*

- (a) *Collection of Information Necessary for the Solution of the Incompressible Stokes Equation:* transfer field-values of temperature and composition from the Lagrangian points to the integration points of the mechanical grid.

- (b) *Solution of Stokes-Equation*: compute the velocity and pressure fields on mechanical grid.
- (c) *Advection*: interpolate velocity-values from the mechanical grid to the Lagrangian points (using shape-functions of mechanical elements), and update the positions of the Lagrangian points.
- (d) *Collection of Information Necessary for the Solution of Thermal Diffusion Equation*: transfer thermal field-values from Lagrangian points, to the thermal grid-nodes.
- (e) *Solution of Diffusion Equation*: update the thermal field, by solving the diffusion equation on thermal grid. Transfer the incremental change in temperature, together with a correction to account for subgrid-scale diffusion, from the thermal grid to the Lagrangian points.
- (f) **Repeat the steps of the time-loop until the total time of simulation is reached.**

The unknown fields \vec{v} , T , and C_k from Equations 3.6 - 3.9 may have different characteristic length-scales associated with them, and thus pose different resolution-requirements to their spatial approximation (e.g. in terms of number of elements, order of polynomials for shape-functions, or number of markers). This is part of the motivation for using different spatial representations (mechanical grid, thermal grid and markers) for different fields.

Steps 1 and 6: Using marker-in-cell method for modelling advection of compositional and thermal fields requires an interpolation step (Steps 1 and 6 in Figure 4.1) of properties carried by the markers to the static meshes on which conservation equations of momentum and mass, as well as the thermal diffusion equation, are solved. Different methods for performing this step, and the potential caveats associated with the interpolation errors in this part of the algorithm, are presented in Section 4.3. In marker-chain method, material interfaces are discretized as a connected set of points that lie on the boundary between different materials. Together with the boundary of the domain (as well as boundaries around holes within the domain, if such are present), the connected set of points (or multiple sets) constitute closed polygon-boundaries which enclose the regions spanned by each material. Determining which material is (or whether there is a hole) at an arbitrary point within the domain is then simply a matter of determining which polygon the point falls into.

Steps 3-4: For computation of trajectories during the advection step (Steps 3-4 in Figure 4.1), we use second order Runge Kutta method (mid-point rule). The advection step can either be performed over one full time-step ('frozen velocity'), or - in cases when the velocity field is reevaluated at each intermediate step of the ODE-solver - over an increment of a time step. The former approach is first-order accurate

in time, while the latter is second-order accurate in time. The former was used in our simulations, since we used a relatively small time-step size due to other time-resolution restrictions, discussed in Section 4.2.1.

Step 11: To generate an adapted mesh (Step 11 in Figure 4.1), we first generate an approximately uniform unstructured triangular mesh, which we refer to as the auxiliary mesh. Mesh-generator ‘Triangle’ (Shewchuk, 1996) allows for different desired element sizes to be prescribed in regions occupied by each element of the auxiliary mesh, and use it as input for generating a new adapted mesh. In cases when the refinement criterion is the magnitude of thermal gradients, thermal gradients are computed on the preexisting mesh (i.e. on which thermal diffusion was solved in previous timestep), and interpolated onto the auxiliary mesh. The desired element size in regions occupied by each element of the auxiliary mesh is scaled such that elements with highest gradients get prescribed the smallest element-areas, and vice versa. In cases when the refinement criterion is presence of compositional interfaces (i.e. it is desirable to have smaller elements in regions where material-properties change abruptly, such as in the vicinity of material-interfaces), we identify the elements of the auxiliary mesh which are crossed by the interface, and prescribe the smallest element-areas to those elements. When using marker-in-cell method (described in Section 4.2.4), elements containing the interface correspond to those that contain at least two types of markers. When using marker-chain method (described in Section 4.2.4), elements containing the interface correspond to those containing the chain-markers. For marker-chain method, in addition to prescribing the desired element-area in different regions of the domain, one can also generate elements whose edges are aligned with the segments of the marker-chain.

Option to use compositional field as one of the refinement criteria is presented here for the sake of generality. For the long-term thermochemical convection simulations, such as the ones presented in Chapter 6, we use only the thermal gradients as criterion for mesh-refinement. Also, the marker-chain method is discussed here (and in Section 4.4.1 on benchmarking and Section 4.2.4) in order to provide a perspective on the advantages and limitations of the marker-in-cell method, where only the latter is used for the simulations presented in Chapter 6.

Note that ‘Triangle’ allows only for the *maximum* element-area to be prescribed, but there is no way to constrain the smallest element-area. Thus, element-areas are only bounded from above, and care must be taken to avoid producing tiny elements. The only times we ran into this problem was when using methods that force element-boundaries to be aligned with the material-interface(s) (marker-chain with conforming mesh). This is one of the main reasons why we chose not to use such methods for modelling long-term thermochemical mantle convection, which involves extensive deformation of material-interfaces. In models featuring modest deformation of materials (e.g. isoviscous Rayleigh-Taylor instability benchmark presented in Sec-

tion 4.4.1), however, such methods provide a valuable alternative for comparison with methods where smearing of material-interfaces in element-interiors are inevitable.

Step 12: As materials get deformed throughout the simulation, and change their associated characteristic length-scales, the need may arise to redistribute markers used for their spatial discretization. To exemplify, envision a single vortex flow in a two-dimensional box filled with material A, in which a disc of material B is being advected. For simplicity, we will assume that although materials A and B are different, this does not influence the velocity field, and thus material B is being advected passively. A velocity field representing a single vortex flow is relatively smooth and can be adequately resolved with a few grid-nodes or elements. The disc-radius of material B can be chosen such that its initial characteristic lengthscale is comparable to that of the velocity field (note that the latter does not change with time). Further, we can construct a grid of resolution h_v , as well as a grid or a set of markers with resolution h_C , such that $h_v = h_C$. In other words, the value of the discretization error for the velocity and the compositional fields are similar at the beginning of the simulation. A structure advecting in a single vortex flow gets continuously stretched and thinned. Thus, the discretization error associated with the compositional field gradually increases, because its diminishing lengthscale cannot be resolved with the initially constructed grid or set of markers of a coarser resolution h_C . In order to maintain the initially prescribed value of the discretization error associated with the approximation of the compositional field, more nodes or markers must be introduced. In marker-chain methods, this involves adding new markers along segments of the chain that become longer than some prescribed threshold, and removing markers along chain-segments that become too short.

In marker-in-cell method, we generally aim to keep markers-distribution within the domain approximately uniform (although this is not necessary for tracer-ratio methods, and marker-adaptivity can be explored in the future, with higher marker-density in regions where two types of markers meet). However, markers may become inhomogeneously distributed throughout the simulation due to errors associated with computing their trajectories, or solution of Stokes equation. It is possible to add and remove markers in regions where they get diluted or clustered, respectively, where the material and/or thermal properties of the newly added markers are prescribed by interpolating from their neighboring markers. However, when running our models, we chose not to tamper with marker-distribution throughout the simulation, except for the very rare occasions when markers escape the bounds of the domain due to errors associated with computing their trajectories. To detect whether any artificial clustering of markers occurs, we perform a test similar to the one described in *Christensen and Hofmann* (1994): we divide the model domain into quadratic cells of the size similar to the mean area of triangular elements. Statistics of the number of markers that fall into each cell is compared to a Poisson's distribution, which is indicative of

random marker-distribution. If some artificial clustering is detected, we interpreted it as an insufficient spatial and/or temporal resolution for the given simulation, and increase the resolution until no more clustering is detected. Thus, for the simulations presented in this work, Step 12 of the algorithm shown in Figure 4.1 refers only to cases when we use marker-chain method for advection of compositional fields.

In marker-in-cell methods, especially when using adaptive meshes in which we cannot control the size of the smallest elements, there is always a possibility that an element will have no markers falling into its interior. In such cases, to determine thermal and/or compositional properties in the elements interior, we interpolate properties from its neighboring elements, in which these properties are known.

4.2 Numerical Challenges

4.2.1 Time-Discretization

Full System of Equations

The four primary unknown variables in the system of Equations 3.6 - 3.9 are velocity, pressure, temperature, and composition. Variations in temperature and composition induce density variations, which enter the buoyancy term of Equation 3.6 for velocity. At the same time, velocity appears in the advective term of both temperature and composition - Equations 3.8 - 3.9. This leads to a non-linear coupling between Equations 3.8 - 3.9 (or, equivalently, Equations 3.12 - 3.13) and Equation 3.6.

We use fractional stepping for time-discretization of the non-linearly coupled time-dependent conservation equations of energy and composition, and the instantaneous incompressible Stokes equation. We alternate between solving the coupled system of Equations 3.6 - 3.7, and the time-dependent Equations 3.8 and 3.9, to find the approximate solution of the full problem given by Equations 3.6 - 3.9.

Velocity and pressure are solved for using the coupled system of Equations 3.6 and 3.7, where Equation 3.7 acts as a constraint to Equation 3.6. The buoyancy term on the right hand side of Equation 3.6 is computed using the temperature and composition fields given for the particular point in time for which the Stokes solution is sought. The obtained velocity-solution is used to solve the time-dependent Equations 3.8 and 3.9, the result of which are the updated fields of temperature and composition. Note that the instantaneous velocity field used for solving Equations 3.8 and 3.9 is given by Equations 3.6- 3.7 for a particular point in time (e.g. for the beginning of a time-step), yet we use it as a constraint for the time-dependent Equations 3.8 and 3.9 throughout the entire time-step, or finite fractions of a time-step. Thus, solution of

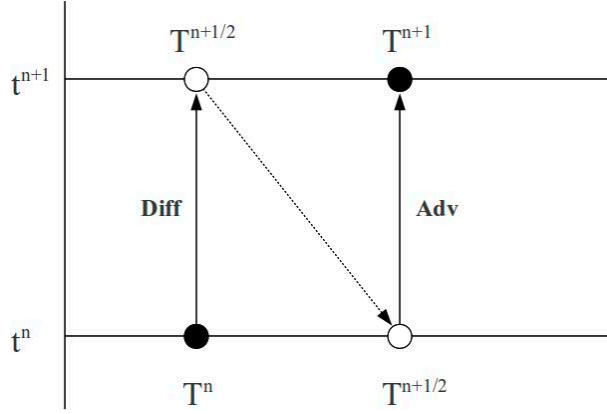


Figure 4.2: Graphic illustration of the operator splitting method. *Diff* and *Adv* are diffusion- and advection-operators, respectively.

the non-linearly coupled system of Equations 3.6 - 3.9 with a fractional step method introduces a splitting error, which size is dependent on the size of the time-step.

Advection-Diffusion Equation: Operator Splitting

Equation 3.8 describes time evolution of the thermal field, subject to advection and diffusion processes. For its time-discretization, we employ the fractional step method, or Godunov splitting (*LeVeque*, 2002): pure advection is solved first, followed by the diffusion step. In general, we can express Equation 3.8 as an initial value problem of the form:

$$\frac{\partial T}{\partial t} = \mathbf{L}(T) \quad (4.1)$$

where \mathbf{L} is an operator. Operator \mathbf{L} is generally nonlinear (e.g. due to thermally induced density anomalies that determine velocity for advection). Nonetheless, we can still write \mathbf{L} as a sum of two pieces:

$$\frac{\partial T}{\partial t} = \mathbf{L}(T) = \mathbf{Diff}(T) + \mathbf{Adv}(T) \quad (4.2)$$

where \mathbf{Diff} and \mathbf{Adv} are diffusion- and advection-operators, respectively.

To solve the equation numerically, we must discretize it in space and time. We choose to do the discretization in time first. Thus, the operator splitting will be applied to \mathbf{Diff} and \mathbf{Adv} before their discretization in space. This allows us to discretize different operators in space independently, using different methods.

We seek to find the numerical solution of time-discretized Equation 3.8:

$$\left(\frac{\partial^*}{\partial t}\right)T = \mathbf{Diff}(T, \Delta t) + \mathbf{Adv}(T, \Delta t) \quad (4.3)$$

where $\left(\frac{\partial^*}{\partial t}\right)$ is a discrete time-derivative, and Δt is the size of the timestep. If one of the operators, say **Diff**, was the *only* one standing on the right hand side, then we could express the update of T from timestep t^n to the next timestep t^{n+1} as:

$$\left(\frac{\partial^*}{\partial t}\right)T\Big|_{[t^n, t^{n+1}]} = \mathbf{Diff}(T(t^n), \Delta t) \quad (4.4)$$

Analogous expression can be found if **Adv** was the *only* one standing on the right hand side. The idea behind operator splitting method is that we update the variable T from one timestep to the next by allowing only one of the operators to act at a time, i.e. the operators are applied in an alternating manner. The total update of T after one timestep Δt can then be expressed as a sequence of updates:

$$\begin{aligned} \left(\frac{\partial^*}{\partial t}\right)T\Big|_{[t^n, t^{n+1/2}]} &= \mathbf{Diff}(T(t^n), \Delta t) \\ \left(\frac{\partial^*}{\partial t}\right)T\Big|_{[t^{n+1/2}, t^{n+1}]} &= \mathbf{Adv}(T(t^{n+1/2}), \Delta t) \end{aligned} \quad (4.5)$$

Notice how both operators act over a total timestep Δt , and it may appear that after performing the two steps, we find the solution at t^{n+2} , instead of t^{n+1} . This is not the case, however, since only a *part* of the original PDE is used in each of the steps. Equations 4.5 demonstrate how the general advection-diffusion problem stated in Equation 3.8 was split into a homogeneous conservation equation (diffusion) and a simple ODE (advection). Followingly, we can use numerical methods that are best suited for these specific problems, i.e. a high-resolution explicit method for the advection part and an implicit method for the diffusion part. In addition to the numerical errors associated with the advection- and diffusion-solvers of our choice, there arises an additional splitting error that depends on the timestep Δt . Only in some special problems, where the operators of the subproblems *commute* (meaning that they can be applied in any order), the splitting error is zero. In our case, however, the operators **Diff** and **Adv** are not commutative, and so the splitting error needs to be taken into account, posing a constraint on the size of the timestep.

Thermal Diffusion Solver

We use a fully implicit scheme for time-discretization of the thermal diffusion equation, which is unconditionally stable (with respect to timestep size). This means that for any arbitrarily large timestep, the errors introduced in each timestep do not grow out of bounds in the course of a simulations. In other words, the value of the solution remains within a given range and does not explode, or that any initial disturbance

of the temperature field will disperse, and not become unphysically more and more concentrated. At what cost do we get this convenient feature?

Let us, for simplicity, consider a one-dimensional diffusion equation:

$$\frac{\partial T}{\partial t} = \frac{\partial^2 T}{\partial x^2} \quad (4.6)$$

In our algorithm, we use FEM for discretization in space. To simplify the discussion in this section, we will consider discretization with FD in both space and time. The FTCS (Forward-Time Central-Space) scheme for Equation 4.6 is as following:

$$\frac{T_j^{n+1} - T_j^n}{\Delta t} = \left[\frac{T_{j-1}^n - 2T_j^n + T_{j+1}^n}{(\Delta x)^2} \right] \quad (4.7)$$

This scheme is first order accurate in time and second order accurate in space. The *von Neumann* stability analysis of this scheme grants an amplification factor ξ of the form:

$$\xi = 1 - \frac{4\Delta t}{(\Delta x)^2} \sin^2\left(\frac{k_w \Delta x}{2}\right) \quad (4.8)$$

where k_w is a real spatial wave number (of the eigenmodes of the difference Equations 4.7). The stability criterion $|\xi| \leq 1$ can thus be expressed as:

$$\frac{2\Delta t}{(\Delta x)^2} \leq 1 \quad (4.9)$$

Thus, a stable choice of the timestep Δt is dictated by the characteristic grid spacing Δx . Another way to interpret Equation 4.9 is that the maximum allowed Δt is given by the diffusion time across a cell of width Δx . This means that even if we were only interested in the part of the solution that is of lengthscale $\lambda \gg \Delta x$, we would still have to model the uninteresting smaller scales Δx . In general, this would require $\lambda^2/\Delta x^2$ steps to get to the part of the solution we are interested in.

The fully implicit (or backward in time) scheme avoids this timestep restriction by driving the disturbances that take place on the lengthscale below λ (but that are still resolved by Δx) to their equilibrium state. This means that temporal evolution of the thermal field on lengthscales that are smaller than the lengthscales that can be resolved with the given timestep, behave according to the time-independent diffusion equation. Thus, this small-scale part of the solution is spuriously decaying, and does not pollute the part of the solution that we are interested in. This is in contrast to an unstable FTCS scheme, where the temporally under-resolved part of the solution may spuriously grow and eventually overwhelm the interesting part of the solution. In problems where the solution tends towards a steady state, the numerical solution obtained with any size of the timestep, using the fully implicit scheme, will

eventually reach a steady state configuration, and the errors due to low temporal resolution will eventually die out. However, this is generally not the case for models of time-dependent mantle convection. A simple example to illustrate the significance of potential errors associated with time-step size in mantle convection simulations is as following. Envision an anomalously hot diapir (or plume) rising from the heated bottom of the mantle. What is the temperature of this thermal structure once it reaches the surface? The amount of its thermal anomaly determines two of the major plume-observables at the surface: the heat-flux, and the associated lithospheric uplift due to its thermally induced excess buoyancy. Accurate modelling of thermal diffusion rate while the diapir rises through the mantle has a direct effect on the prediction of its thermal anomaly at the surface. Although the Earth's mantle is a high Rayleigh number fluid, with diffusion timescales generally much larger than the convective timescales, accurate modelling of thermal diffusion is crucial for the correct prediction of the thermal boundary layers, which thickness determines the lengthscales of all the other thermal structures, such as the plume-heads and -tails. The lengthscale and magnitude of the thermal structures become even more important once we take into consideration the strong, exponential temperature-dependence of viscosity. As suggested by the analytical and experimental study of *Jellinek and Manga* (2004), the existence and stability of the long-lived hotspots in the mantle is determined by the thickness of the plume-tails, the magnitude of their thermal anomaly with respect to the ambient mantle, and the temperature-dependence of viscosity. More specifically, these parameters determine the rate at which new hot material is supplied to the plume tail, and the rate at which the material in the plume tail is cooling. If the modelled cooling rate is artificially enhanced due to a too large timestep, the too rapidly cooling plume-tail, as it also becomes more viscous, may prematurely choke off.

Stability of a numerical scheme is an obvious constraint. While the fully implicit scheme guarantees stability for any size of the timestep, its first-order accuracy poses limits on the size of the timestep that can be chosen for a given simulation. Insufficient time-resolution in models where small scale structures tend to develop, such as vigorous thermal convection simulations, can lead to erroneous damping of these parts of the solution.

4.2.2 Incompressible Stokes Equation for Multicomponent Flow

In the elements of the grid which are not cut by the material-interface - the material properties are defined unambiguously. However, elements that are cut by the compositional interface can pose a challenge when it comes to computing the velocity -

specifically in cases of materials with different viscosities. In isoviscous cases, viscous coupling ensures that flow variations induced by a compositional density anomaly are smooth. On the other hand, a viscosity jump across material interfaces produces a jump in the velocity-gradient, which is known to reduce the quality of the numerical solution of flow (Equation 3.6) (*Moresi et al.*, 1996; *Deubelbeiss and Kaus*, 2008; *Duretz et al.*, 2011). A jump cannot be represented with the smooth continuous shape functions used for spatial discretization of the velocity field (exception is the special case where element edges are aligned with the interface), and, at least in the vicinity of the interface, a relatively high grid-resolution is required in order to obtain a velocity solution with the desired level of accuracy.

Numerical simulations presented in this study do not feature jumps in viscosity, so we do not expand on this discussion here. There are, however, strong variations in viscosity present in our models, induced by its exponential dependence on temperature, but these are relatively smooth, and their approximation is helped by the adaptivity of the mesh to thermal gradients.

4.2.3 Thermal Advection Equation

Numerical modelling of advection of fields with large spatial gradients (e.g. Equation 3.8 at high convective vigor) is numerically challenging (*Lenardic and Kaula*, 1993). Typical errors include numerical diffusion, most prominent in low order or low resolution schemes, and dispersion errors, which may occur in higher order schemes. Different mathematical formulations of the left-hand side of Equation 3.8 - the advective component - lead to different numerical solution methods (*Gerya*, 2010). Eulerian formulation - the right hand side of Equation 3.12 - leads to an approach which utilizes a static grid for spatial discretization of the thermal field. A static grid is cheap to use from the computational point of view, as it only needs to be computed once for the entire simulation time, and ensures that the initial quality of the computational grid (e.g. shape of the elements in FE methods) is maintained throughout the simulation. On the downside, Eulerian advection schemes (at least the more simple ones) may suffer from numerical diffusion, which arises due to the repeated action of the interpolation procedure, as the advected field needs to be evaluated in points along its trajectory, which generally do not coincide with the computational nodes. When applied to advection of thermal fields, this can lead to artificial dissipation of sharp thermal gradients, and lead to an effectively lower convective vigor that is being modelled, compared to the one intended. In addition, Eulerian advection schemes pose a bound on the maximum size of the time-step that can be used, dictated by the CFL criterion.

Lagrangian formulation of the advective component of Equation 3.8 - the left hand

side of Equation 3.12 - leads to an advection scheme which utilizes a moving grid or markers (or both). The Lagrangian approaches are not (or less) prone to errors related to numerical diffusion, compared to their Eulerian counterparts, which gained them popularity in the geodynamic community. During the advection step of a Lagrangian scheme, positions of nodes - where the values of the advecting field are prescribed (e.g. markers or grid-nodes) - are updated, according to the computed velocity field. The field-values prescribed in the advecting nodes remain unchanged, and this is why Lagrangian methods can be considered a remedy against numerical diffusion. An additional advantage of the Lagrangian advection methods is that their stability is not limited by the size of the time-step (albeit their accuracy is). The Lagrangian methods of advection can be categorised into those where the computational mesh itself is advected with the flow, and those where a separate set of points - markers - are utilised for advection, while the grid is static. One of the difficulties associated with the former type of methods, is that a moving grid can become strongly deformed, or tangled, which deteriorates the quality of the PDE-solutions obtained on it. Remeshing procedure can be computationally expensive, and also leads to some numerical diffusion, as field-values must be interpolated from the old grid onto the new one.

In marker-methods, the grid is static, while markers, which carry properties of an initially prescribed field (e.g. temperature), get advected. Velocity field, which is computed on the static grid, is interpolated onto markers in order to compute their trajectories. The advection step is followed by a communication step - where the updated field values (carried by the markers) are communicated to the computational grid (nodes and/or element-interiors). Thermal field is mapped from markers to the grid in order to perform the thermal diffusion step (computed on the grid), and to update the thermal contribution to the buoyancy term on the right-hand side of the momentum conservation equation (also solved on the grid). Mapping of the thermal field back and forth between the markers and the grid can give rise to some numerical errors. First of all, it introduces some numerical diffusion, although it can be significantly diminished if only the incremental temperature changes are mapped between the different sets of points, rather than the full field-values (*Gerya and Yuen, 2003*). Another problem is related to the different length-scales that can be resolved by the markers and the grid (resolution of the former typically higher than that of the latter, by at least an order of magnitude). In the course of simulation, as some regions of the material get stretched and thinned, markers may form thermal structures that are smaller than what can be resolved by the grid. Consequently, the subgrid-scale thermal structures are not captured by the grid-controlled diffusion process, and thus fail to dissipate away. They do, however, continue to contribute to the thermally induced density anomaly on the right hand side of the momentum equation - which collects information from all markers irrespective of the scale of the structures they represent. The overall effect may be an overestimated vigor of convection, or, in the

worst case - unstable growth of thermal anomalies. A remedy against this numerical artifact, induced by the variable resolution of markers and the grid is presented in (Gerya and Yuen, 2003). It involves a correction step that follows the thermal diffusion operation. In the correction step, the subgrid-scale diffusion is accounted for in the grid-nodes, prior to transferring the updated temperature values onto markers.

4.2.4 Compositional Advection Equation

Equation 3.9 describes advection of a discrete compositional field. Similar to the thermal field discussed in previous section - the compositional field can be discretized using a static or moving grid, or markers. The first representation is used if advection is performed with a Eulerian approach, and the two latter ones for the Lagrangian advection-schemes. For a compositional field, an interface separating two materials represents a discontinuous jump, or an infinitely large compositional gradient. Thus, advection of such field is an extreme case of advection of a function with sharp gradients (infinite in this case).

Using Eulerian scheme for advection of a compositional field gives rise to similar types of problems as were discussed in the previous section: numerical diffusion and dispersion (Lenardic and Kaula, 1993), but the numerical diffusion error manifests itself in a different way. During Eulerian advection of a continuous function (e.g. temperature), the numerical errors associated with interpolation lead to artificial dissipation of sharp gradients - numerical diffusion. Interpolation of a discrete function (e.g. an indicator function used for compositional fields), on the other hand, boils down to determining where in the intermediate node-positions one material ends, and the other begins (the uncertain location of the interface). The interpolation error thus manifests itself as an erroneous location of the interface - or an erroneous distribution of the materials. In the course of a simulation, the volume-fraction of different materials may artificially change due to the interpolation errors.

Errors due to the uncertainty of the location of the interface can be avoided when using the interface tracking methods for advection. Marker-chain method is one such approach, where rather than discretizing the volume of each material, only the interface separating the materials is discretized by a connected set of markers. Together with the boundary of the domain (as well as boundaries around holes within the domain, if such are present), the marker-chain (or multiple chains) constitute closed polygon-boundaries which enclose the regions spanned by each material. The global positions of markers, as well as their respective positions in a chain (neighbor-relations) constitute the discretized representation of the compositional field.

Advection of discrete fields happens via advection of the markers in a chain. Marker-chain method does not require interpolation of the compositional field during the ad-

vection step, eliminating the numerical diffusion and dispersion errors at this stage. In order to compute the velocity field, the material properties need to be communicated to the grid (in FEM - to the locations of integration points) on which the Stokes system of equations is solved. This is done by determining which polygon each integration point falls into, optionally followed by some averaging procedure of the values in integration-points (e.g. arithmetic, geometric or harmonic mean (*Schmeling et al.*, 2008)), or a linear least squares approximation (*Thielmann et al.*, 2014)).

Throughout the simulation, interface separating the materials gets deformed. In cases where the interface gets stretched and entangled, addition of new markers along the chain may be required, in order to properly resolve the increasingly complicated geometry of the interface. Conversely, some markers may be removed from smooth interface-regions or where neighboring markers get clustered.

Some of the difficulties associated with the marker-chain method involve development of subgrid-scale material structures, which may not have any integration points falling into them, thus being completely invisible to the grid. This may not produce a significant error in isoviscous materials with moderate compositionally induced density variations, since velocity-variations induced by such (geometrically) small anomalies are also small. However, a thin interconnected filament of a material with anomalous viscosity may induce strong variations in the velocity field, and ignorance of the grid to such structures may result in significant error.

Methods which utilise a moving grid Lagrangian approach for advection of a compositional field typically have the edges of grid-elements positioned along the interface. One can think of this discretization as similar to the marker-chain method, but with an additional feature that neighboring markers in the chain comprise some of the element-edges. Thus, the location of the interface is known with certainty - requiring no interpolation in the course of advection. Followingly, these methods do not suffer from numerical diffusion. There are other technical difficulties associated with this method, however. First of all, as was already mentioned in previous section, a moving and deforming grid can become prohibitively entangled. While remeshing can sometimes provide a remedy to this issue, forcing the element-edges to be aligned with the interface can produce a grid with a prohibitively large number of elements - and thus degrees of freedom - rendering the method impractical.

Another problem associated with the moving grid Lagrangian advection schemes is related to the representation of the interface with straight element-edges. In cases where the geometry of the interface develops strong curvature, it may become increasingly poorly approximated with the straight element-edges, which makes the material appear effectively stiffer. An example of a numerical simulation where this artifact influences the solution is presented in (*Schmeling et al.*, 2008), where a cusp-like geometry develops between a modelled slab subducting beneath an overriding mantle. This problem can be circumvented by adapting the number of nodes - or

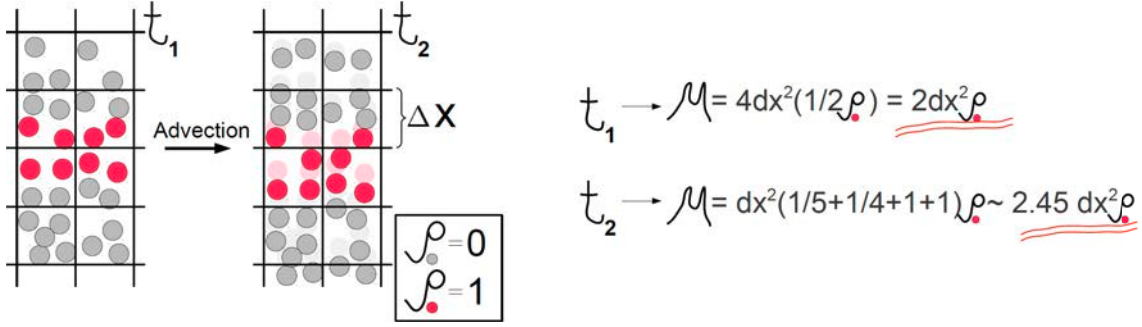


Figure 4.3: Illustration of how mass-conservation can be violated in tracer-ratio methods, due to statistical ‘noise’. The sketch shows evolution of compositional field from time t_1 to a later time t_2 . Tracers (filled circles) represent different materials, which differ in their intrinsic density ρ . Gray tracers represent material with $\rho = 0$, and pink tracers $\rho = 1$. The density-distribution as seen by the grid is computed by averaging ρ -values of the markers within each grid-cell (outlined with black lines). The mass of each cell is given by the product of averaged density with the cells area (Δx^2). Equations on the right show the total mass computed for the two density distributions shown in the figures on the left.

element-edges - along the interface to its curvature.

Markers in Cell

Methods using markers in bulk for discretization of the compositional field can be categorized into two groups: *absolute tracer* method and the *tracer ratio* method, each with their own advantages and limitations. A detailed comparison of the two methods in the light of thermochemical mantle convection simulations can be found in (Tackley and King, 2003). A brief outline, largely based on (Tackley and King, 2003) and (Gurnis, 1986), is given in the following.

In the absolute tracer method, the tracers represent only one of the materials (say the anomalous one), and have a finite volume (and mass) associated with them. The compositional field within grid-nodes or -cells is determined based on the local density of the tracers. Grid cells that are devoid of tracers represent the ambient material. Cells that contain the maximum number of tracers that can fit within a cell (according to the volumes associated with a cell and a tracer) represent the compositionally anomalous material. The fraction C_i of the anomalous material within a grid cell, here denoted by subscript i , can thus be expressed as:

$$C_i = \frac{N_i}{N_{\max}} \quad (4.10)$$

where N_i and N_{\max} are the number of tracers in cell i and the maximum number of tracers that fit in a cell, respectively. Note that tracers are viewed as material-patches of finite extent during the transfer of chemical information from tracers to grid cells (Equation 4.10). This is generally not the case during the advection step, where tracers are treated as points (i.e. they are infinitesimal) in space that advect with the velocity field interpolated onto them from the Eulerian grid. This can lead to geometrical overlapping of the tracers when they are viewed as patches again, allowing more than N_{\max} to enter one cell, and resulting in unphysical fraction-values $C_i > 1$. The mass of the model, however, remains conserved, being a constant property associated with each tracer.

In the tracer ratio method, tracers fill the entire domain. They have a discrete value associated with them (like 0 or 1 in case of only two materials) that determines which material they represent. The fraction of the materials within a grid cell is determined from the ratio of each type of tracers within that cell, scaled by the total number of tracers in that cell. The fraction of the anomalous material within a cell can thus be expressed as:

$$C_i = \frac{N_i^1}{N_i^0 + N_i^1} \quad (4.11)$$

where N_i^1 and N_i^0 are the number of anomalous-material and ambient-material tracers within cell i , respectively. The ratio method guaranties $C_i \not\geq 1$. On the downside, as tracers advect in the course of simulation, their distribution throughout the domain may become inhomogeneous, which can for example lead to different cells having different number of markers falling into them. The non-uniform marker-distribution may lead to errors in the fraction of materials that is ‘seen’ by the grid, and thus the total apparent mass of the materials present in the system. These errors manifest as violation of mass-conservation, as is graphically illustrated in Figure 4.3. A larger number of markers decreases their associated statistical ‘noise’ (e.g. variation in marker-density per cell between 1 and 2 is much more significant (50%) than variation between 101 and 102 ($\sim 1\%$)), and thus also the discrepancies in the apparent material-distribution ‘seen’ by the grid.

In the numerical benchmarking study of (*Van Keken et al.*, 1997), it was shown that the discretization ‘noise’ can influence the solution, and is more pronounced for lower number of markers. In their study, the absolute marker-method was used to perform simulations of flow driven by compositional density anomaly. The authors showed that lower number of markers results in more small-scale instabilities (secondary and tertiary diapirs in Rayleigh-Taylor benchmark). Errors that arise due to marker-discretization ‘noise’ may be strongly reduced by using the tracer-ratio method, as was proposed by (*Tackley and King*, 2003). Nonetheless, (*Tackley and King*, 2003) also showed that lower number of markers in the tracer-ratio method results in more

small-scale instabilities.

In order to compute the velocity field, material properties must be interpolated from the markers to the grid. This involves the same difficulty related to interpolation of discrete fields as was discussed for the Eulerian advection methods. The material-distribution, and thus material-properties like viscosity and density, seen by the grid is polluted by the interpolation error, which enters the resulting solution of the momentum equation - the velocity and pressure fields. Thus, the velocity field with which markers subsequently advect suffer from the interpolation error due to transferring material-properties from markers to the Eulerian grid.

Similar to the marker-chain method discussed above, subgrid-scale structures may develop in the markers-in-bulk methods as well. In (*Tackley and King, 2003*), the authors point out that although one may discretize subgrid-scale structures with markers, it is still important for the grid-resolution to capture the active (in terms of density) compositional length-scale. (*Gurnis, 1986*) modelled subduction and segregation of a compositionally dense oceanic crust to the bottom of the lower mantle with an absolute marker-method, where the oceanic crust material is discretized using one marker along its width, rendering the length-scale of the prescribed compositional anomaly smaller than the Eulerian grid scale. This is justified by considering the settling (or Stokes) velocity of the modelled oceanic crust (given its size and compositional density anomaly) with respect to the characteristic convective velocity. The former is much smaller than the latter, implying that as long as the large scale convective flow is resolved (by the grid), the numerical solution captures the dominant dynamical effects. If the ambient flow is such that it accumulates anomalous tracers in some regions, such that they form larger structures, they may have a stronger influence on the ambient flow. Despite a relatively large discretization error associated with one marker wide subgrid-scale structures of the compositional field, the quality of the solution is still reasonable, as it is dominated by the dynamics of other fields, such as temperature, which have larger length-scales and are sufficiently well resolved. Modelling approach in (*Gurnis, 1986*) illustrates an important point when it comes to dealing with discretization errors. The smaller the length-scale of a structure - the larger is the discretization error associated with it (for a given number of points). At the same time, for isoviscous simulations with density being the only compositionally induced effect - as is the case in (*Gurnis, 1986*), the smaller the length-scale of a structure - the smaller is its effect on the large-scale dynamics - and thus its contribution to the error of the final solution. Note that this argumentation does not hold if compositional variations also induce variations in viscosity, since variations in the latter may induce highly localised variations in the velocity field.

The lack of connectivity between markers renders them robust and cheap for representation of material-structures, whose geometry may be too complex to be efficiently represented by a grid with a similar number of nodes. However, representation of

discrete fields with markers comes at a price that the location of the interface is not well defined. One example that illustrates potential artifacts arising due to the uncertainty of the interface-geometry in marker-methods goes as following. An increasingly thinned and stretched compositional structure may eventually have only one marker along its width. Further stretching simply creates larger distances between the markers aligned with what ideally should be a connected filament. When the distance between neighboring markers becomes greater than one element, the grid on which the velocity is solved no longer sees the structure as a connected filament, but rather as isolated droplets. This is a problem, because the bulk properties of materials with different viscosities is significantly different depending on whether the anomalous phase is distributed as droplets, or as interconnected filaments (*Karato, 2008*). This artifact related to subgrid-scale resolution may occur in the limit of low marker-density, but keeping in mind that compositional structures undergoing viscous deformation have no limiting length-scale (we disregard effects of surface-tension), this numerical artifact may pose a constraint on the total simulation time. Similar to the moving grid and marker-chain advection-schemes, where an increasingly deformed interface may require adding new interface-points for its sufficiently accurate representation, addition of new markers may be required in marker-methods to discretize compositional structures that get stretched and thinned.

4.3 Communication from Markers to Grids

Using Lagrangian points, such as markers, for modelling advection, together with a Eulerian grid on which mass, momentum and diffusion equations are solved, necessitates transferring of information from the Lagrangian points to the Eulerian grid (grid-nodes or integration points in elements). To keep the discussion general, we formulate this task as transferring information from points on which compositional or thermal fields are defined, to an arbitrary location within the domain.

4.3.1 Voronoi Diagram and Delaunay Triangulation

Markers are points in space without any connectivity prescribed to them. They are distributed approximately homogeneously throughout the entire domain and have assigned a function-value that is to be found in their exact location. Transferring information from markers to an arbitrary point within the domain is non-trivial, because markers have no interpolation rule, or connectivity, associated with them (in contrast to a computational grid). Efficient algorithms for navigating within such

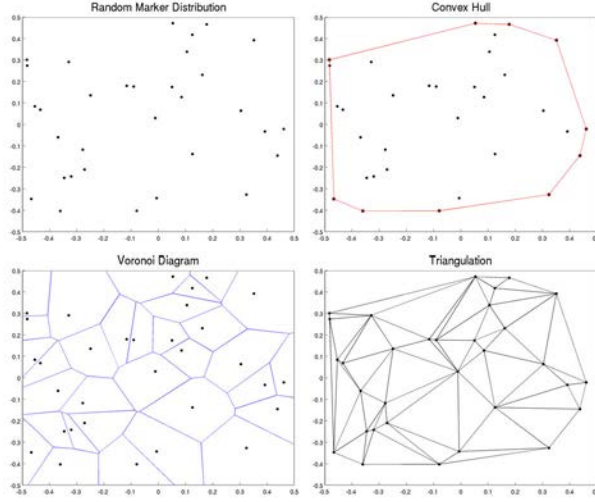


Figure 4.4: Top left: *Example of a random marker-distribution.* Top right: *Convex hull of the marker-distribution.* Bottom left: *Voronoi diagram of the marker-distribution.* Bottom Right: *Triangulation of the marker-distribution.*

scattered sets of points (e.g. finding the closest neighbors, triangulating, etc.) are known from the field of computational geometry. These concepts have been used extensively in meshless methods for constructing various scattered data interpolants. Details of these algorithms are beyond the scope of our study. We will, however, discuss the use of some of the most fundamental geometrical constructs related to irregular sets of nodes: the Voronoi diagram, and its dual Delaunay triangulation. In addition, we will make use of background meshes, referred to as ghost meshes, similar to the ones used in Element-Free Galerkin method of (*Belytschko et al.*, 1994) for their quadrature procedure. We emphasise that we use the aforementioned geometrical constructs only for the purpose of interpolation, and, in contrast to the meshless methods, not for the construction of discrete equations.

Figure 4.4 illustrates an example of a set of randomly distributed points (markers) and its associated Voronoi diagram. For a given set of markers, the Voronoi diagram is unique, and consists of cells, or Voronoi polygons, associated with each marker (markers that constitute the convex hull of the set have unbounded polygons associated with them). A Voronoi polygon possesses the property that an arbitrary point in its interior is closer to the marker associated with the polygon, than to any other marker within the set. This property may be harvested to find the nearest marker of an arbitrary point within the domain. Given an arbitrary point within the domain, we can determine which marker is its closest neighbor by comparing (or sorting) its distances to all other markers. Alternatively, we can do it with the help of a Voronoi

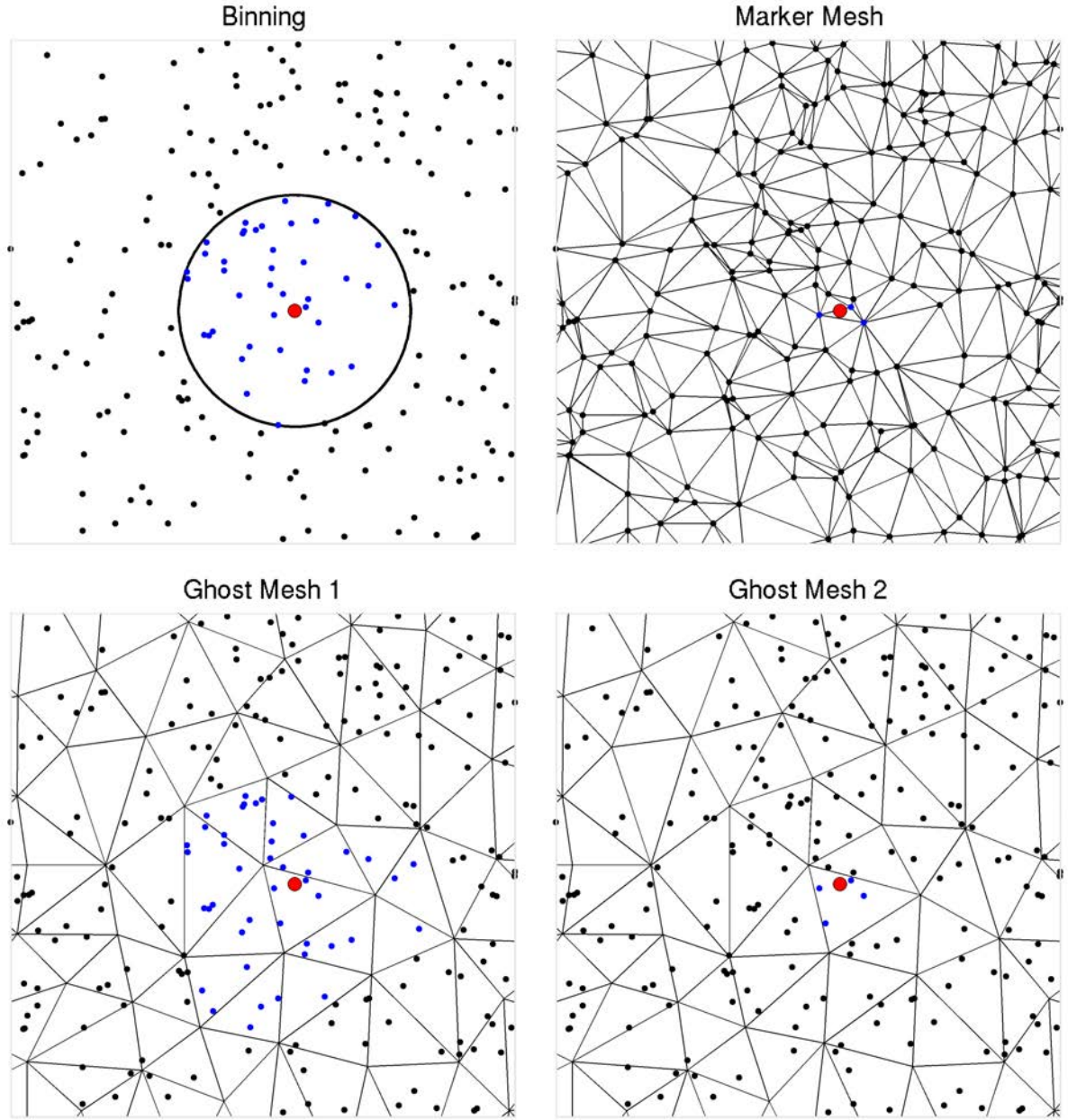


Figure 4.5: Visualization of different methods for transferring information from markers (black dots) to an arbitrary point of interest (red circle). Markers whose values play a role in determining the value in the point of interest are colored blue. A special case of the binning method (top left) is the nearest neighbor method, in which case the radius of the bin is equal to the distance between the sampling point and its closest marker. In the bottom row, the black edges are the ghost mesh elements.

diagram, by checking which Voronoi polygon the point of interest falls into: the marker associated with that polygon is thus the closest neighbor.

For illustration of the concept of interpolation from markers via a Voronoi diagram, we present examples in Figure 4.6. Cases of markers representing both discrete and continuous functions are shown.

A connectivity between markers can be introduced via triangulation: construction of triangular facets with markers at their vertices. A Delaunay triangulation constructed from a set of randomly distributed markers is shown in the bottom right of Figure 4.4: markers constitute vertices, joined by non-intersecting straight-line segments. The resulting triangular unstructured mesh can be used for interpolation (like in FE methods) from markers to anywhere in the interior of their associated convex hull. The convex hull spanned by the markers is generally a subset of the total computational domain (because markers are located in the domain-interior). Therefore, to construct a marker-triangulation that spans the entire domain, we must place some auxiliary markers on the domain-boundary. The function-values prescribed in the original markers must then be extrapolated to the boundary-markers. The procedure for generating the auxiliary boundary-markers that is used in this study goes as following: the outermost markers (e.g. those falling within a given distance from the domain boundary) are projected onto their nearest domain-boundary - the projections become the locations of the auxiliary boundary markers, and the function-values of the projected markers become the values of their respective boundary markers. Original markers that get to be projected are chosen such that the distance between the neighboring boundary-markers is close to a characteristic distance between the original markers, and such that the outermost points of the domain boundary (e.g. corners of a box) get a marker projected onto them. The resulting marker-mesh can be used analogous to a finite element mesh, with linear shape functions for interpolation in the regions between the markers.

Mesh generation routines normally insert points additional to the ones prescribed, in order to satisfy mesh-quality constraints (such as maximum area or minimum angle of the triangles). In the course of marker-triangulation, however, we don't want any new markers to be inserted. Banning additional points leads to a generally poor quality of the marker mesh, which is partially why one wouldn't attempt to solve the differential equations on that mesh. The only place where we have to introduce some additional markers is along the boundary of the computational domain, as was already discussed.

For transferring information from the markers to an arbitrary point within the domain, we treat the marker mesh as linear finite elements. First, we find which marker-element the point of interest falls into. Then, we use first-order shape-functions associated with marker elements to interpolate from the three markers at the corners of the element to the point of interest.

For illustration of the concept of interpolation from markers via a constrained Delaunay triangulation, we present examples in Figure 4.6. Cases of markers representing both discrete and continuous functions are shown, together with the resulting values in the boundary-markers.

Implementation and Computational Time

To construct marker-triangulation, as well as vertices constituting segments of the Voronoi diagram, we use *Triangle* by *Shewchuk* (1996). Alternatively, the Voronoi diagram can be generated using MATLAB-function ‘voronoin.m’. Computational time required to generate a Voronoi diagram with ‘voronoin.m’, to generate a Voronoi diagram and a marker-mesh with *Triangle*, and to generate the boundary-markers needed for the latter, is shown in Figure 4.7 for a range of numbers of markers. The computational time of ‘voronoin.m’ and *Triangle* both scale as $O(N\log N)$, where N is the total number of markers, and is an optimal scaling for these procedures (*Shamos and Hoey*, 1975). The generation of boundary-markers is computationally least demanding of the three. Notably, computational time required to generate a Voronoi diagram and a mesh from a scattered set of points (markers) becomes prohibitively expensive (2 – 20 seconds for the more efficient *Triangle*) when the number of points grows from 10^6 – 10^7 . As will be shown in the benchmarking part of this chapter, in Section 4.4, such high number of markers is necessary for accurate simulation of global scale thermochemical mantle convection (even in 2D) with the marker-in-cell methodology.

4.3.2 Binning

In the two interpolation-methods described above only one (for Voronoi diagram) or three (for Delaunay triangulation) markers are used to evaluate a function in the point of interest. In the binning method presented in this section, the number of contributing markers is more flexible. A bin is a region - e.g. circle of a given radius, or circle that includes a given number of markers - centered on the point of interest. The function-value in the point of interest can be determined using markers that fall into its respective bin. A constant bin size generally results in a different number of markers being enclosed by each bin, including the possibility of empty bins. An adaptive bin-size, on the other hand, ensures to include a constant number of markers, but the length-scale of interpolation becomes less well-defined. The minimum adaptive bin size is the distance to the closest marker, and leads to the nearest neighbor approach.

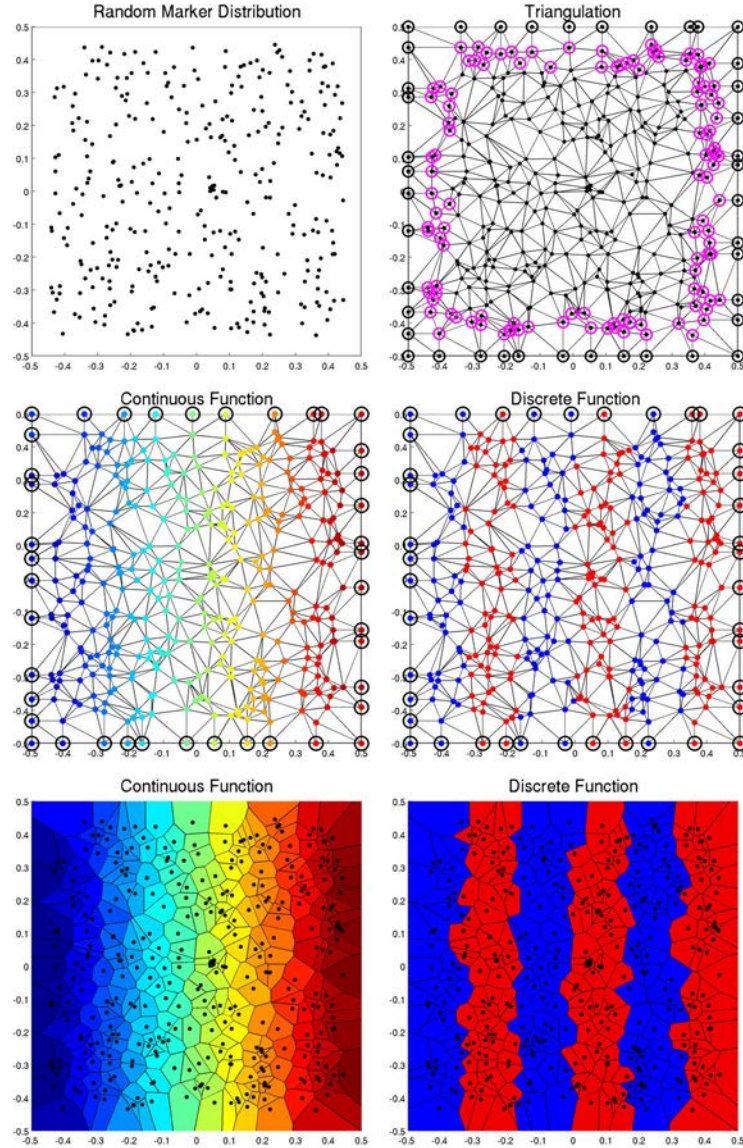


Figure 4.6: Triangulation and a Voronoi diagram constructed from markers. Construction of a marker-triangulation that spans the entire domain necessitates placing some auxiliary markers on the domain-boundary. The top right plot illustrates which markers from the original set were used for generating boundary markers (magenta-rims), and the locations of the resulting boundary markers (black rims). Center row: marker-colors indicate values of continuous (left) and discrete (right) functions. Auxiliary boundary-markers are encircled by black rims. Bottom row: Voronoi polygons are colored according to the continuous (left) and discrete (right) function-values in their respective markers.

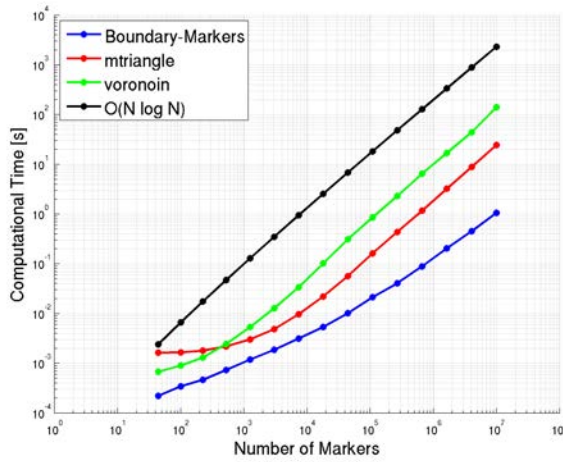


Figure 4.7: Computational time required to generate a constrained Delaunay triangulation and a Voronoi diagram using Triangle (`mtriangle` in the legend), as well as a Voronoi diagram using MATLAB-function `voronoin.m` (`voronoin` in the legend) from a scattered set of points (markers). Construction of a marker-triangulation that spans the entire domain necessitates placing some auxiliary markers on the domain-boundary. The procedure for generating boundary-markers is described in the text, with an example presented in Figure 4.6, and its required computational time is presented in the figure here. Results for different numbers of markers are shown. A line that illustrates scaling as $O(N \log N)$ is shown for reference, where N corresponds to the values along the x -axis.

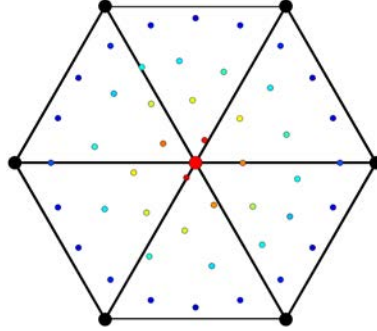


Figure 4.8: Illustration of markers (small circles) whose host-elements (black edges) share a node (central large red circle). Marker-colors indicate their weight on the shared central node: blue means lowest weight, and red means highest weight. For each marker, its weight on the central node is the value of the shape function associated with that node, computed at the markers location. The value of the shape function reflects the distance from the marker to the node: the smaller the distance - the larger the value of the shape-function.

Depending on the size of the bins, it is possible that there are markers without a parent-bin. Alternatively, a single marker can belong to several bins, in cases where bins overlap. This limits the efficiency of algorithms for finding which markers belong to each bin, so we found this method to be too costly to implement.

If, on the other hand, the bins are not allowed to overlap, each marker can only have one bin that it falls into. Once that bin has been found, we never have to check that marker again to find out whether it belongs to any other bin. Additionally, if the cumulative area of the bins spans the entire domain, there will be no orphaned markers who don't get to contribute their information. The requirements of non-overlapping bins that span the entire domain bring us to the ghost-mesh methods in the following section.

4.3.3 Ghost Mesh Methods

In general, the spatial resolution associated with markers is the highest one in the numerical model, compared to the resolutions of the computational grids on which the conservation equations are solved. An interpolation scheme that transfers information from markers to an arbitrary location within the domain with an accuracy dictated by the marker-resolution (such as the case for Voronoi diagram and Delaunay triangulation methods) may thus be unnecessarily expensive. Additionally, highly local interpolation schemes result in only a fraction of markers contributing to the final

result, with the information carried by the rest of the markers being completely ignored. To reduce the computational effort associated with interpolating from markers to the interior of the domain, we introduce the concept of a ghost mesh.

The ghost mesh serves as an auxiliary mesh, with a prescribed connectivity between its nodes, and with the number of nodes less than the number of markers. We can define interpolation functions associated with each node of the ghost mesh elements, analogous to shape functions in the finite element method. The field carried by the markers is mapped onto ghost mesh by collecting the contributions from all the markers into its nodes. The resulting field can be further interpolated from the ghost-mesh to anywhere within the domain. The ghost mesh does not have to coincide with any of the computational meshes on which the conservation equations are solved, but it can naturally represent those meshes as well. In addition, the ghost-mesh can be adapted to enhance the accuracy of interpolation in some regions (e.g. compositional interfaces or strongly varying temperature).

Ghost mesh methods are similar to the binning method described above, only the bins are the elements of the ghost mesh. The main difference is that we no longer require for the bins to be centered on the points of interest, they are not allowed to overlap, and their cumulative areas span the entire domain.

In the methods described hereafter, we use an unstructured ghost mesh with triangular elements. It allows more flexibility with respect to the geometry of the domain and mesh adaptivity, compared to structured meshes. We describe two approaches for transferring information from markers to points of interest with the help of a ghost mesh. Common for both methods, the shape functions associated with the ghost-mesh elements are used to estimate distances from markers to ghost-mesh nodes, or from ghost-mesh nodes to the points of interest. With linear triangular ghost-mesh elements, values of three shape-functions are computed in the location of markers or points of interest, and reflect the distance between the latter and each of the three nodes of their hosting ghost-mesh element. Values of the shape-functions thus reflect the relative weights that each marker has on the three nodes of its host-element, or weights that each node of a ghost-mesh element has on the points of interest in its interior.

Navigation and information-transfer between markers, ghost-nodes and sampling points in ghost mesh method (1) includes the following two steps: first, evaluating the function carried by the markers in *all* ghost-mesh nodes, and then interpolating these values from ghost-mesh nodes onto the point of interest. To evaluate the function carried by the markers in a given node - we collect the contributions from markers in *all* the elements that share this node, as is graphically illustrated in Figure 4.5. The contributions from markers are weighted by their distances to the node, obtained from the values of the shape-functions in markers' locations, as is graphically illustrated in Figure 4.8. The obtained field-values are then transferred from ghost-mesh nodes to

the point of interest.

Ghost mesh method (2) differs from ghost mesh method (1) in the choice of markers that get to contribute to the nodes of the ghost-mesh, and thus also to the points of interest. In ghost mesh method (2), we only collect contributions from the markers that are within the same element as the one hosting the point of interest, as is graphically illustrated in Figure 4.5. Thus, in ghost mesh method (2), we do not prescribe a unique function-value to each ghost-mesh node, in contrast to what is done in ghost mesh method (1). In ghost mesh method (2), a node that is shared by several elements gets assigned a different function-value, depending on what element we are currently looking at (or what element the point of interest falls into). Thus, the only markers contributing to the point of interest are those that are found within the same element. Information-transfer from the ghost mesh nodes onto the point of interest is the same as in ghost mesh method (1).

Ghost Mesh Methods: Implementation

We implemented the two ghost-mesh methods in the following way:

1. Create a ghost mesh using MUTILS-function ‘mtriangle.m’.
2. Determine the host-element of each marker (i.e. which ghost-element each marker falls into), using MUTILS-function ‘tsearch2.m’.
3. Compute values of the shape-functions in marker-locations (e.g. using MUTILS-function ‘einterp.m’ to find the barycentric marker-coordinates w.r.t. their host-element). Values of the shape-functions in each marker-location act as relative weights that each marker has on the three nodes of its host-element.
4. Determine which element the point of interest falls into, again using ‘tsearch2.m’.
5. Compute values of the shape-functions in the point of interest, again using ‘einterp.m’ and ‘shp_deriv_triangle.m’. Values of shape-functions reflect the weight on the point of interest from each of the three nodes of its host-element.
6. Transfer function-values from markers to ghost-mesh nodes:
 - (a) **Ghost mesh method (1):** Each node collects contributions from all the markers that fall within the elements that share this node. In-built MATLAB-function ‘accumarray.m’ is used for this procedure, output of which is a vector with one entry for each ghost-mesh node.

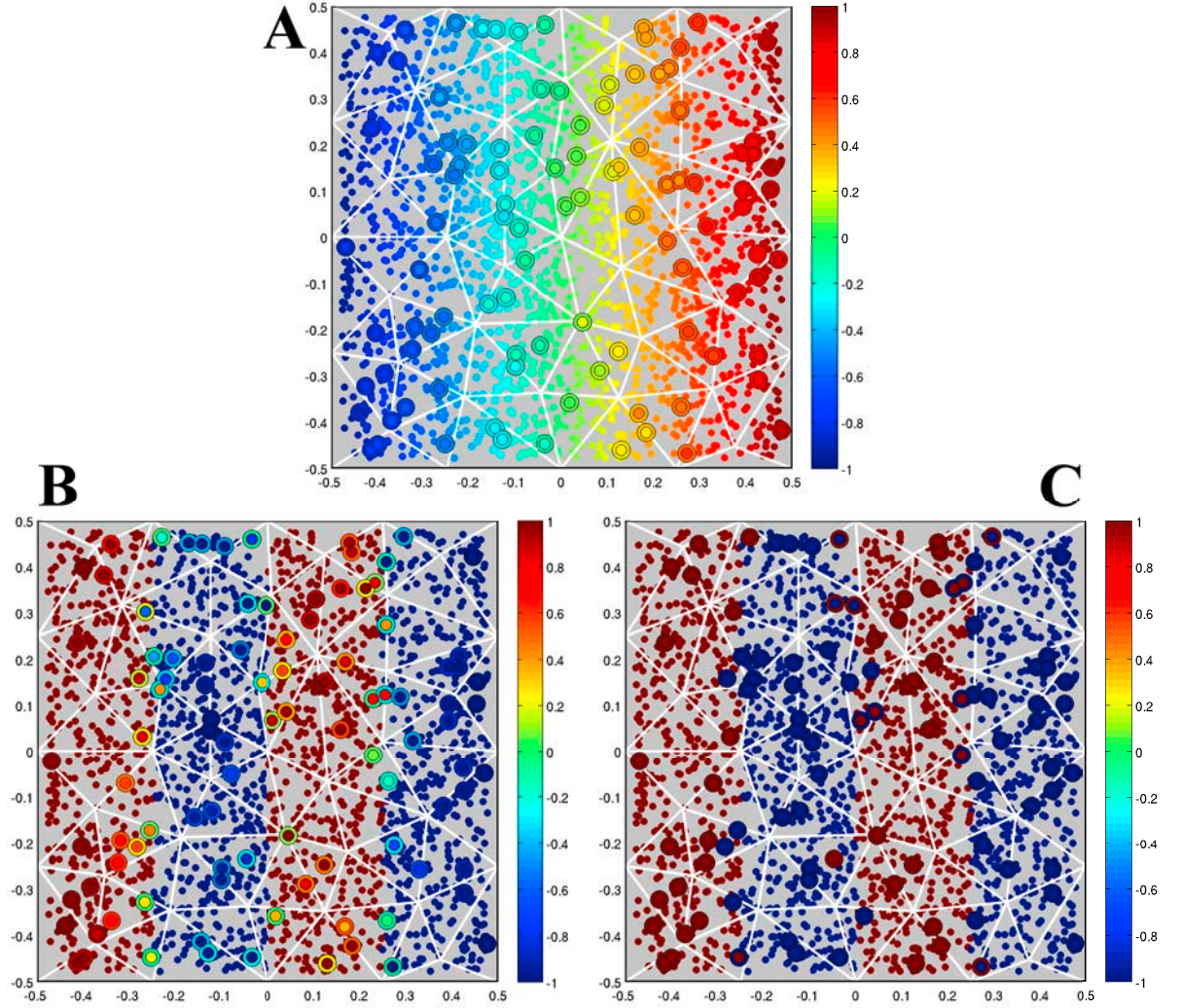


Figure 4.9: Example of transferring function-values from markers (smallest circles) to arbitrary points of interest (big and small concentric circles with black rims) via a ghost mesh (triangular elements indicated by white edges). Results obtained with the ghost-mesh method (1) (biggest circles with black rims) and ghost-mesh method (2) (smaller circles with black rims) are shown. A: markers represent a smooth continuous function. B: markers represent a continuous function with jumps. C: markers represent a discrete function.

- (b) **Ghost mesh method (2):** Nodes of an element collect contributions only from the markers that fall within that element. In-built MATLAB-function ‘accumarray.m’ is used for this procedure, output of which is a vector with three rows (three nodes per element), and as many columns as there are elements in the ghost mesh.

In steps 6a and 6b, transfer of function-values from markers to nodes depends on the type of function carried by the markers:

- (a) **If markers carry a continuous function:** Value in a ghost-mesh node is the distance-weighted average from its contributing markers.
 - (b) **If markers carry a discrete function:** Value in a ghost-mesh node is the value of the marker with the biggest weight on that node.
7. Transfer function-values from the ghost-mesh nodes to the point of interest:
- (a) **If markers carry a continuous function:** Interpolation analogous to FE methods with triangular first-order elements, using MUTILS-function ‘einterp.m’.
 - (b) **If markers carry a discrete function:** Only the node with the biggest weight contributes to the point of interest.

Figure 4.9 illustrates the different results obtained with the ghost-mesh methods (1) and (2) for three different types of functions that can be carried by the markers: continuous functions that are smooth or have jumps in them (both can be interpolated or averaged), and discrete functions (which cannot be interpolated or averaged). The results illustrate that when markers carry a smooth function, ghost-mesh methods (1) and (2) yield similar results for the function-values obtained in the points of interest. When markers carry a continuous functions with jumps, ghost-mesh method (2) produces less smearing than ghost-mesh method (1), as is most apparent in the points of interest close to the function-jumps. When markers carry a discrete function, the two ghost mesh methods produce different results in some of the points of interest that are close to the interfaces. Also in this case, ghost-mesh method (2) appears to capture the discontinuity in function-values better than ghost-mesh method (1).

Ghost Mesh Methods (1) and (2): Systematic Comparison

We compare the performance of the two ghost mesh methods for transferring both discrete and continuous functions from markers to arbitrary positions in the interior of the domain (referred to as points of interest, and which are generally more numerous than markers). Figure 4.10 exemplifies a discrete function that is used for the

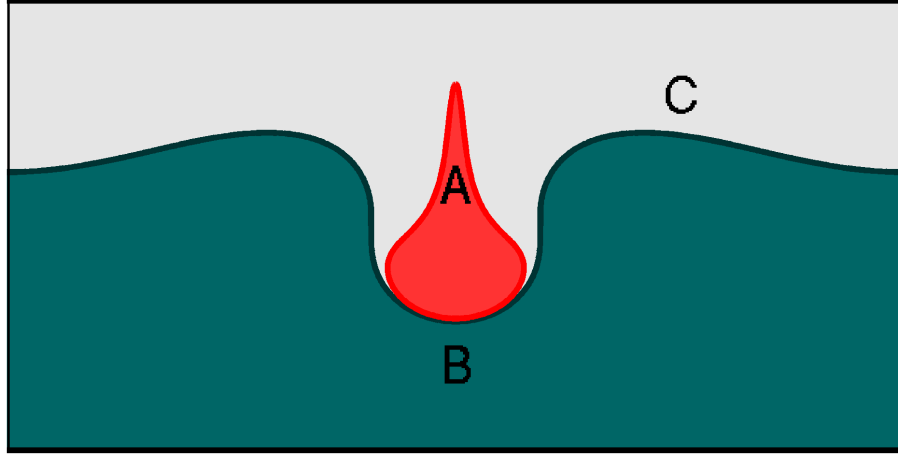


Figure 4.10: Example of a material distribution: colors (and letters A, B and C) indicate regions occupied by different materials. Material distribution field is discrete, meaning that its range of values constitutes a countable set. In this example, the field can assume values A, B, or C, but no intermediate values, or values outside of this set.

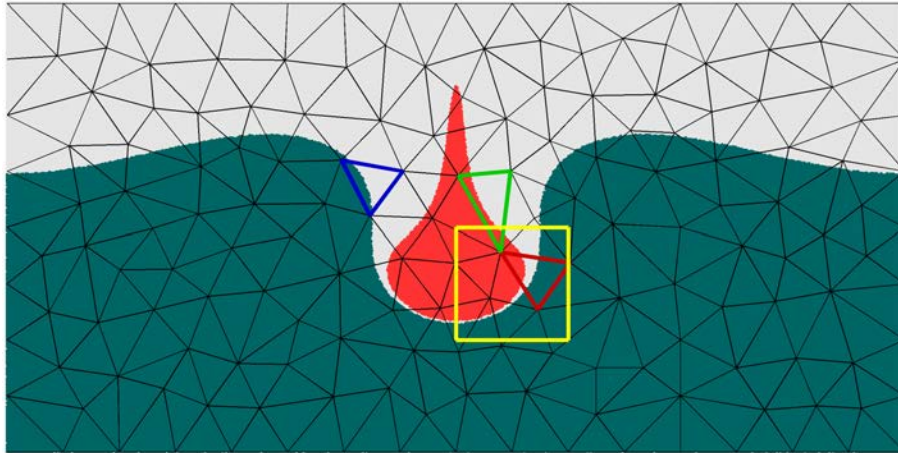


Figure 4.11: This figure illustrates markers colored according to the materials they represent (original field in Figure 4.10). A ghost mesh is shown as triangular elements with black edges, and is used for transferring information from markers to arbitrary points within the domain. The three elements with edges colored red, green and blue are those in which results are showed in detail in Figure 4.14. The results obtained in the region enclosed by the yellow square for four different ghost-mesh resolutions are shown in Figure 4.15.

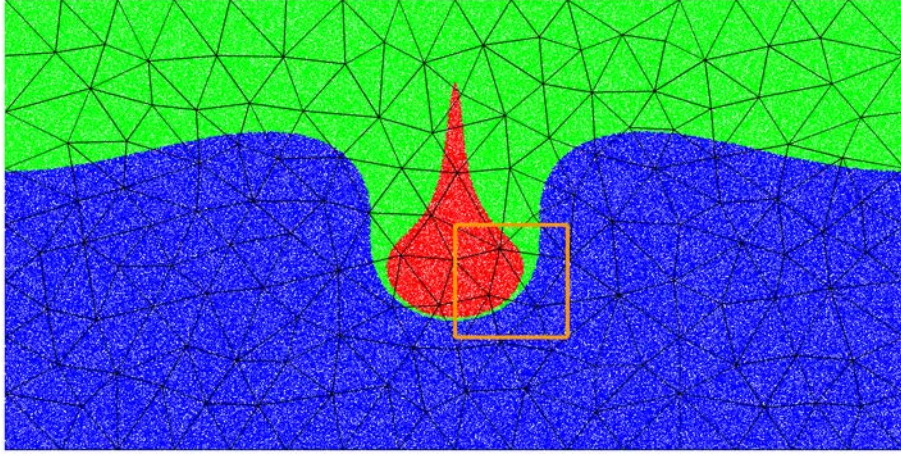


Figure 4.12: Markers colored according to their prescribed values of a **continuous function** with jumps (e.g. red = 1, green = 0.5, and blue = 0). A ghost mesh is shown as triangular elements with black edges, and is used for transferring information from markers to arbitrary points within the domain. Ghost mesh methods are described graphically in Figure 4.5. The results obtained in the region enclosed by the orange square for four different ghost-mesh resolutions are shown in Figure 4.17.

comparison, while Figure 4.12 exemplifies a continuous function with jumps. As a reference, results obtained with the nearest neighbor approach (for the discrete function) and marker-triangulation approach (for the continuous function) are presented in Figure 4.13 (only a fraction of the domain is shown to visualize the details).

For the discrete function, the result shown in Figure 4.13 demonstrates that the compositional field is correctly identified in most regions. However, in regions close to the interface (by approximately a characteristic marker-distance), some discrepancy may be observed. This is not a surprising result, and is a direct consequence of the fact that in marker-discretization methods interfaces are not well-defined. Consider a general case, with an interface passing somewhere between two markers of different material-types. The interface can be arbitrarily close to one marker or the other. An arbitrary point which lies between the two markers has no way of knowing which side of the interface it is on, and simply assumes that the interface lies exactly in the middle between the two markers, which can lead to errors.

In many cases where the exact description of the interface is not crucial to the simulation result, we can live with errors dictated by the characteristic marker-distance (which is generally much smaller than the characteristic distance between the nodes of the computational mesh). Typical examples of when it is important to accurately compute interface-geometry, specifically its curvature, are applications where surface tension plays a significant role. In most large-scale geodynamical applications, how-

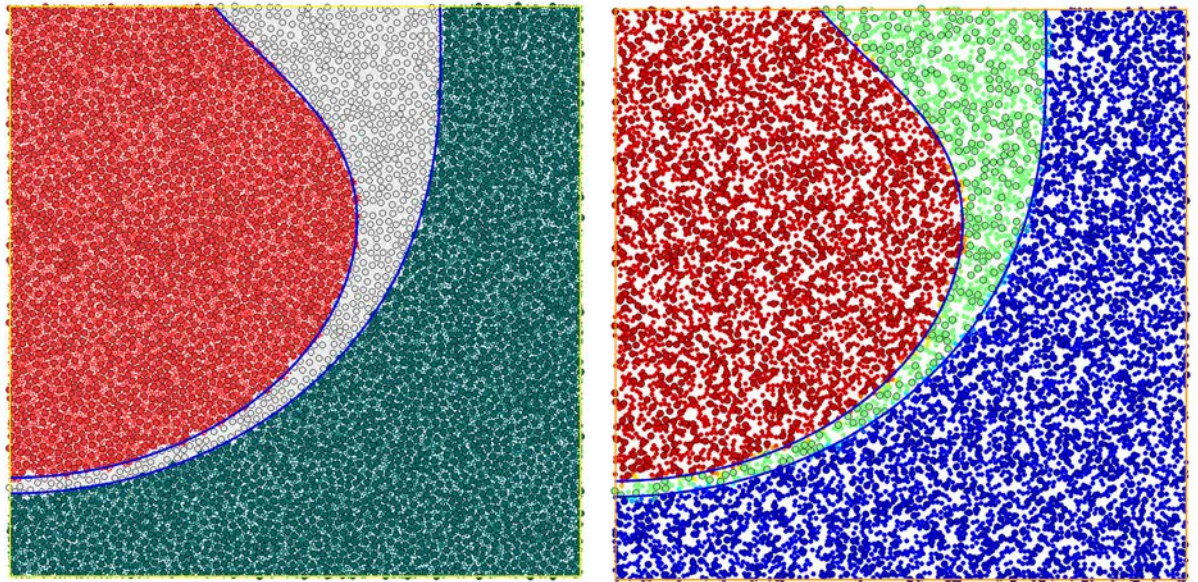


Figure 4.13: Discrete and continuous functions evaluated in the points of interest, by transferring information from the markers. Left: The discrete field is transferred from markers to points of interest with the nearest neighbor approach. Right: The continuous field is transferred from markers to points of interest with the marker-triangulation approach. Markers are the larger circles with black edges, while the smaller dots are the arbitrarily spaced points of interest.

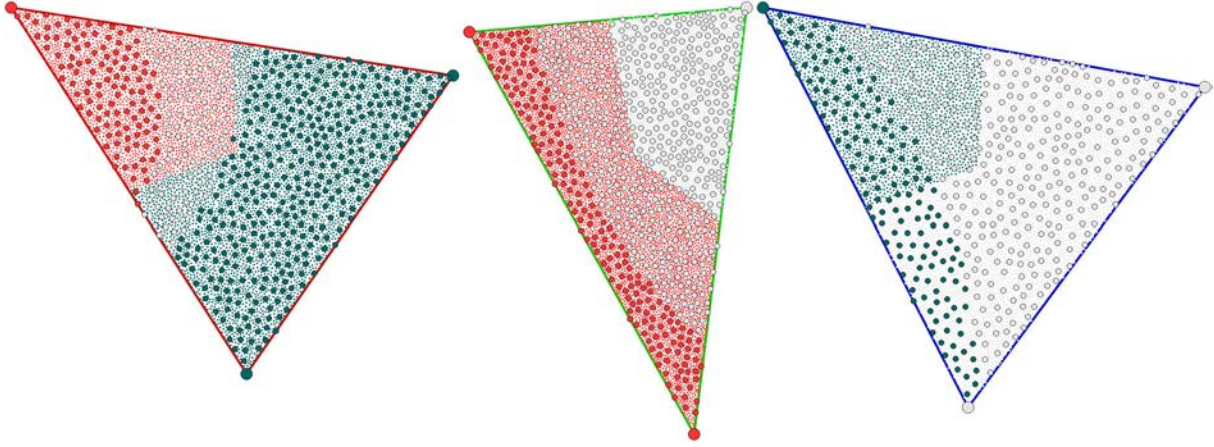


Figure 4.14: Illustration of the field C obtained with the ghost mesh method (1). Materials prescribed in the markers are shown as medium-sized circles with black edges, materials as seen by the nodes of the ghost mesh are shown as large circles with black edges at the vertices of the elements, and materials as seen by the arbitrary points in the interior of the elements is shown as the smallest circles, or dots.

ever, effects of surface tension can be ignored.

For the continuous function, the result shown in Figure 4.13 demonstrates that the field appears to be correctly identified almost everywhere, except for the regions within a characteristic marker-distance away from the interfaces. Sampling points that fall within marker elements containing a function-jump get an intermediate value of the field, as a result of linear interpolation from the markers. This produces some smearing of the jump due to interpolation-errors. The length-scale of this artificial smearing decreases with increasing marker resolution.

Markers Carry a Discrete Function

Figure 4.14 illustrates the compositional field obtained with ghost method (1) in the three elements that are highlighted in Figure 4.11. Prescribed field-values in the markers, as well as the resulting values in the nodes of the ghost-mesh and homogeneously distributed sampling points are shown. One of the elements (leftmost in Figure 4.14) contains markers of three different phases in its interior. However, the nodes of the elements get to ‘see’ only one marker each - the ones that are closest to them. Thus, the material represented by the markers closer to the center of the element, and further from the corner nodes, is invisible to the ghost-element. As a result, the sampling points overrepresent two of the materials found in this element, and completely ignore the third material. The element in the center of Figure 4.14

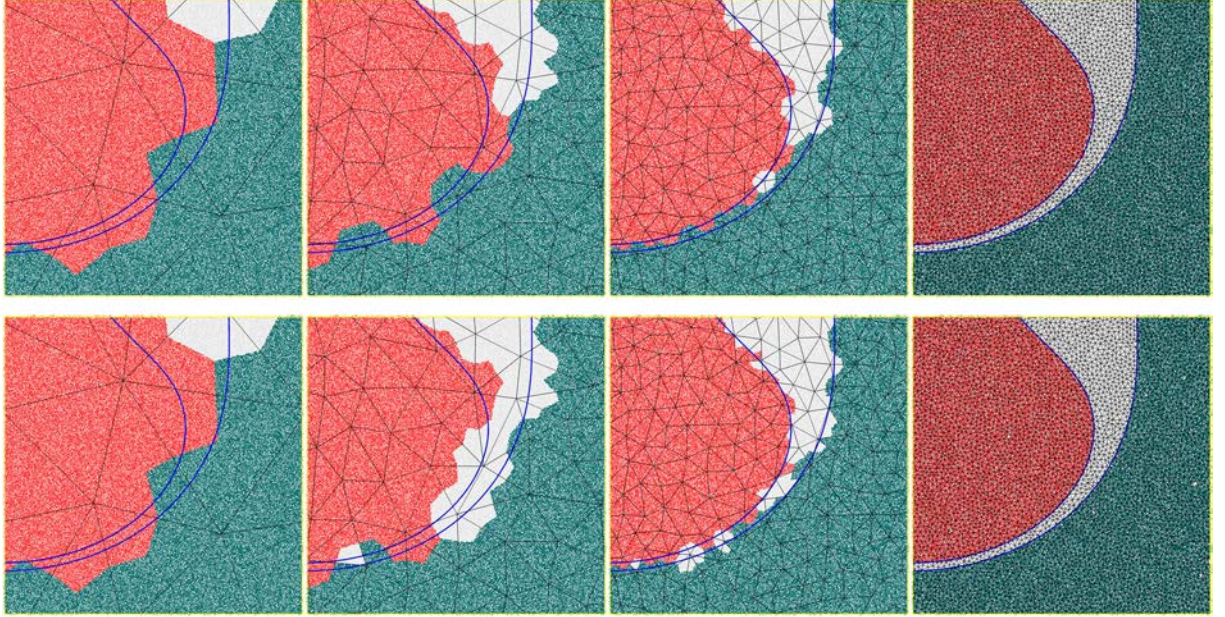


Figure 4.15: Materials as seen by the arbitrary points (colored dots), obtained with the ghost mesh method (1) TOP and (2) BOTTOM. Marker-distribution (not shown in these figures, but is the same as in Figure 4.13) is the same in all plots. Ghost-mesh resolution increases towards the right.

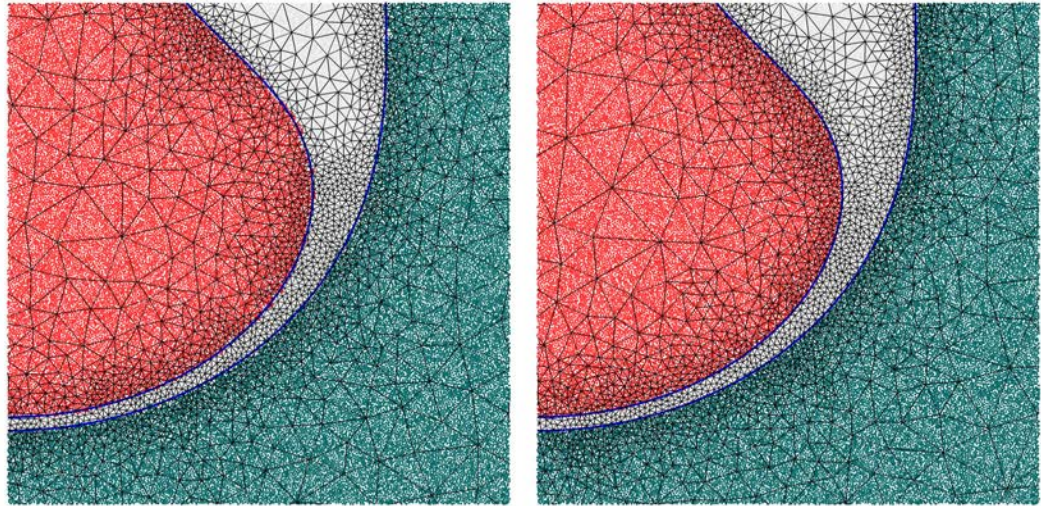


Figure 4.16: Materials as seen by the arbitrary points (colored dots), obtained with the ghost mesh methods (1) (left) and (2) (right), using a ghost mesh that is refined in regions close to the interfaces.

demonstrates how fraction of two different materials in one elements can be wrongly estimated as a result of ‘miscommunication’ between the markers and the sampling points. Similar numerical artifact can be observed in the rightmost element of Figure 4.14, where mis-representation of the interface (interface is not shown, by can be assumed looking at the markers) is also evident. These three types of artifacts: an invisible phase, wrong fraction of the materials, and inaccurate geometry of the interface, are common in marker methods. It is the result of markers having a generally higher spatial resolution than what can be resolved by the grids (ghost and/or computational).

The larger scale effects of the numerical artifacts associated with ghost-mesh methods (1) and (2) can be seen in the plots of Figure 4.15, which shows the compositional field obtained for four different ghost mesh resolutions. For lowest (left-most) and highest (right-most) ghost-mesh resolutions, the two methods yield similar results. In the right-most plots of Figure 4.15, where the ghost-mesh elements are smaller than the thinnest material structure in the model, the result looks similar to that of the nearest neighbor approach. Ghost mesh method (2) appears to be more successful at capturing all three materials for intermediate resolutions.

It is apparent from the results in Figure 4.15 that the resolution of the ghost-mesh largely controls the quality of interpolation from markers to arbitrary points within the domain. This property allows us to vary the accuracy of interpolation in different regions of the domain, by adapting the size of the ghost-elements accordingly. It is, for example, desirable to have small ghost-elements in regions where markers with different properties are close together (i.e. material interfaces), and large elements in regions occupied by the same type of markers. Figure 4.16 shows the compositional fields obtained with ghost mesh methods (1) and (2), using an adaptively refined ghost mesh.

Markers Represent a Continuous Function

Like for discrete methods, we present two ghost-mesh approaches for continuous functions. The results are presented in Figure 4.17. At low resolutions, ghost-mesh methods (1) and (2) produce quite different results. Ghost-mesh method (1) results in much smoother field than ghost-mesh method (2). The field-jumps obtained with ghost-mesh method (2), however, are not aligned with the original interfaces, and ghost-mesh method (2) is therefore not considered to be less numerically diffusive. Both methods converge to the same result with increasing ghost-mesh resolution.

In summary, the length-scale of the interpolant effectively used by ghost-mesh method (1) is greater than that of ghost-mesh method (2) when interpolating field-values carried by the markers onto an arbitrary point within the domain. This results in greater

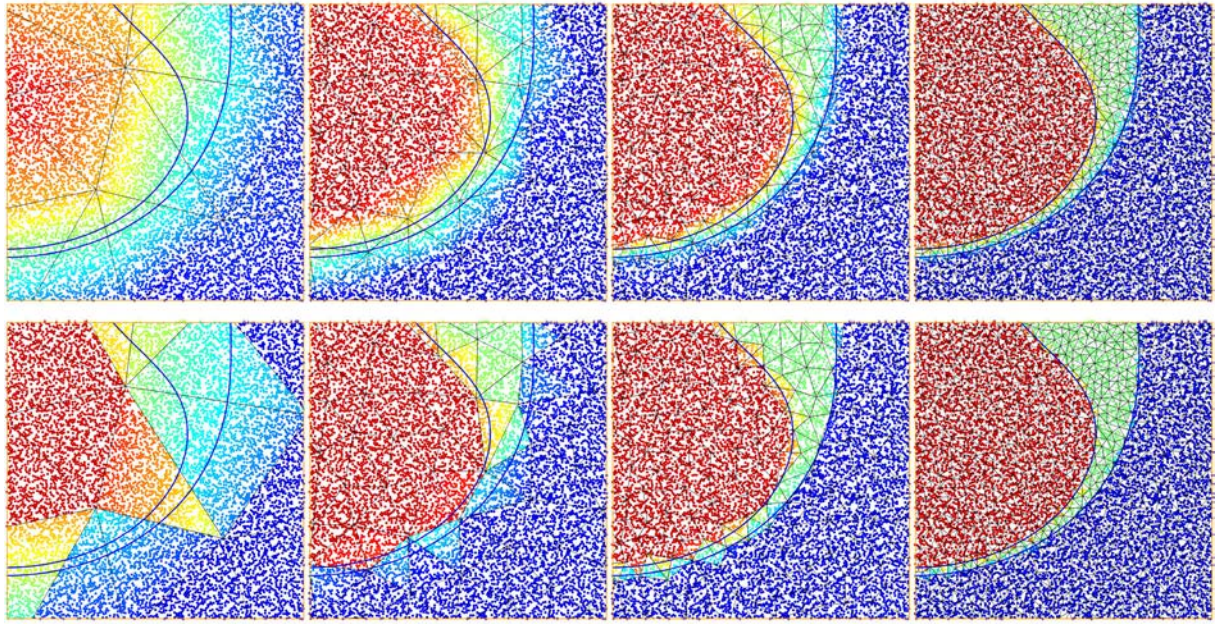


Figure 4.17: Continuous field as seen by the arbitrary points (colored dots), obtained with the ghost mesh method (1) TOP and (2) BOTTOM. Marker-distribution (not shown in these figures, but is the same as in Figure 4.12) is the same in all plots. Ghost-mesh resolution increases towards the right.

smoothing of the interpolated field produced by ghost-mesh method (1) (especially across element-edges), than the one produced by ghost-mesh method (2). For ghost meshes whose element-edges are (even approximately) aligned with the jumps in field-values carried by the markers - the ghost-mesh method (2) is clearly preferable to ghost-mesh method (1). However, when the ghost mesh elements feature no such adaptation, ghost-mesh method (2) produces spurious jumps across element-edges. Influence of such ‘non-smooth’ interpolation error on the subsequent solution of the fields thermal and mechanical evolution is more difficult to asses, compared to the interpolation error produced by ghost-mesh methods (1), where it is not sensitive to the geometry of the ghost-elements, other than their size.

4.3.4 Communication from Markers to Grids: Our Algorithm

We chose to use the ghost-mesh method (1) for communication from markers to grids in our algorithm, with the thermal mesh acting as the ghost mesh, as we found it to be the most practical compromise between the required computational time and the accuracy of information-transfer from markers to arbitrary points within the domain. The thermal mesh elements are generated by splitting each mechanical element into six triangles. Thus, Step 1 of the algorithm presented in Figure 4.1 involves transferring information from markers to the nodes of the thermal mesh, and subsequently from the nodes of the thermal mesh to the integration points of the mechanical mesh. Properties that get transferred from markers to the grid are temperature (a smooth continuous function, exemplified in Figure 4.9(A)), and compositionally induced variations in density (a continuous function with jumps, exemplified in Figure 4.9(B)).

4.4 Benchmark-Results

Performance of our code in modelling the governing processes of thermochemical convection, i.e. flow driven by compositionally and thermally induced density variations, is analyzed using benchmarks that are common in the geodynamic community, results of which are presented in this section.

4.4.1 Rayleigh-Taylor Benchmark

We solve the isoviscous Rayleigh-Taylor instability problem, where the fluid flow is driven by the compositionally induced density variations, as described in *Van Keken*

et al. (1997). The flow is described by Equations 3.6, 3.7 and 3.9. Two methods for advection of the compositional field are compared: (i) tracer ratio method, and (ii) marker chain method. In method (i), projection of the compositionally induced density variations from markers to the integration points of the mechanical elements is done using ghost-mesh method (1), described above.

In method (ii), composition in integration points of the mechanical grid is determined by checking which polygon the given point falls into (two closed polygons made up by the material interface and the boundary of the box enclose the two materials). Mechanical grid is generated after each time step, such that all segments of the material-interface constitute element-edges (i.e. interface never crosses element-interior). At each time step, we check the distance between the neighboring markers in the chain and add new markers in order not to increase the initially prescribed distance. We do not remove any nodes along the interface.

All simulations are performed using a small enough timestep ($\Delta t = 10^{-2}$), such that increasing the time resolution (i.e. decreasing the timestep) does not change the simulation result.

Quantities that are calculated for benchmarking are the following:

- (i) Root-mean-square velocity as a function of time:

$$v_{rms} = \sqrt{\frac{1}{V} \int_V \|v\|^2 dV} \quad (4.12)$$

where V is the area of the computational domain.

- (ii) Relative entrainment of the lower layer as a function of time:

$$e = \frac{1}{\lambda d_b} \int_{d_e}^1 C dV \quad (4.13)$$

where $\lambda = 0.9142$ is the aspect ratio of the box $d_b = 0.2$ is the thickness of the lower and compositionally buoyant layer, $d_e = d_b$ is the depth above which entrainment is measured, and C describes spatial distribution of different materials, with $C(\vec{x}) = 1$ if \vec{x} is occupied by the buoyant material, and $C(\vec{x}) = 0$ otherwise.

- (iii) Maximum value of the root-mean-square velocity and time at which the maximum value is reached.

In addition, we test the self-consistency of each method by comparing the total amount of the buoyant material ‘seen’ by the mechanical grid at the beginning and end of each simulation. This value should be approximately constant throughout the

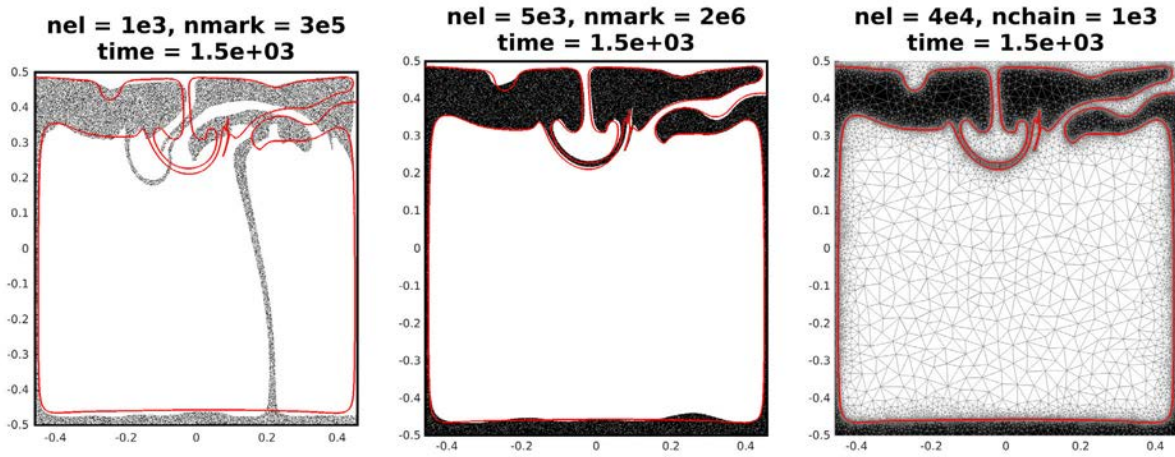


Figure 4.18: Comparison of the results for the Rayleigh-Taylor benchmark obtained with the tracer-ratio methods at two different resolutions (first two figures), and those obtained with the marker-chain method with a conforming grid, at time $t = 1500$. For the latter, the mesh is shown with gray lines delineating element-edges. The red line delineates the marker-chain, and is plotted for comparison in all three figures. Resolutions are given in the titles of each figure, where ‘nel’ means number of mechanical elements, ‘nmark’ number of markers in the tracer-ratio method, and ‘nchain’ number of markers in the marker-chain method.

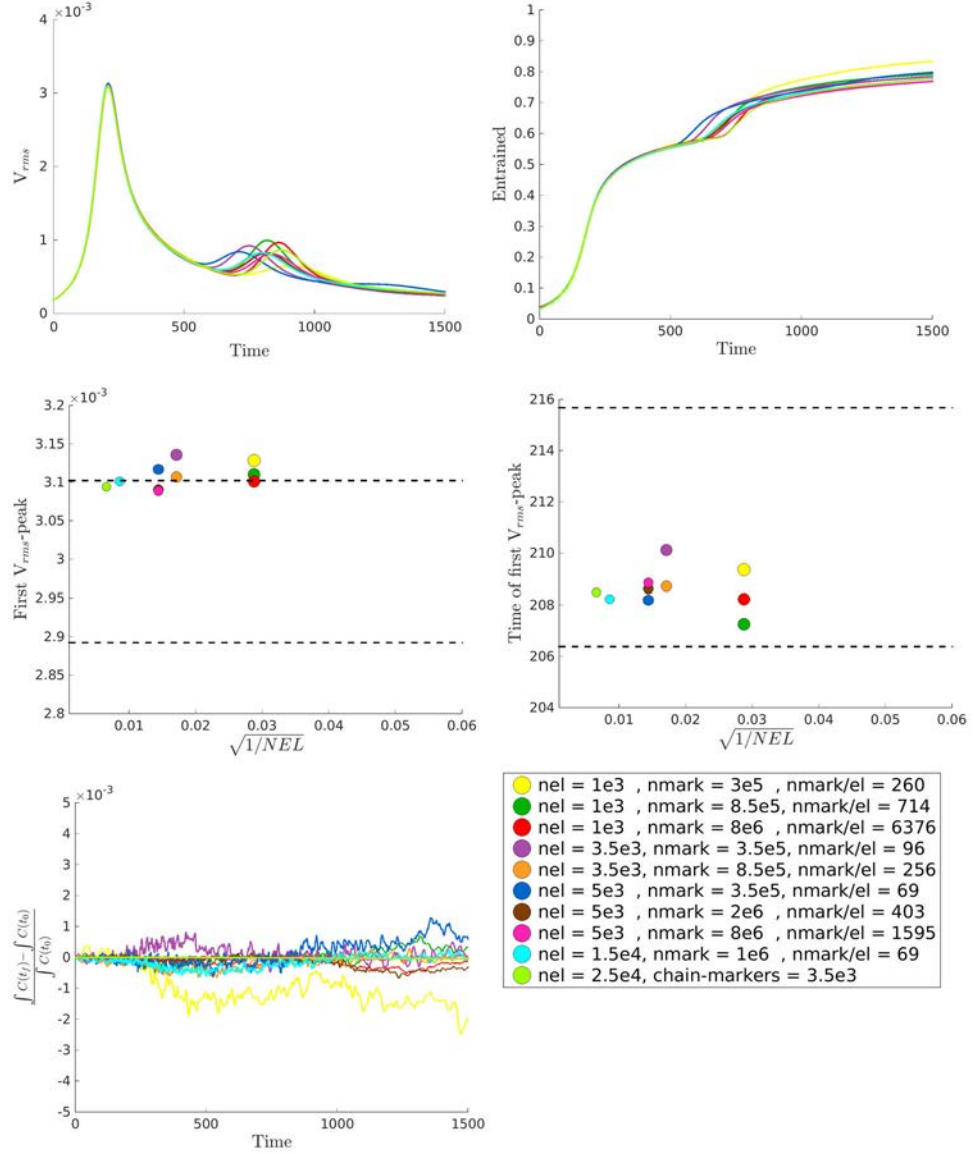


Figure 4.19: Benchmark-quantities for the isoviscous Rayleigh-Taylor instability set-up, obtained with the tracer-ratio method at different resolutions (according to legend) and marker-chain method with a conforming grid. In the legend, ‘nel’ means number of mechanical elements, ‘nmark’ number of markers in the tracer-ratio method, and ‘nchain’ number of markers in the marker-chain method. Black dashed lines in plots showing values and points in time of the first v_{rms} -peak (middle row) indicate the range of values for the respective quantities presented in Van Keken et al. (1997).

simulation, and any trend in this value over time would indicate an error in mass-conservation.

Figure 4.18 shows an example of the modelled compositional field at the end of the simulations obtained with the tracer-ratio methods at two different resolutions, and those obtained with the marker-chain method with a conforming grid. For the latter, the mesh conforming to the material interface is also shown for illustration. The left-most plot of Figure 4.18 shows an erroneous distribution of compositional field, which evolves when the spatial resolution (both markers and mechanical grid) is too low. At higher spatial resolutions - larger number of mechanical elements and markers - the solution converges towards the same result as the one produced with the method of marker-chain with conforming mechanical mesh.

Figure 4.19 shows time-evolution of the benchmark-quantities. Increasing divergence with time of the results obtained with different methods and resolutions is apparent both in the measured v_{rms} and entrainment values. This was also observed in the results published for this benchmark in *Van Keken et al.* (1997). The value and time of the maximum root-mean-square velocity, also shown in Figure 4.19, suggests that results obtained with increasing numbers of markers and elements in the tracer-ratio method approach the results obtained with the marker-chain method with a conforming grid. The error in the total amount of the buoyant material ‘seen’ by the mechanical grid for the tracer-ratio method is within 0.25%, and decreases with increasing resolution. For the marker-chain method, this error is below 0.01%.

Results of this benchmark demonstrate the importance of having a sufficient number of markers when modelling advection of compositional fields with tracer-ratio method, in order for the statistical ‘noise’ associated with marker-discretization not to dominate the solution. According to the results presented in Figure 4.19, up to 100 markers are needed for the isoviscous Rayleigh-Taylor instability set-up. For comparison, *Tackley and King* (2003) find that for the isoviscous benchmarks, using 40 markers per cell gives results that are within the range of those published in (*Van Keken et al.*, 1997).

4.4.2 Thermal Convection Benchmark

We solve the problem of isoviscous thermal convection in a box at Rayleigh number $Ra = 10^6$, as in case 1(C) in *Blankenbach et al.* (1989). This problem is described by Equations 3.6 - 3.8. Quantities that are calculated for benchmarking (at a time after the system has reached a dynamic steady state) are the following:

- Nusselt number:

$$Nu = \frac{\int_0^l \partial_z T(x, z = h) dx}{-\frac{\Delta T}{h}} \quad (4.14)$$

where l and h are the width and the height of the box, respectively.

- Root-mean-square velocity:

$$v_{rms} = \sqrt{\frac{1}{V} \int_V \|v\|^2 dV} \quad (4.15)$$

where V is the area of the computational domain.

Figure 4.20 shows an example of the modelled thermal field at dynamic steady-state. We compute the benchmark case using both uniform meshes, and meshes that are adapted to have smaller elements in regions of high thermal gradients. In both cases, thermal mesh elements are generated by splitting each mechanical element into six triangles. We vary the total number of elements, as well as the number of markers that are used for temperature-advection. As initial conditions for temperature, we use a precomputed result from a convection simulation. We run the simulation until a dynamic steady state is reached, which is the point in time when the computed benchmark-quantities may still be oscillating, but there is no trend in the value about which these oscillations occur. All simulations are performed using a small enough timestep ($\Delta t = 10^{-6}$), such that increasing the time resolution (i.e. decreasing the timestep) does not change the simulation result.

Results of the benchmark, presented in Figure 4.21, demonstrate the importance of having a sufficient number of markers when modelling thermal convection with the characteristics based marker-in-cell method. In the presented cases, at least 100 markers per element are needed. When the static grids are too coarse to resolve the active length-scales of the model (in this case, thickness of the thermal boundary layers), increasing the number of markers does not improve the result. The opposite is also valid: when there aren't enough markers to accurately represent and communicate to the grid the evolution of thermal field due to advection - increasing the number of elements does not improve the result. A small number of markers per element leads to a larger amplitude of oscillation of benchmark-values around the mean. This is a manifestation of statistical 'noise' associated with markers-discretization, which increases with decreasing number of markers per element. This effect is especially pronounced in the benchmark-results obtained with meshes that are adapted to have smaller elements in regions of high thermal gradients. There is a large amplitude of oscillations around the mean Nusselt-value in cases where the lower part of the range for number of markers per element is below 10. This is understandable, because Nusselt-number is measured at the top boundary of the domain, where thermal gradients are the largest, and thus where elements are the smallest: with approximately uniform marker-distribution, regions with the smallest elements have the lowest number of markers per element, and a significant associated statistical 'noise'.

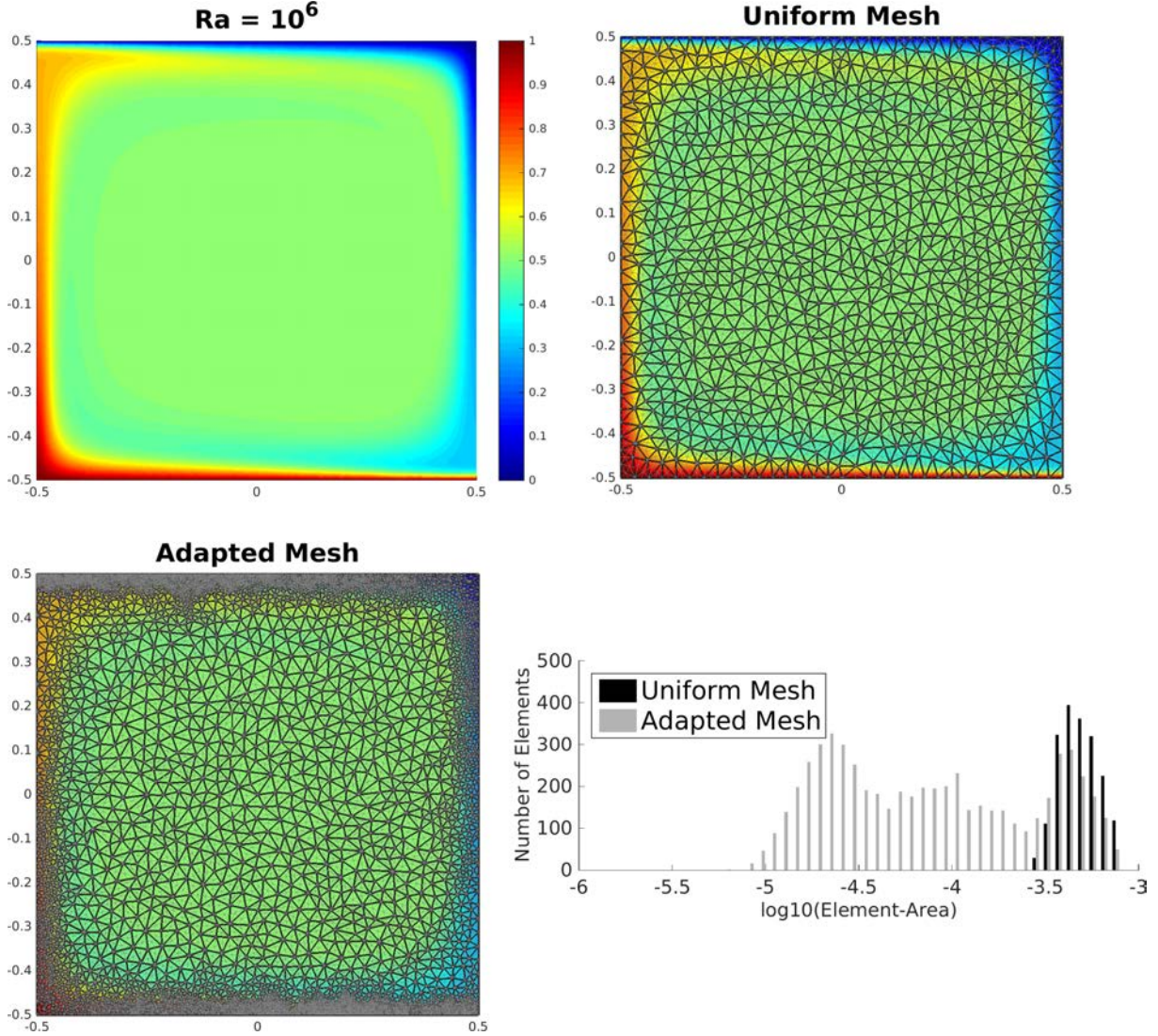


Figure 4.20: Top left: Thermal field at dynamic steady-state for the isoviscous convection benchmark case at $Ra = 10^6$ (case 1(C) in Blankenbach et al. (1989)). Top center: Example of a uniform unstructured mesh. Edges of mechanical elements are delineated with thicker black lines, while those of thermal mesh with thinner gray lines. The thermal mesh elements are generated by splitting each mechanical element into six triangles. Top right: Example of a mesh that is adapted to have smaller elements in regions of high thermal gradients. Bottom: Element-size distribution for the uniform and adapted meshes presented in the top row, as indicated by the legend.

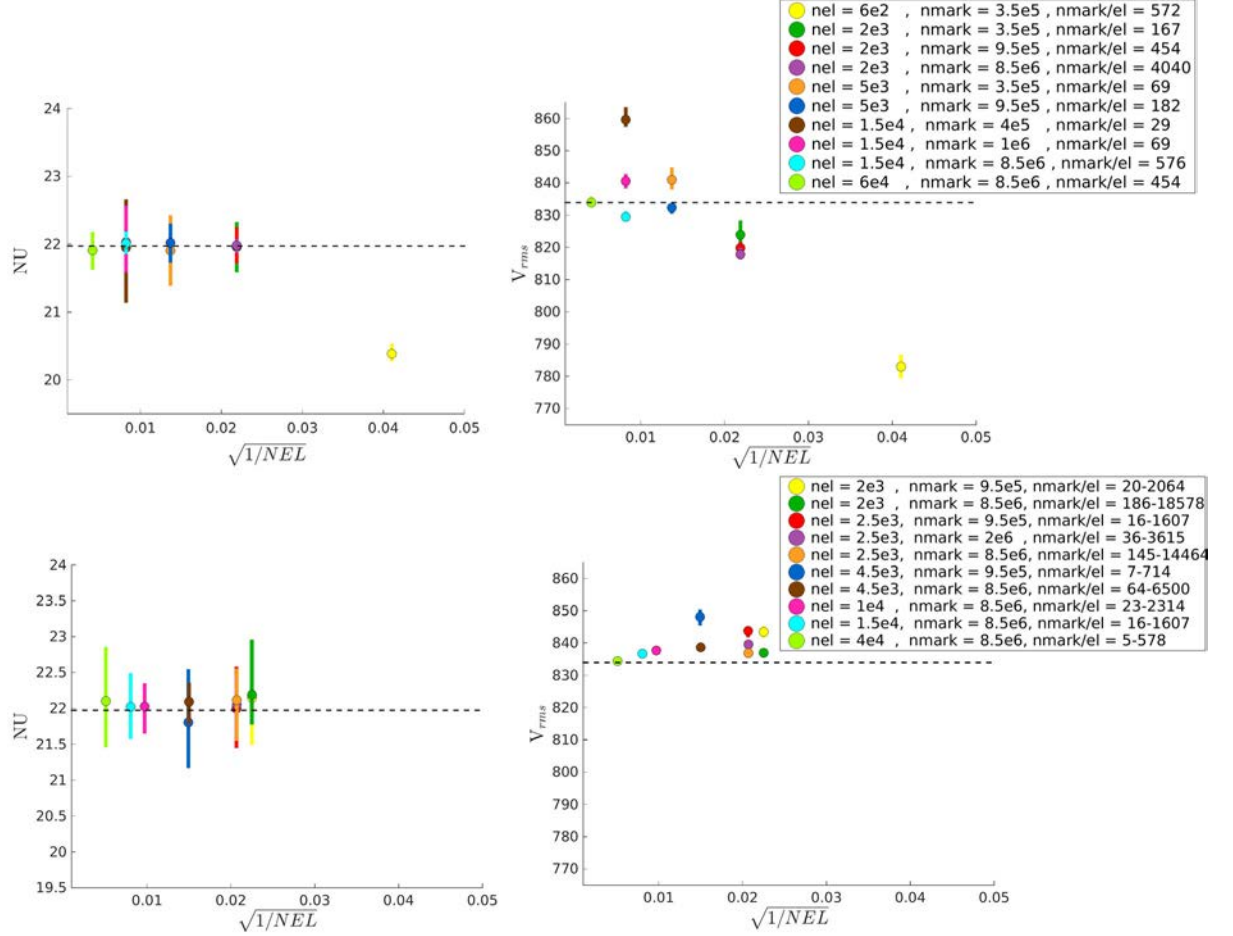


Figure 4.21: Results from the isoviscous convection benchmark case at $Ra = 10^6$ (case 1(C) in Blankenbach et al. (1989)) for uniform meshes (top row) and meshes adapted to have smaller elements in regions of high thermal gradients (bottom row). Results for varying number of elements ('NEL' on the x-axis and in the legend indicates the number of mechanical elements) and markers are shown, as indicated in the legends. The number of markers per element (indicated by 'nmark/el' in the legends) is approximate, because the element-areas vary somewhat in the uniform unstructured meshes, and vary by up to two orders of magnitude in the adaptive meshes. For the adaptive meshes, the approximate range of the number of markers per element is given in the respective legend. Circles indicate the mean value of the computed benchmark-quantities after the system has reached dynamic steady state. Thick lines indicate the range of oscillation around the mean-values. Dashed black lines are the benchmark values from Blankenbach et al. (1989).

4.4.3 Thermochemical Convection Benchmark

We simulate thermochemical convection of an isoviscous fluid, where the flow is driven by the compositionally and thermally induced density variations. The set up of this benchmark is described in *Van Keken et al. (1997)*, and mathematically described by Equations 3.6 - 3.9. Advection of thermal and compositional fields is performed using markers-in-cell methodology. Projection of compositionally and thermally induced density variations from markers to the integration points of the mechanical elements, as well as to the nodes of the thermal elements, is done using ghost-mesh method (1), described above. All simulations are performed using a small enough timestep ($\Delta t = 5 \cdot 10^{-6}$), such that increasing the time resolution (i.e. decreasing the timestep) does not change the simulation result.

Quantities that are calculated for benchmarking are the same as for the Rayleigh-Taylor instability problem, described in Section 4.4.1. We compute the benchmark case using both uniform meshes, and meshes that are adapted to have smaller elements in regions of high thermal gradients. In both cases, thermal mesh elements are generated by splitting each mechanical element into six triangles. We vary the total number of elements, as well as the number of markers.

For illustration, two snapshots of the thermal and compositional fields are shown in Figure 4.22, together with an example of a mesh that is adapted to have smaller elements in regions of high thermal gradients. Results of the time-evolution of the benchmark-quantities are shown in Figure 4.23.

Results obtained at different resolutions exhibit an increasing divergence with time, but generally agree with the published benchmark-values within the time-span $t \sim [0, 0.025]$ (which is also the time-span of approximate agreement of the results published in *Van Keken et al. (1997)*). Increasing mesh- and marker-resolution decreases the entrainment rate of high density material by thermal plumes. Similarly, *Van Keken et al. (1997)* observed that the more accurate high-order finite element method produced lower entrainment rate than the lower order finite difference method. Our results suggest that up to 100 markers per element are required to model accurate entrainment rates in this set-up (at least within the time-span $t \sim [0, 0.025]$), with lower resolutions overestimating the rate of entrainment.

The divergence of results with time even in this relatively simple isoviscous benchmark case, as well as the discrepancies in the modelled entrainment rate, have important implications for the interpretation of results obtained with long-term thermochemical convection simulations. In such simulations, processes taking place on small scales (e.g. viscous entrainment of compositionally dense material by plumes, or segregation of thin basaltic crust at the CMB) ultimately affect the emerging large-scale structures (e.g. accumulation and/or destruction of thermochemical piles at the CMB), and the

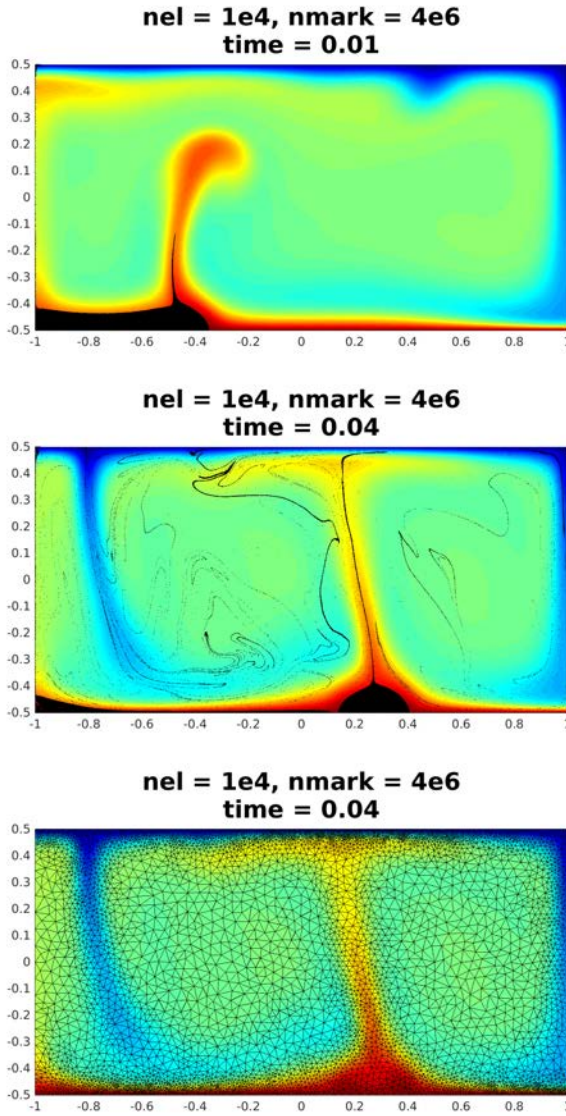


Figure 4.22: Snapshots of the thermal and compositional fields (dense material indicated by black markers) in the thermochemical convection benchmark. Bottom plot shows the mechanical mesh that is adapted to have smaller elements in regions of high thermal gradients.

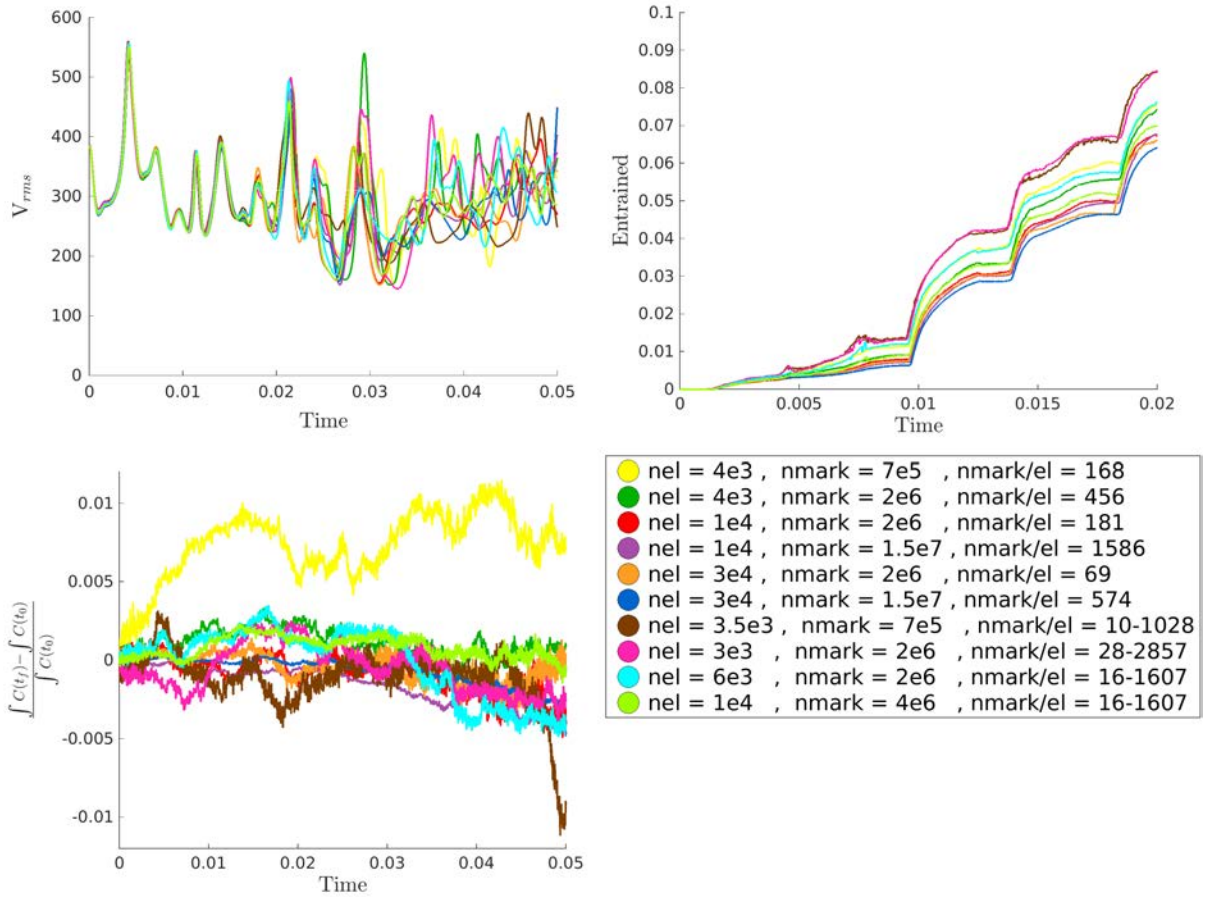


Figure 4.23: Benchmark quantities for the thermochemical convection benchmark, computed using the tracer-ratio method for advecting composition, and the characteristics based marker-in-cell method for advecting temperature (thermal and compositional fields are carried by the same markers). Results obtained with uniform meshes (entries of the legend that have a single value for the number of markers per element ‘nmark/el’) and meshes adapted to have smaller elements in regions of high thermal gradients (entries of the legend that have a range of values for the number of markers per element ‘nmark/el’) are shown.

global-scale model characteristics (e.g. heat-flow across the CMB or at the surface). Resolution tests, in which results of the large scale model-characteristics obtained at different mesh- and marker-resolutions are compared, help to gain confidence in the results of the simulations.

Chapter 5

Rheological Model

In this chapter, we present the rheological model of the mantle that was used in our mantle convection simulations. Values of the physical parameters entering the rheological model are presented, together with the approximations that were made to simplify the rheological law. Implementation of the model in our code is presented at the end of the chapter.

5.1 Factorization of Temperature- and Depth-Dependence of Viscosity

The rheological model used in this study includes depth- and temperature-dependence of viscosity, and largely follows the one derived in *Steinberger and Calderwood* (2006). The rheological behavior of the mantle may generally be expressed as that of power-law fluids:

$$\dot{\epsilon} = A_1 \sigma^n \exp\left(-\frac{H}{RT}\right) \quad (5.1)$$

where $\dot{\epsilon}$ and σ are the square root of second invariants of strain rate and deviatoric stress tensors, respectively, A_1 is a constant, H is enthalpy, R is the gas constant, T is temperature, and n the stress exponent that determines the stress and strain-rate dependence. The apparent viscosity can followingly be defined as:

$$\eta \equiv \frac{\sigma}{2\dot{\epsilon}}$$

The rheological model of *Steinberger and Calderwood* (2006) does not explicitly include dependence on strain-rate. However, in regions of the mantle where it is important (i.e. in the upper mantle), non-Newtonian behavior can be accounted for by

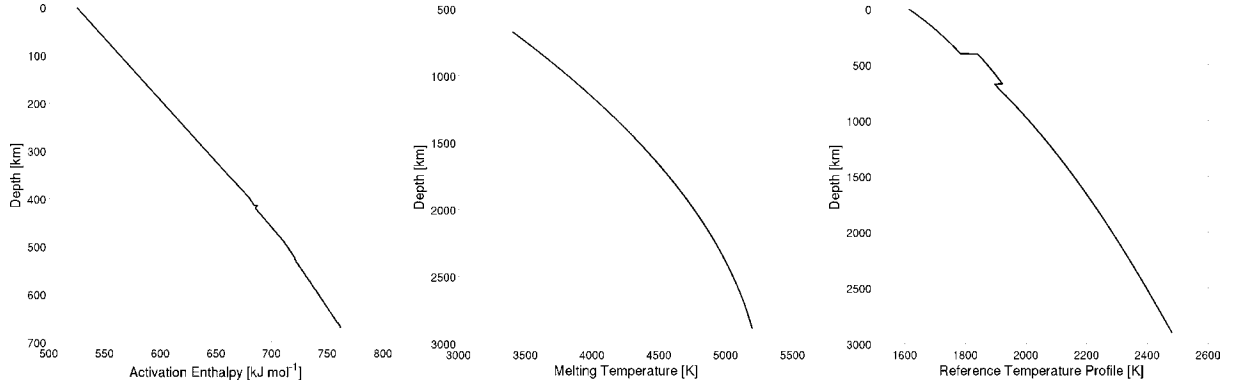


Figure 5.1: From left to right: depth-profiles of activation enthalpy (used to evaluate viscosity in the upper mantle), melting temperature (used to evaluate viscosity in the lower mantle), and adiabatic temperature.

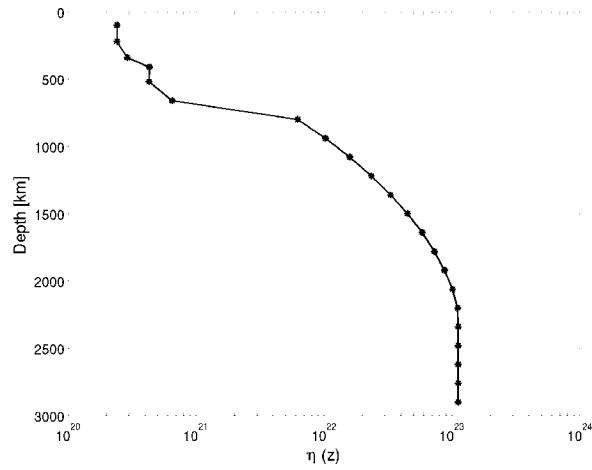


Figure 5.2: Optimized radial viscosity profile, modified from Steinberger and Calderwood (2006) to exclude the effect of thermal boundary layers.

taking advantage of the results presented in *Christensen* (1983). *Christensen* (1983) found similarity between convective flow of power-law fluids and those of Newtonian fluids, with a reduced activation enthalpy of the latter by a factor of 0.3–0.5. Observing that the lower limit of this reduction factor is close to the value of $1/n$ for $n = 3$ (which is the stress exponent appropriate for fluid deforming by dislocation creep (e.g. *Karato*, 2008), as is expected for the upper mantle), *Steinberger and Calderwood* (2006) adopt the following expression for the apparent viscosity:

$$\eta = A \cdot \exp\left(\frac{H}{nRT}\right) \quad (5.2)$$

where strain-rate is assumed to be constant, and A is a constant. The values of n are $n = 3.5$ above 660km depth (i.e. in the upper mantle), and $n = 1$ below 660km depth (i.e. lower mantle).

The dependence on H in Equation 5.2 can be replaced by the dependence on melting temperature, T_m . Experimental studies show a good correlation between activation enthalpy and melting temperature (e.g. *Weertman*, 1970), expressed as:

$$H = BRT_m \quad (5.3)$$

where B is a dimensionless constant. This leads to an alternative expression of viscosity:

$$\eta = A \cdot \exp\left(\frac{BT_m}{nT}\right). \quad (5.4)$$

Yamazaki and Karato (2001) estimate the value of B for the two main mantle materials, (Mg,Fe)SiO₃ perovskite and (Mg,Fe)O magnesiowustite, to be ~ 10 and ~ 14 , respectively. *Steinberger and Calderwood* (2006) use an arithmetic mean of these two values, namely $B = 12$, which we adopt as well. Depth-profiles of activation enthalpy and melting temperature used in this study are presented in Figure 5.1.

Following *Steinberger and Calderwood* (2006), we use activation enthalpy profile, based on *Calderwood* (1999), to determine the viscosity in the upper mantle (top 660 km), and melting temperature profile, based on the results of mineral physics experiments (e.g. *Wang*, 1999; *Zerr and Boehler*, 1994) for the viscosity in the lower mantle. The choice of whether to use enthalpy or melting temperature for the viscosity profile is made based on the availability of the experimental data.

Temperature is decomposed into a reference state temperature, \bar{T} , which is the lateral average of T and only depends on depth, and a departure from this reference state, δT , such that:

$$\frac{1}{T} = \frac{1}{\bar{T} + \delta T} = \frac{1}{\bar{T}} - \frac{\delta T}{\bar{T}(\bar{T} + \delta T)} \quad (5.5)$$

Using the above decomposition of temperature, we can factorize dependence of viscosity on temperature and depth in terms of its radial and lateral variations, which

can be expressed as following:

$$\eta = \eta_i \cdot V_{rT}(z) \cdot V_{lT} \quad (5.6)$$

where η_i are the ‘anchor viscosities’ that were determined in *Steinberger and Calderwood* (2006) for 3-4 depth-ranges of the mantle, by minimizing misfit between model predictions and observations, $V_{rT}(z)$ is the radial viscosity variation due to radial temperature and pressure variations, and V_{lT} is the lateral viscosity variation due to lateral temperature variations. Using the Equations 5.2, 5.4 and 5.5, we can express viscosity as:

$$\eta = \eta_i \cdot \exp \left[\left(1 - \frac{\delta T}{\bar{T} + \delta T} \right) \frac{H}{nR\bar{T}} \right] = \eta_i \cdot \exp \left[\left(1 - \frac{\delta T}{\bar{T} + \delta T} \right) \frac{BT_m}{n\bar{T}} \right] \quad (5.7)$$

In order to use this model, we need to specify the reference temperature \bar{T} , the detailed derivation of which is presented in Section 5.2,

5.2 Radial Temperature Profile

We distinguish between the reference temperature profile \bar{T} that is used for evaluating viscosity according to Equation 5.7, and the one that is otherwise used in our model of the mantle, i.e. Equations 3.6 and 3.8. The reference thermal profile used for conservation equations is simply a constant, since we use the Boussinesq approximation. For Equation 5.7, we use a reference profile $\bar{T}(z)$ that is adiabatic throughout the entire mantle depth, which is a deviation from *Steinberger and Calderwood* (2006), who include the thermal boundary layers into their reference profile. We exclude the thermal boundary layers from $\bar{T}(z)$, and instead treat them in the same manner as the lateral temperature variations, as will be discussed later.

The adiabatic temperature gradient in the mantle is given by (e.g. *Schubert et al.*, 2001):

$$\frac{d\bar{T}}{dz} = \frac{\alpha(z)\bar{T}(z)\gamma(z)}{C_p(z)} \quad (5.8)$$

where α is thermal expansivity, γ is the gravitational acceleration, and C_p is specific heat capacity. The adiabatic temperature profile is obtained upon integration of Equation 5.8. In order to do this, the radial profiles of α , γ and C_p must be determined.

To obtain a unique adiabatic profile, we need to prescribe a value at some given depth. Surface value of $T_{adi,0} = 1613$ K at $z = 0$ is used, which is an extrapolated value of the mantle adiabat to the surface, based on decompression melt studies of MORBs.

The gravity profile γ is determined from the radial profile of density, and is well constrained from previous studies. *Schubert et al.* (2001) demonstrate how the gravity can be computed for a spherically averaged model of the Earth, using the results from seismic studies.

A constant value for the specific heat capacity $C_p \approx 1250 \text{ J kg}^{-1} \text{ K}^{-1}$ is used. Thermal expansivity α in the upper mantle is given by *Schmeling et al.* (2003):

$$\begin{aligned}\alpha(p, T) &= \alpha_0(T) \left(\frac{\rho(p, T)}{\rho_0(T)} \right)^{-\delta_T} \\ \alpha_0(T) &= 3.034 \cdot 10^{-5} \text{K}^{-1} + 7.422 \cdot 10^{-9} \text{K}^{-2} \cdot T - 0.5381 \text{K} \cdot T^{-2}\end{aligned}\quad (5.9)$$

where subscript 0 denotes the value at zero-pressure, and $\delta_T = 5.5$. In the lower mantle, α is given by (*Steinberger and Calderwood, 2006*):

$$\begin{aligned}\alpha(p, T) &= \alpha_0(T) \exp \left\{ -\frac{\delta_{T0}}{b} \left[1 - \left(\frac{\rho_0(T)}{\rho(p, T)} \right)^b \right] \right\} \\ \alpha_0(T) &= \left(2.9 + \frac{0.9 \cdot T}{1000 \text{K}} \right) \cdot 10^{-5} \text{K}^{-1}\end{aligned}\quad (5.10)$$

where $\delta_{T0} \approx 5.5$ and $b \approx 1.4$. The density values that are present in the expression for α can be obtained from e.g. PREM. The difference in expressions for α for upper and lower mantle arises due to the relation between the thermal expansivity and density, which is assumed constant in the upper mantle, but varies with depth in the lower mantle.

To incorporate a realistic transition of the majorite phase between 660 and 730 km depth into the thermal expansivity profile, the following expression for α is used in this depth range:

$$\alpha(z) = \alpha_{lm}(z) + 0.3 \cdot (\alpha_{um}(z) - \alpha_{lm}(z)) \cdot (z - 730 \text{km}) / (660 \text{km} - 730 \text{km}) \quad (5.11)$$

where subscripts *um* and *lm* stand for *upper mantle* and *lower mantle*, respectively, and α_{um} and α_{lm} are determined using Equations 5.9 and 5.10, respectively.

The effect of the phase transitions at 400 and 660km depths on the reference temperature profile is accounted for by using the following expression for the temperature jumps across these phase boundaries:

$$\Delta T_L = \frac{Q_L}{C_p} = \frac{\Gamma \Delta \rho T_{pb}}{\rho_{pb}^2 C_p} \quad (5.12)$$

where Q_L is the latent heat release per unit mass, Γ is the Clapeyron slope, $\Delta \rho$ is the density jump across the phase boundary, T_{pb} and ρ_{pb} is the average temperature and density above and below the phase boundary, respectively. For the phase transition at 400km, $\Gamma \Delta \rho = 0.5 \cdot 10^3 \text{ MPa K}^{-1} \text{ kg m}^{-3}$ is used, and for 660km $\Gamma \Delta \rho = -0.3 \cdot 10^3 \text{ MPa K}^{-1} \text{ kg m}^{-3}$. For references, see *Steinberger and Calderwood* (2006). The resulting reference temperature profile \bar{T} is shown in Figure 5.1.

5.3 Implementing Depth- and Temperature-Dependence of Viscosity

The radial viscosity profile $\eta(z)$ that was derived using the parameters described above, and optimized such as to minimize the misfit between model predictions and observations is presented in Figure 5.2. The difference between the profile presented in Figure 5.2 and the ones published in *Steinberger and Calderwood* (2006) is that the former does not include the effect of thermal boundary layers on the viscosity. The radial viscosity profile presented in Figure 5.2 remains constant throughout the numerical simulation. The viscosity variations due to lateral temperature variations and thermal boundary layers are modeled as modifications of the radial viscosity profile, and are computed in the course of the simulation.

$$\begin{aligned} \eta &= \eta(z) \cdot \exp\left(-\frac{H}{nR\bar{T}} \frac{T - T_{off}}{(T - T_{off} + \frac{\bar{T}}{T_{scale}})}\right) \\ T_{scale} &= T_{CMB} - T_0 - \Delta\bar{T} \approx 2348K \\ T_{off} &= \frac{\bar{T}_0 - T_0}{T_{scale}} \approx 0.5658 \end{aligned} \quad (5.13)$$

where $\eta(z)$ is the reference viscosity profile at adiabatic temperature, H activation enthalpy, n stress exponent ($n = 3.5$ above 660km depth, and $n = 1$ below 660km depth), $\bar{T}(z)$ adiabatic reference temperature profile (note that $\bar{T}(z)$ is different from the reference temperature profile used in the linearization of the conservation equations, with the latter simply being a constant due to the Boussinesq approximation), T are the nondimensional temperature values computed in the course of the simulation, $T_{CMB} = 3500K$ and $T_0 = 285K$ are the assumed temperature values at the core-mantle boundary and at the surface, respectively, and $\Delta\bar{T} \approx 866 K$ is the adiabatic temperature increase across the depth of the mantle. The offset temperature T_{off} and the scaling temperature T_{scale} are used in order to correct for the fact that different reference temperature profiles are used in the general (Boussinesq) model, according to which T is computed, and in the viscosity model, where \bar{T} and δT are used. We use cut-off values 10^{19} and 10^{24} Pa s - to restrict viscosity variations to the respective range.

Chapter 6

Replenishment and Destruction of Compositional Anomaly In Thermochemical Mantle Convection: Simulation Results

In this chapter, we present the results of thermochemical convection simulations that illustrate the dynamics and thermal and compositional evolution of large-scale compositional heterogeneities at the CMB, which develop self-consistently by segregation and accumulation of subducted oceanic crust. This is followed by a discussion about the main observations that were made from these results, and inferences that can be made for the structures evolving in the Earth’s deep mantle. For a critical assessment of the latter, we also discuss the limitations of our models. Finally, the conclusions and outlook for the presented work conclude this chapter and thesis. Part of the work presented in this chapter have been published in *Mulyukova et al. (2015)*.

6.1 Model Description

Geometry of the domain used in the simulations is a two-dimensional hollow cylinder. The nondimensional inner and outer radii are set to 1 and 2, respectively. It is an intermediate scaling compared to the ones studied in *van Keken (2001)*. See Section 6.4.2 for the discussion on how this choice of geometry affects our results, and how it compares to geometries used in other numerical studies. Mechanical boundary conditions used in our models are free slip at the inner boundary of the cylinder,

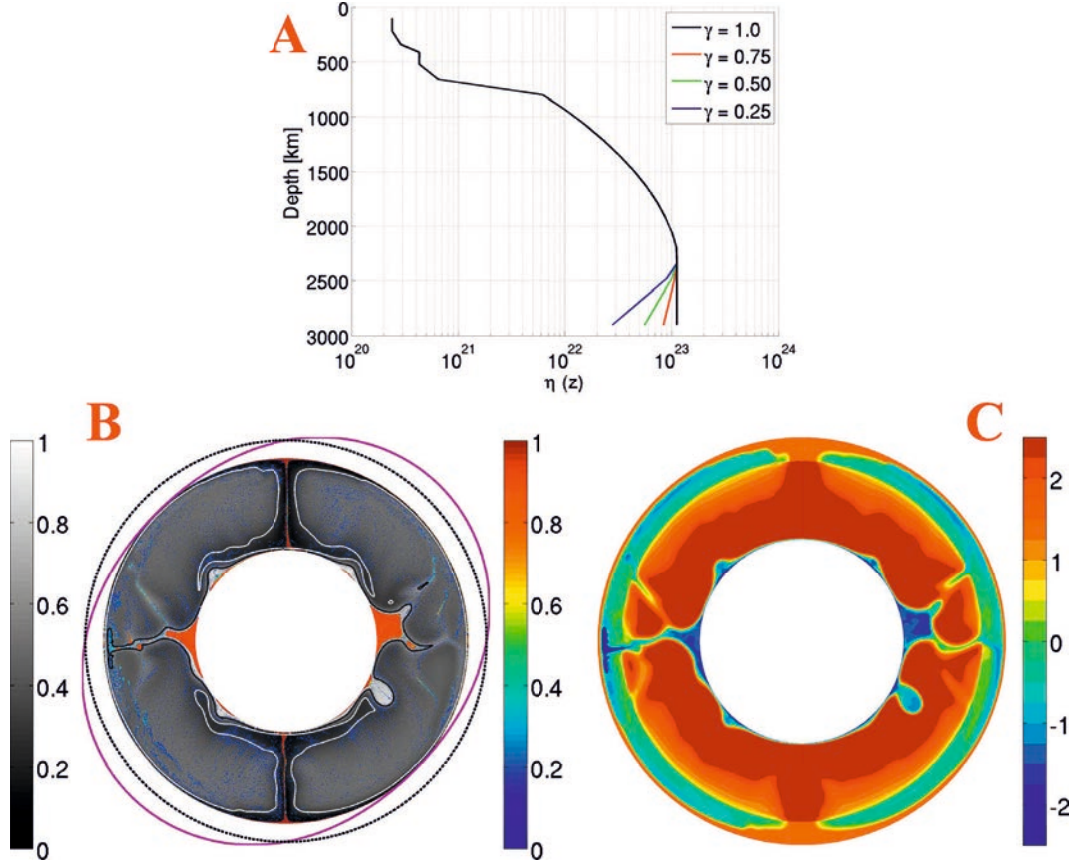


Figure 6.1: (A): Optimized radial viscosity profile, modified from Steinberger and Calderwood (2006) to exclude the effect of thermal boundary layers. The colored lines indicate the effect on viscosity of different values of γ - a variable that we use to lower the viscosity in the bottommost 500 km of the domain, according to legend (see Section 6.2 for details). (B): Snapshot from one of the simulations to explain the set-up of numerical experiments. The gray-scale color-field represents the nondimensional thermal field (colorbar on the left). Red-blue colorscale represents the fraction of OC material (colorbar in the center). Regions where OC-fraction is less than 0.1 are made transparent. The black and white lines are hot ($T = 0.6$) and cold ($T = 0.3$) isotherms, respectively. The purple line on the exterior illustrates the direction of the tangential component of the imposed surface-velocity V'_s (negative means clockwise) - black dashed line indicates the zero-value. V'_s is a function of azimuthal position θ : $V'_s = A_{V_s} \sin(2\theta)$, where $A_{V_s} = 1$ cm/yr. (C): Same snapshot as in (B), but showing base ten logarithm of nondimensional viscosity (colorbar on the right).

and prescribed velocities at the outer boundary. The tangential component of the prescribed surface velocity V'_s is a sinusoidal function of azimuthal position θ along the outer boundary: $V'_s = A_{V_s} \sin(2\theta)$, with the amplitude $A_{V_s} = 1$ cm/yr. The schematic of the prescribed velocity boundary condition is given in Figure 6.1. The prescribed surface-velocity in our models is somewhat lower than what is representative for the tectonic plate velocities. This is because the role of the prescribed surface velocity in our model is mainly to organize the flow such as to form two downwelling regions. As was shown in the analogue experiments of *Gonnermann et al.* (2004), increasing the magnitude of the surface velocity suppresses the naturally developing convecting pattern, which we try to avoid in our models. See Section 6.4.3 for the discussion about the effects of prescribed velocity on our modelling results.

Thermal boundary conditions constitute prescribed temperatures at both inner ($T = 1$) and outer ($T = 0$) boundaries. For initial temperature conditions, we use results of a convection model with the same geometry as in our tested models, but at a coarser resolution, without any compositional heterogeneities, and which was simulated for 500 Myr (starting with $T = 0$ at the surface, $T = 1$ at the CMB, and $T = 0.5$ everywhere else). The initial temperature field used for the models is such that the surface heat flow is larger than the bottom heat flow, and thus the system starts off with mantle-cooling. Over the last Gyr of simulation time, our results show mantle cooling at a rate of 10.5 – 14.5 TW for different tested cases, which is partially due to their initial thermal conditions, and partially due to their developing dense basal structures.

The compositional anomaly is continuously generated throughout the simulation: material that enters the top 6 km of the domain gets converted to oceanic crust material, which is intrinsically denser than the ambient material.

The rheological model used in the simulations was presented in Chapter 5, and the numerical methodology in Chapter 4.

6.2 Results

We systematically vary two physical parameters that have been found to play a dominant role in the evolution of compositional anomaly in a vigorously convecting mantle: buoyancy ratio (Equation 3.11) and viscosity. In our models, viscosity is varied only in the lowermost 500 km of the mantle. We don't attribute its variation to any specific mechanism. Rather, we treat it as an uncertainty in the lowermost part of the radial viscosity profile, shown by the black line in Figure 6.1, which is varied for different models to investigate the effect of this uncertainty.

We define a parameter $\gamma = \frac{\mu_{red}}{\mu_{orig}}$, where μ_{orig} is the reference value of the radial viscosity profile at CMB, shown by the black line in Figure 6.1, and μ_{red} is a reduced

value of the radial viscosity profile at CMB, shown as colored lines in Figure 6.1. Radial viscosity profile between the CMB and 500 km above it is modified to ensure a smooth viscosity reduction towards the bottom, as demonstrated by colored lines in Figure 6.1. Radial viscosity profile above 500 km from the CMB is identical for all models. The range of viscosity reductions tested in this study is given by $0.25 < \gamma < 1.0$.

We use capital letters B-F to enumerate different Br -values (B, C, D, E, F correspond to $Br = 0.57, 0.71, 0.85, 0.99, 1.1$, which scale to $\Delta\rho'_C = 100, 125, 150, 175, 200$ kg/m³, or, equivalently, a density contrast of 1.8, 2.3, 2.7, 3.2, 3.6%). Different γ -values are indicated by numbers from 1 to 4 (1, 2, 3, 4 correspond to $\gamma = 1.0, 0.75, 0.50, 0.25$). For example, a model with $Br = 0.57$ and $\gamma = 0.50$ is entitled **B3**.

Figure 6.2 shows snapshots of the thermochemical evolution for four different cases: **C1**, **C3**, **F1**, and **F4**. In all of these cases, large scale compositional anomaly is formed at the CMB. A zoomed-in view on piles that have developed by the end of each simulation (at 3 Gyr) are shown in Figures 6.3 and 6.4, for the piles on the left and right sides of the domain, respectively. The shapes of large-scale anomalies in the presented cases can be grouped into two categories: (i) large topography piles with sharp edges, which are highly mobile both laterally and vertically, have a close to homogeneous distribution of dense material in their interior, and have plumes rising from their surface and edges, occasionally entraining large bulks of the pile-material; (ii) high density basal layer covering nearly the entire CMB, overlain by high topography piles with a much lower fraction of OC material, and plumes rising from their interior and edges, entraining thin filaments of pile material. Scenario (i) is typical for the cases with moderate buoyancy ratio ($Br < 0.8$), while scenario (ii) is typical for the high buoyancy ratios ($Br > 0.8$). The effect of lowering viscosity in the bottom 500 km appears to be to reduce the concentration of dense material in the piles.

6.2.1 Global Scale Time Evolution

We first look at the thermal evolution of the different cases. Figure 6.5 shows time evolution of heat flow, measured at upper and lower boundaries of the model, for six different cases (**B1**, **B4**, **D1**, **D4**, **F1**, and **F4**). To arrive at dimensional heat flow values indicated on the left axis of Figure 6.5, we first dimensionalised the values of circumference-averaged conductive radial heat flux, measured at top and bottom boundaries of our models, and integrated these over the Earth-like spherical surface- and CMB-area, respectively. The right axis of Figure 6.5 shows the respective values of the Nusselt number - the non-dimensional radial conductive heat flux at the surface of the cylindrical (2D) model.

Using the results of Figure 6.5, we can see the effect of buoyancy ratio and viscosity

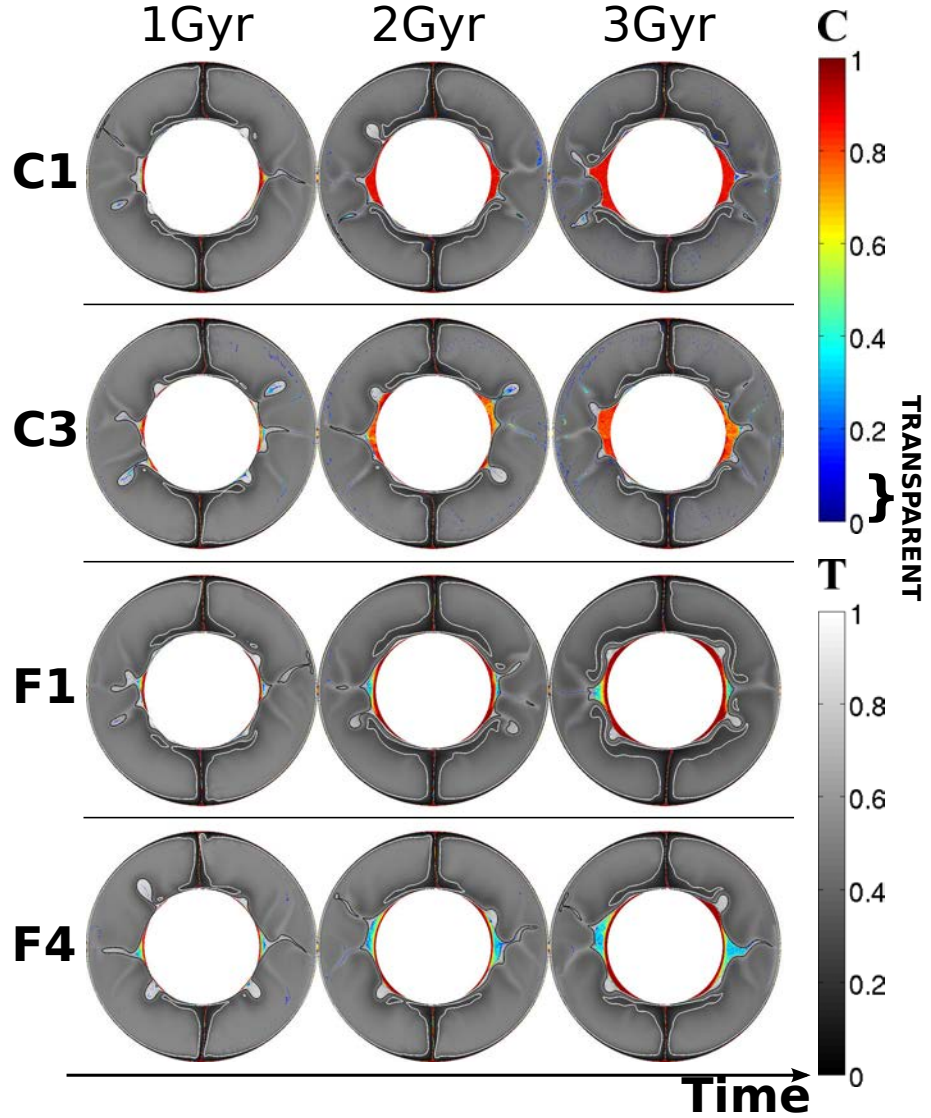


Figure 6.2: Snapshots of the thermochemical evolution at three points in time (1, 2, and 3 Gyr) for four different cases (from top to bottom): C1 ($Br = 0.71$, $\gamma = 1.0$), C3 ($Br = 0.71$, $\gamma = 0.50$), F1 ($Br = 1.1$, $\gamma = 1.0$), and F4 ($Br = 1.1$, $\gamma = 0.25$), as indicated on the left of the figure. The gray-scale reflects the thermal field (bottom colorbar), and the red-blue scale reflects the concentration of oceanic crust material (top colorbar). Concentrations of OC material lower than 0.1 are made transparent. The black and white lines are hot ($T^* = 0.6$) and cold ($T^* = 0.3$) isotherms, respectively (T^* is the nondimensional temperature).

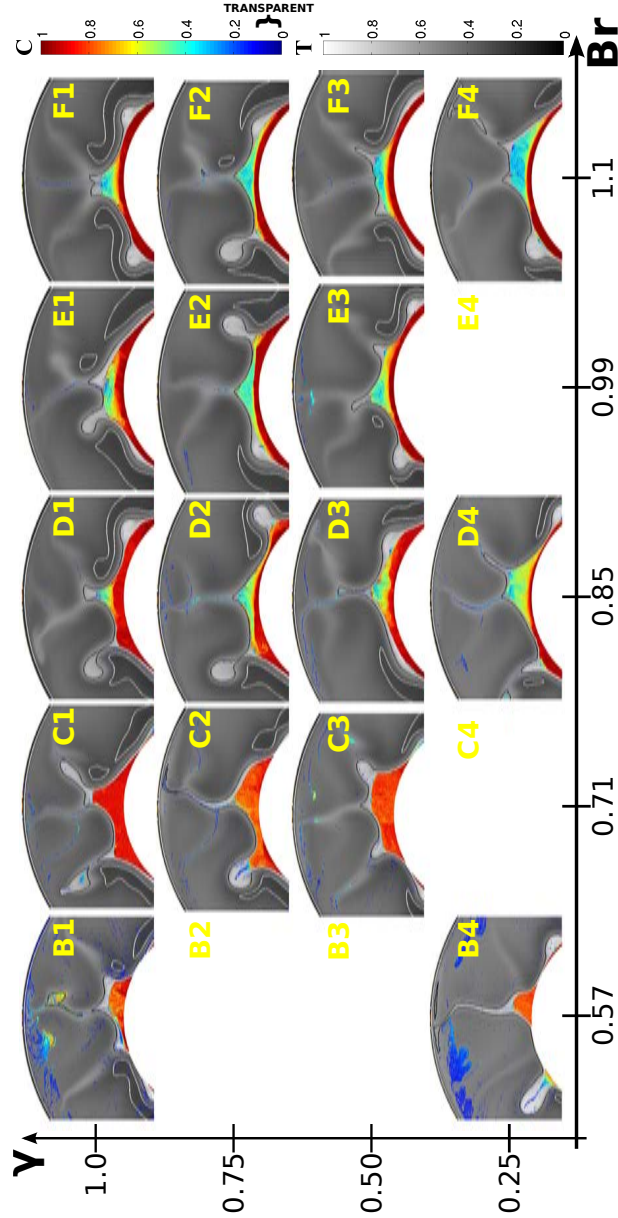


Figure 6.3: Snapshots at 3 Gyr for all studied cases, zoomed in on the thermochemical pile that develops on the left side of the domain. The gray-scale reflects the thermal field (bottom colorbar), and the red-blue scale reflects the concentration of oceanic crust material (top colorbar). Concentrations of OC material lower than 0.1 are made transparent. The black and white lines are hot ($T^* = 0.6$) and cold ($T^* = 0.3$) isotherms, respectively (T^* is the nondimensional temperature).

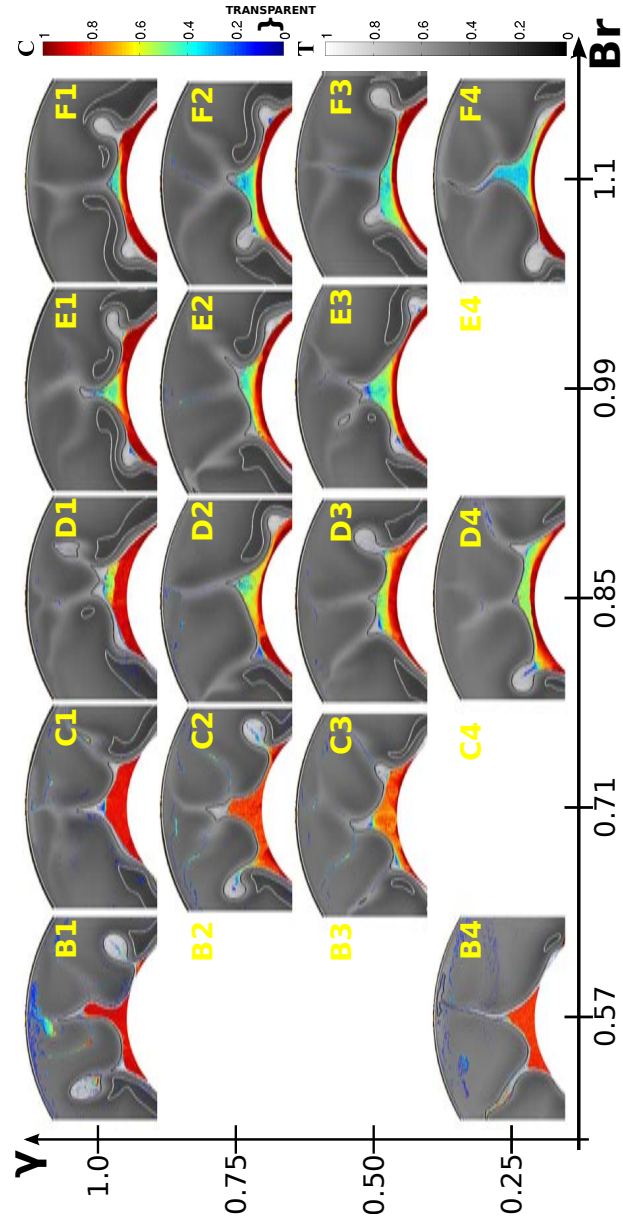


Figure 6.4: Same as Figure 6.3, but zoomed in on the thermochemical pile that develops on the right side of the domain.

reduction in the bottom 500 km on our models thermal evolution. Nu in the beginning of the simulations (up to 1 Gyr - before any substantial amount of dense material has been accumulated at the bottom) is very similar for cases with the same values of viscosity: lowering the viscosity in the bottom 500 km leads to higher heat flux at the surface, consistent with the fact that a lower viscosity gives a higher effective Rayleigh number - thus a higher vigor of convection and more efficient heat flux. After approximately 1 Gyr, the effect of the accumulated dense material at the base becomes evident: cases with the higher buoyancy ratio, and thus a larger volume of dense material accumulating on top of the CMB (as will be discussed in Figure 6.6), have a lower Nu , compared to cases with lower Br . Highest Nu (from ~ 1.5 Gyr until the end of the simulation) among the presented models is obtained for the case with the lowest buoyancy ratio and lowered viscosity in the bottom 500 km (**B4**: $Br = 0.57$, $\gamma = 0.25$), and the lowest Nu is obtained for the case with the highest buoyancy ratio and original (i.e. not reduced in the bottom 500 km) viscosity profile (**F1**: $Br = 1.1$, $\gamma = 1$).

While heat flow across the CMB appears to reach a steady state for all of the presented cases, according to Figure 6.5, there is a gentle decline in the heat flow at the surface. This, and the observation that the heat flow at the surface is larger than that at the CMB throughout the simulation, indicates that the system is still not in statistical steady state. Over the last Gyr of simulation time, the mantle is cooling at a rate of 10.5 – 14.5 TW for different models, which is partially due to their initial thermal conditions, and partially due to their developing dense basal structures, which influences the heat flowing across the CMB.

Presence of a large scale compositionally dense anomaly at the CMB reduces the amount of heat that is flowing into the system. Comparing the amount of dense material (in terms of mean OC-concentration in the bottom 100 km) that accumulates at the base for each of the six cases presented in Figure 6.6(A), and the amount by which the mean temperature at mid-depth has lowered from its initial state, shows that a larger amount of high density material at the CMB leads to a cooler system. A cooler mid-mantle is also more viscous, due to the temperature-dependence of viscosity. Thus, cases with more dense material at the base are more viscous and have a lower effective Rayleigh number. Figure 6.6(A) also shows that more dense material accumulates at the base for higher values of Br , meaning that increasing Br leads to a cooler and more viscous mantle. Effect of decreasing viscosity in the bottom 500 km on the amount of dense material that gets accumulated at the base is less pronounced. It appears that for cases with $Br < 0.8$, decreasing γ reduces the amount of material that gets accumulated, while for cases with $Br > 0.8$, decreasing γ slightly enhances accumulation.

Figure 6.6(B) shows the volume fraction of the dense oceanic crust material present in the system for the six cases over time. The downwelling flow in our models, and thus

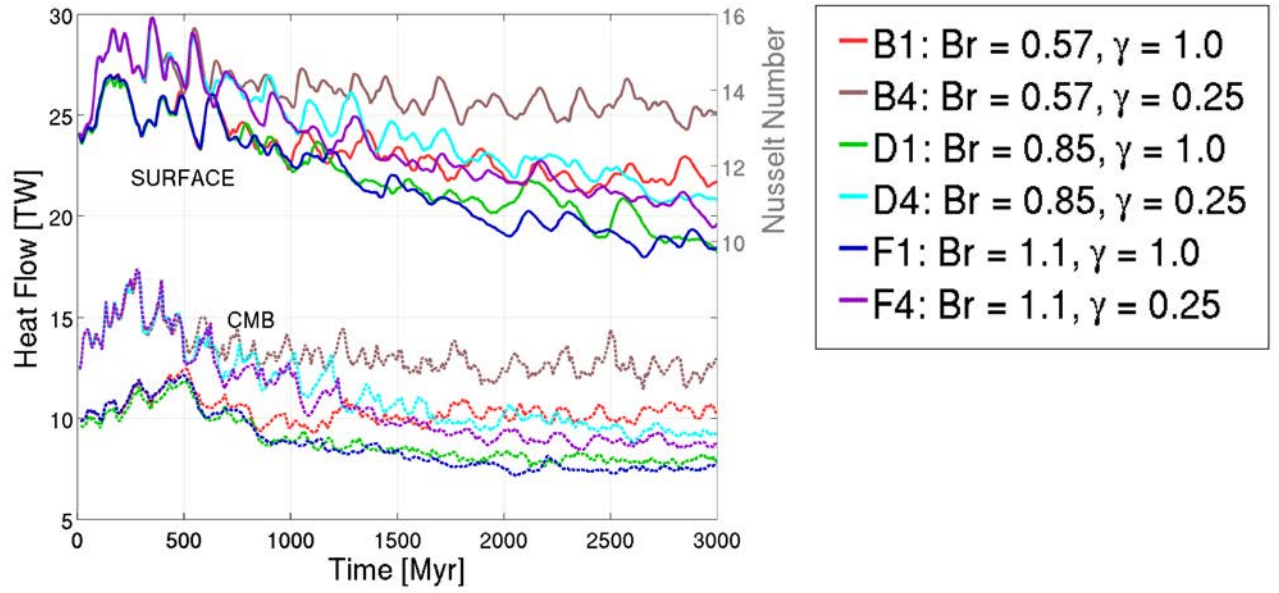


Figure 6.5: Time evolution of conductive radial heat flow across the surface (solid lines) and the CMB (dashed lines). Dimensional values (in TW) are indicated on the left axis, and were obtained by first dimensionalising the values of circumference-averaged conductive radial heat flux, measured at top and bottom boundaries of the models, and then integrating these values over the spherical surface-area of the Earth and CMB, respectively. Right axis indicates the respective values of the Nusselt number (only shown for the surface heat flux).

exposure of new surface area where oceanic crust can form, is largely determined by the prescribed surface velocities, and is therefore similar for all of the models. According to the current rate of production of MORB, as well as that of the recent past, *Xie and Tackley* (2004) estimate that the oceanic crust constitutes approximately 10% of the mantle volume today. This is a double value of what is produced in our models by the end of the simulations, meaning that our modeled rate of replenishment of the high density OC material is lower compared to a more Earth-like system.

Non-uniform distribution of high-density material within the large-scale compositional anomaly, seen in Figures 6.3 and 6.4, is indicative of small scale convection taking place in the lowermost part of the domain, and/or within the thermochemical piles or layers. Using Fourier transform of the radial velocity component, we can get an idea of how the convective flow is partitioned between the small-scale flow, and the larger scale flow, with the latter dominated by plumes and downwellings. Figure 6.7 presents the results of this analysis for six different cases (**B1**, **B4**, **D1**, **D4**, **F1**, and **F4**), computed at two different depths: 250 km above the CMB, and at mid-depth of the domain. Small-scale convection is reflected in the higher harmonic degrees. Partitioning of the radial velocity component between different harmonic degrees for the cases with lower Br values (**B1** and **B4**) changes little between the two depths - inferring a minor role of the small scale convection in these cases. On the contrary, results for cases with high Br values (**D1**, **D4**, **F1** and **F4**) demonstrate a notable shift in the radial velocity partitioning between different harmonic degrees from the lower to higher depths: at 250 km above the CMB the small scale convection constitutes a much larger part of the flow, compared to mid-depth. Effect of lowered viscosity in the bottom 500 km of the domain is reflected in a slight increase of power stored in the high harmonic degrees. It is an expected result, given that lower viscosity results in higher Rayleigh number, which further results in smaller characteristic length-scales of convection (e.g. *Schubert et al.*, 2001).

Upwelling flow of the rising hot plumes can entrain the high density OC material in its vicinity, and gradually contribute to the destruction/erosion of the accumulated dense anomaly at the CMB. This can happen solely by the action of viscous drag, in which case only a thin filament of high density material is entrained. This is observed in cases with $Br > 0.8$ (Figures 6.3 and 6.4). Entrainment can be assisted by the action of mechanical mixing of high density and ambient materials prior to rising in plumes: a sufficiently diluted mixture can be heated to the degree where its effective compositionally induced positive density anomaly is less strong than the thermally induced negative density anomaly, forming the so-called thermochemical plumes. The latter is observed in cases with $Br < 0.8$ (Figures 6.3 and 6.4), and is much more efficient at destroying the compositional anomaly at the base of the mantle - i.e. it causes a higher flux of high density material from the bottom to the surface of the mantle. Efficiency of these two entrainment-modes to transport high

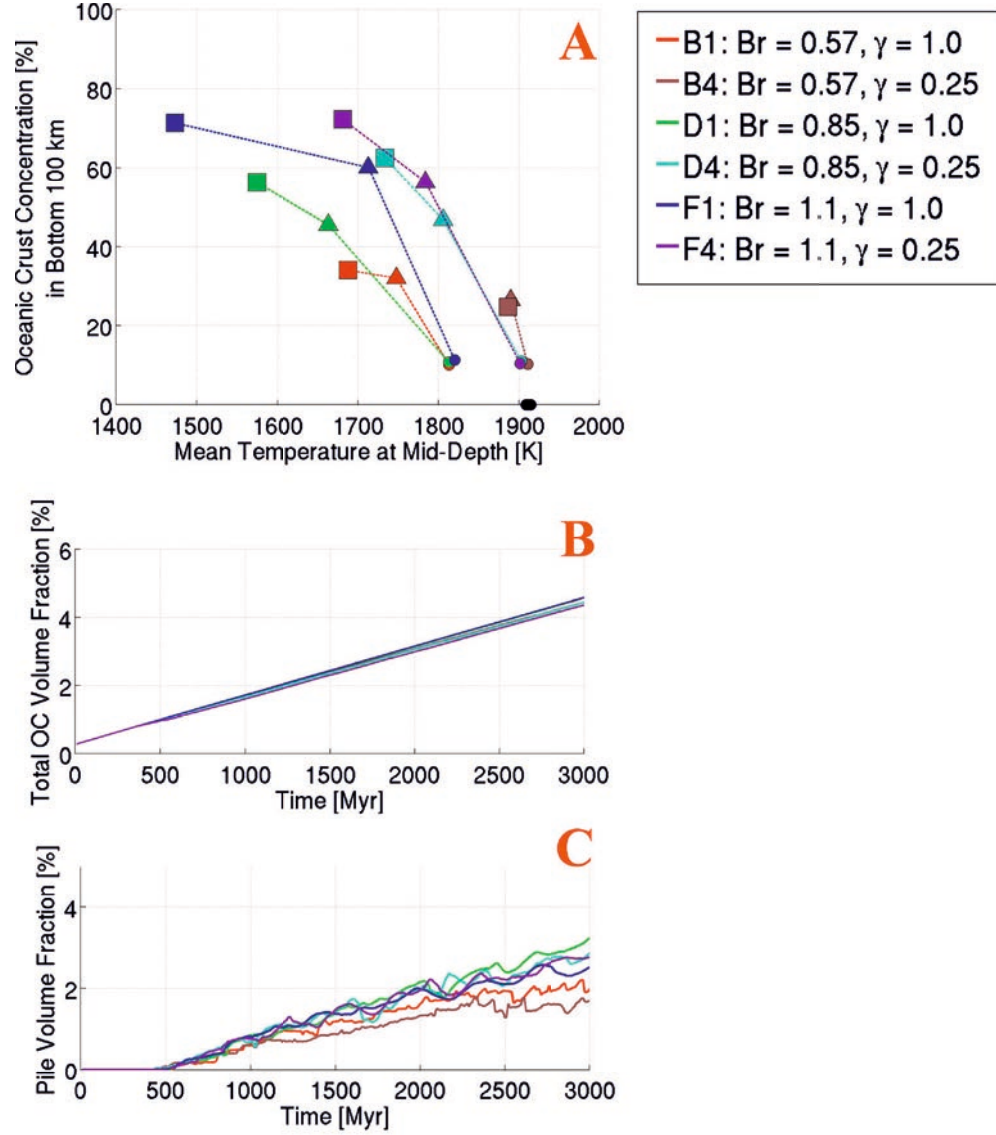


Figure 6.6: (A): Mean temperature at mid-depth versus mean concentration of OC material in the bottom 100 km of the domain. Results for six cases are presented, according to legend. Colored symbols indicate points in time at which the plotted values were sampled: circles - 0.5 Gyr, triangles - 2 Gyr, squares - 3 Gyr. The black filled circles are the values sampled after the first 10 Myr of the simulation. (B): Volume-fraction of OC material present in the system over time. (C): Volume-fraction occupied by thermochemical piles over time.

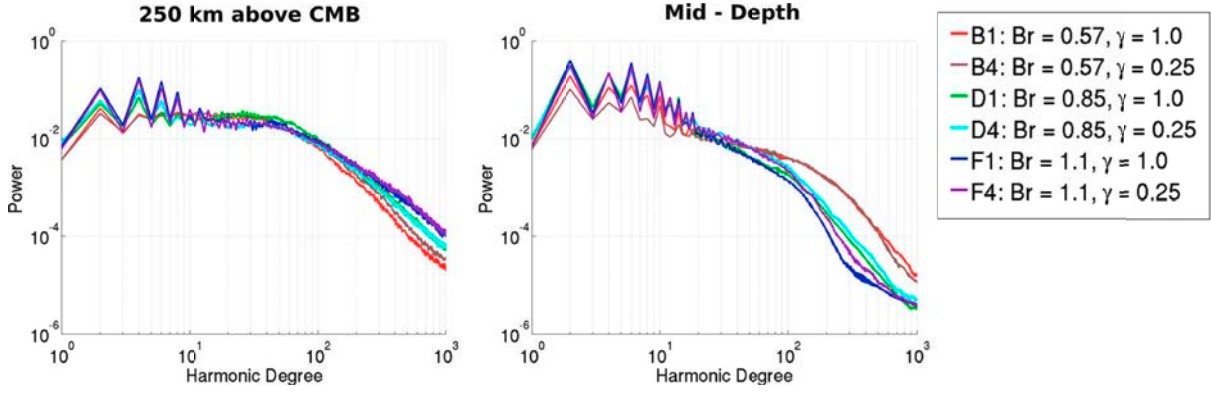


Figure 6.7: Fourier transform of the radial velocity component, measured at two different depths: 250km above CMB (left) and mid-depth of the domain (right), and averaged over the last 500 Myr of simulation.

density material is demonstrated in Figure 6.8, where volume flux of OC material across mid-depth is plotted over time for six different cases (negative flux means in the direction upwards from the CMB). The plotted volume-flux of OC is normalized by that associated with the two downwelling regions, which is governed by prescribed surface velocities and is similar for all cases. The rise of well-stirred thermochemical plumes, reflected in the large negative peaks of OC-flux in Figure 6.8, is observed for cases with $Br < 0.8$. An example of one such event for case **B1** is shown in the insert in Figure 6.8. In some cases, thermochemical plume fails to rise all the way to the surface, and a part of it drains back down. In one such example, shown for case **B4** in the second insert of Figure 6.8, the hottest, least-viscous, and closest to center (i.e. furthest from surrounding ambient mantle) part of the plume drains down, while the rest of the plume continues to rise. Such rare events are reflected in the positive peaks of OC-flux in Figure 6.8. For cases with $Br > 0.8$, entrainment of dense material by plumes is very inefficient - the net OC flux across the mid-mantle exhibits very rare (if any) and small in amplitude negative peaks.

To visualise the individual events associated with variations in entrainment and heat flux, we present the volumetric flux of oceanic crust material and heat flux as functions of time and azimuthal position in Figure 6.9, measured at mid-depth of the domain for five different cases (**B1**, **B4**, **C3**, **F1** and **F4**). Figure 6.9 illustrates the episodic nature of plumes - the yellow-red dots in the heat-flux part of the figure. It is interesting to see the locations of plumes with respect to the locations of the thermochemical piles. For this purpose, we superpose the locations (black lines) of the ‘north’ and ‘south’ boundaries for one of the piles in each simulation onto the heat- and OC-flux color-plots in Figure 6.9.

We can identify three typical locations of plumes with respect to the piles: close to

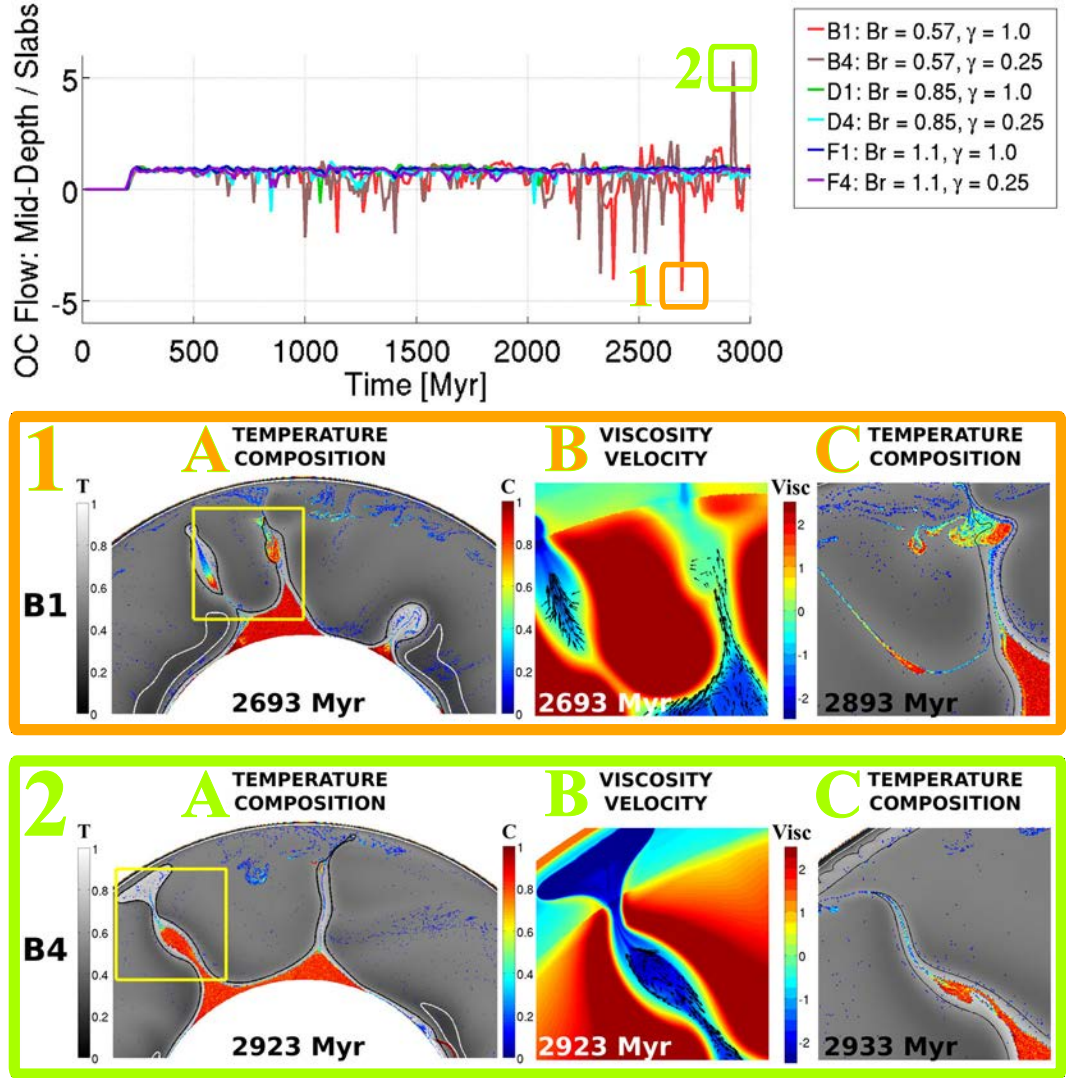


Figure 6.8: *Top:* Volume flux of OC material measured at mid-depth of the domain for six cases (see legend), scaled by the volume flux of OC material transported by subducting slabs. Negative flux means in the direction upwards from CMB. Events associated with one of the negative peaks (orange box) in case **B1**, and one of the positive peaks (green box) in case **B4** are explained in the inserts 1(A-C) and 2(A-C), respectively. **1(A)** and **2(A)** show temperature and composition fields for one of the piles at the time of their respective peaks, with yellow square marking the region of zoom-in in **1(B-C)** and **2(B-C)**, respectively. **1(B)** and **2(B)**: velocity and base ten logarithm of viscosity fields at the time of the peak. **1(C)** and **2(C)**: temperature and composition fields some time after the observed peak in OC-flow.

both edges of the pile, and the mean lateral position of the pile. The plumes occurring close to the mean lateral position of the pile are cooler and more long-lived, compared to the ones occurring at the edges. Cases with lower viscosities in the bottom 500 km of the domain (**B4** and **F4**) exhibit higher plume-frequency and hotter plumes, compared to their more viscous counterparts (**B1** and **F1**). Plume-formation is strongly suppressed in cases with high buoyancy ratio (**F1** and **F4**), where a high density layer develops on top of the CMB.

The contours of the piles in Figure 6.9 illustrate the transient, or oscillating, nature of the piles geometry: it shrinks and expands laterally over time, and also moves as a whole laterally along the CMB.

Transport of OC material across mid-depth in cases with high Br (**F1** and **F4**) is mostly restricted to the narrow regions associated with the downwellings - downward transport of the oceanic crust, as well as the highly localized regions where the OC material is transported upwards. The latter is associated with the thin filaments of high density material entrained by plumes. In contrast, in cases with a moderate buoyancy ratio (**B1**, **B4** and **C3**), a lot more OC material is traversing the mid-depth of the domain - illuminating both the fact that plumes carry more of the dense material as they rise, and that there is a larger fraction of dense material present as a well-stirred component of the ambient material. In all cases, a christmas-tree like structure can be seen in the plots of the OC material flux, which indicates that plumes carrying high density material upwards tend to migrate towards the center of the piles.

To gain some understanding of how long the anomalously dense material lingers in the lower mantle, before it (in some cases) gets entrained and carried back up to the surface, we show the distribution of the dense material by the end of the simulation, colored according to the time at which it was first converted to oceanic crust (Figure 6.10). To generate this figure, we subdivided the domain into 8×8 km² boxes, and assigned the age to each box according to the ‘oldest’ marker found in its interior. By ‘age’ here we mean the time at which it was first converted to oceanic crust.

Results for four selected cases are shown: **B1**, **C3**, **D4** and **F4**. These results illustrate that the subducted oceanic crust material can reside in the deep mantle for at least 3 Gyr. Once a large scale anomaly is formed, the newly arriving dense material travels along its surface, and thus is more likely to get entrained into rising plumes. This process helps to preserve the ancient material inside the piles, and creates a wealth of different ages of the dense material that gets stirred and embedded within the ambient mantle. In two cases with the highest Br -values (**D4** and **F4**), the newly arriving dense material can sometimes accumulate at the surface of a preexisting pile (or layer), due to the inefficiency of entrainment by plumes, until it finally avalanches into the preexisting large-scale structure.

Formation of large structures with accumulated dense material in our models, as

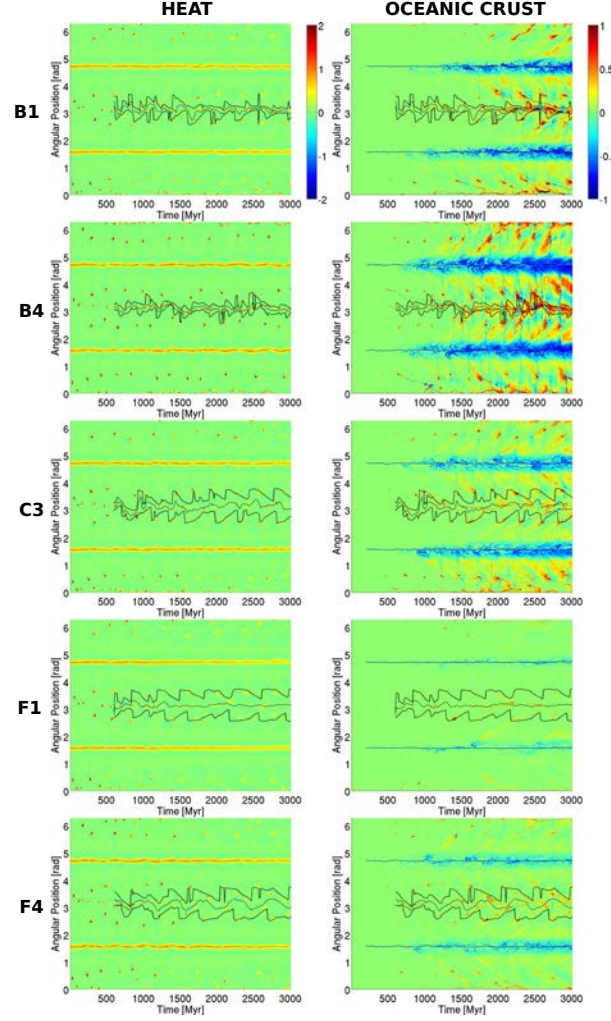


Figure 6.9: Dimensionless heat flux (left) and volume flux of OC material (right), both measured at mid-depth of the domain, as functions of time and azimuthal position for cases **B1**, **B4**, **C3**, **F1** and **F4**. Heat flux colorbar $[-2, 2]$ translates to dimensional values of $\sim [-25, 25]$ kW/m. Flux of OC material is positive when it is away from the CMB, and its colorbar $[-1, 1]$ translates to dimensional values of $\sim [-18, 18]$ m²/yr. The black solid lines superposed on top of each figure indicate the ‘north’ and ‘south’ boundaries for one of the piles. Pile-boundaries are evaluated for the part of the pile that is above its average height over CMB. The dashed black line indicates the mean lateral position of the pile.

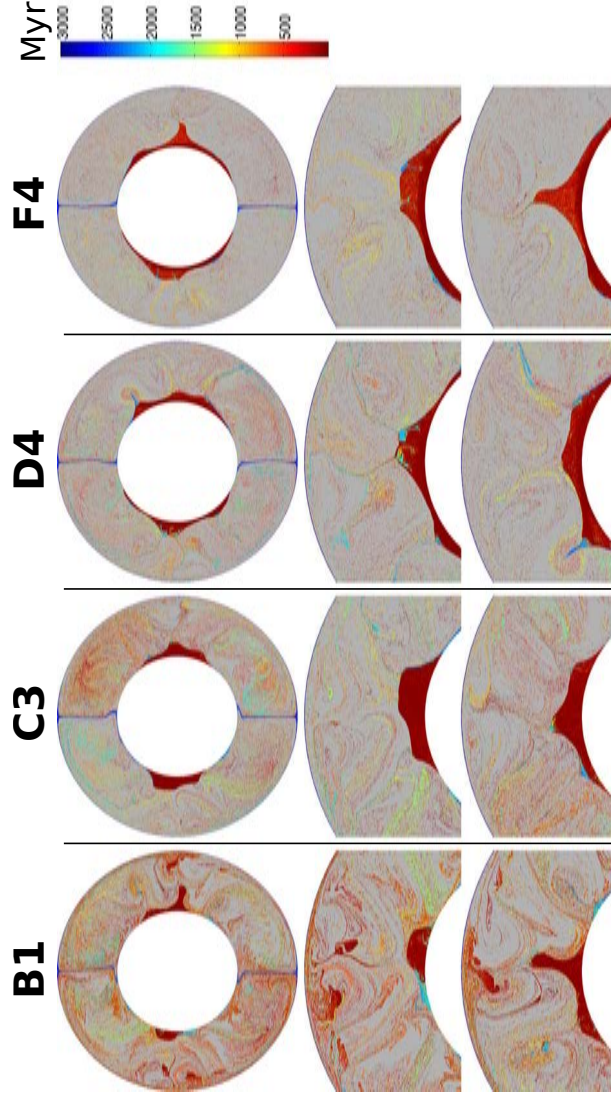


Figure 6.10: Snapshots of cases **B1**, **C3**, **D4** and **F4** at 3 Gyr. Color indicates the time at which material was first converted to oceanic crust. To generate this figure, we subdivided the domain into $8 \times 8 \text{ km}^2$ boxes, and assigned the age to each box according to the ‘oldest’ markers found in its interior. By age here we mean time at which it was first converted to oceanic crust. Top row shows the entire domain, with the zoom in on the left and right piles in the second and third rows of the figure, respectively.

shown in Figures 6.2 - 6.4, the observed compositional heterogeneity in the interior of these structures, as well as the zonation of times when the dense material in different parts of these structures was formed (most notably the preservation of ancient subducted material), as shown in Figure 6.10, point to the time- and space-variations of mechanical mixing of different regions of the mantle. This is visualised in Figure 6.11, where for each point in space, and for a given point in time, the depth at which material was ~ 500 Myr ago is shown (indicated by color). Two ~ 500 Myr-long time-intervals ($[230 - 710]$ and $[3100 - 3600]$ Myr) are analyzed for three different cases: **B1**, **D4** and **F1**. For all presented models, and for both time-intervals, separation of the domain into four large-scale convecting regions is apparent. This large-scale convective pattern is controlled by the prescribed surface velocity, which is the same for all models.

We first look at the earlier of the two presented time-intervals ($[230 - 710]$ Myr). For all of the presented models, material that is in the upper part of the domain at 230 Myr (blue in Figure 6.11) displaces all of the material at the bottom within 500 Myr: i.e., there is no red color immediately at the CMB at 710 Myr. Some of the material that was originally at the bottom (at 230 Myr) traverses approximately twice the mantle-depth within 500 Myr, and is seen reentering the deeper mantle again at the subducting regions at 710 Myr. In cases with $\gamma = 1.0$ (**B1** and **F1**), the reentering material doesn't reach the CMB again, but circulates upwards as part of the return flow surrounding the subducting regions. In contrast, in case with $\gamma = 0.25$ (**D4**), some of the material that was displaced from the CMB ~ 500 Myr ago is being returned back to the CMB.

Flow of the material away from the CMB happens episodically, in form of hot rising plumes with large heads and narrow conduits. Remnants of plumes which drained the material that was originally at the CMB (at 230 Myr) are seen as streaks of red conduits, often tilted. Some of the remnant tails are colored deep red, and indicate the oldest plumes, consisting of material that was at the CMB at the very beginning of the time-interval. There are also remnant tails consisting of material colored from light-orange to light-blue. These are plumes that formed from a more recently formed hot thermal boundary layer. Finally, plumes initiating at 710 Myr, whose heads can be seen in the presented plots in Figure 6.11, consist partially of material that was in the upper part of the mantle, and partially of that in the lower part of the mantle 500 Myr ago (at 230 Myr). Notably, the axis of symmetry in some of these plumes clearly separates the materials that were initially at different depths, most easily seen in the early stages of plume-head development, and getting increasingly mechanically mixed as the plume-head rises.

Some segregation and accumulation of oceanic crust material can be seen at 710 Myr, as deep blue regions that are thickened beneath the upwelling flow.

The striking difference in flow-patterns over ~ 500 Myr observed for the two presented

time-intervals, is that in the later time-interval ($[3100 - 3600]$ Myr), a large fraction of mantle-material at the bottom of the domain does not get displaced by the newly arriving material. These gravitationally stable parts of the mantle are the dense thermochemical piles, which have flow in their interior, but have little material-exchange with the ambient mantle. The newly arriving material travels along the surface of the piles, some of it getting entrained into the piles interior (seen as yellow-green patches in the piles interior for cases **B1** and **D4**), and some of it getting entrained upwards into upwelling flow. This is consistent with the observations from Figure 6.10, where the most recently formed oceanic crust tends to travel along the piles surface, with some of its larger chunks occasionally avalanching into the piles interior.

Similarly to the observation from the earlier time-interval ($[230 - 710]$ Myr), plumes that are rising at 3600 Myr consist partially of material that was in the upper part of the mantle, and partially of that in the lower part of the mantle 500 Myr ago (at 3100 Myr). And, also similar to the earlier time-interval, the axis of symmetry in some of the plumes developing in the later time-interval clearly separates the materials that were initially at different depths.

6.2.2 Pile Scale Time Evolution

We now shift our focus from the global scale characteristics of the thermochemical evolution presented in the previous section, to the evolution of the individual piles. Figure 6.6(C) shows the pile-size evolution, in terms of the fraction of volume occupied by both piles. Despite the low influx of high density material in the models, compared to the more Earth-like values, we observe that by the end of the simulations, the portion of the volume occupied by the thermochemical piles is comparable with the values estimated for the seismically observed LLSVPs ($\sim 2\%$). Growth-rate of the piles in cases with lower Br values (**B1**, **B4**) appears to be declining with time, while in the cases with high Br values (**D1**, **D4**, **F1** and **F4**), the growth rate appears to remain more or less constant.

For a more detailed analysis of the internal structure of the thermochemical piles, we look at the time- and depth-dependence of the following three parameters measured in their interior: concentration of the OC material, temperature, and the total buoyancy anomaly. The latter is defined as the sum of thermally and compositionally induced density variations inside the pile, with respect to the azimuthally averaged values of temperature and composition in the ambient mantle. Results are presented for the individual piles developing on the left and right sides of the domain in Figures 6.12 and 6.13, respectively.

OC-concentration: Piles presented in Figures 6.12 and 6.13 all exhibit some degree of vertical stratification of OC-concentration, which generally decreases away from the

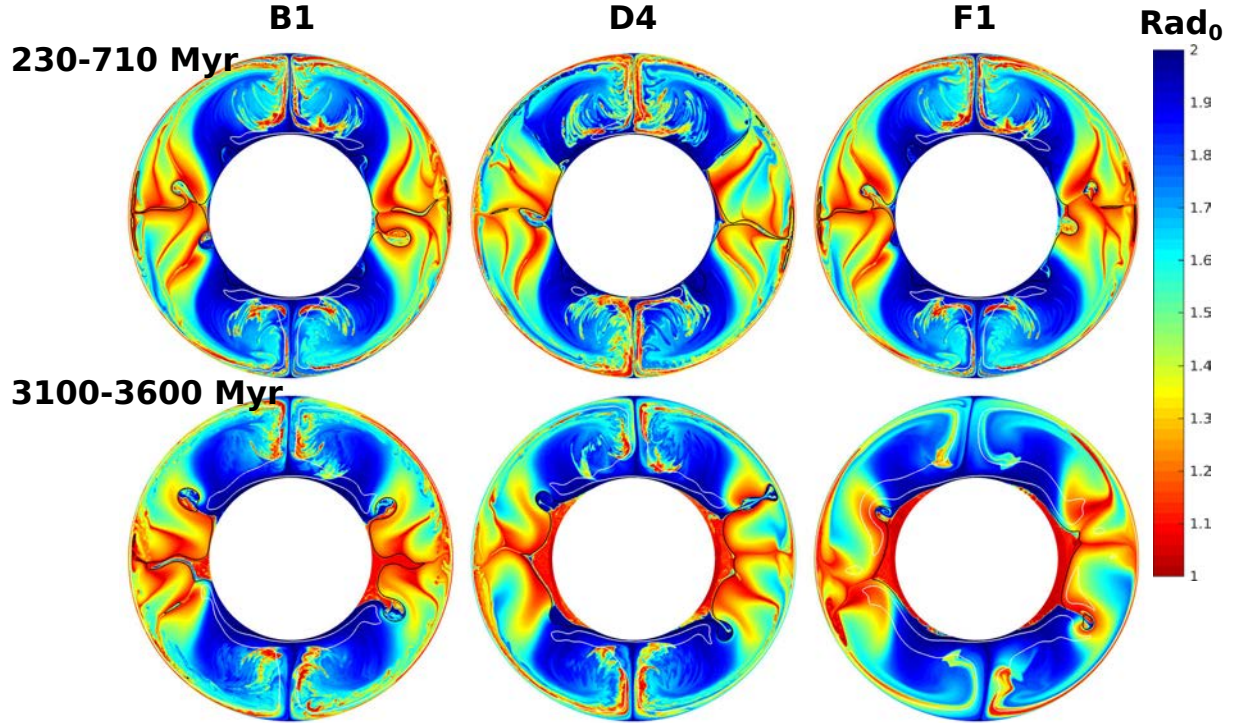


Figure 6.11: Illustrating mantle flow over two ~ 500 Myr-long time-intervals ([230 – 710] (top) and [3100 – 3600] (bottom) Myr) for cases **B1**, **D4** and **F1**, as indicated in the titles of the figures. Color indicates the radial coordinate at which material was at the beginning of the time-interval, with its distribution by the end of the time-interval shown in the figure. For example, dark blue color marks the material that was at the surface of the domain ~ 500 Myr ago. The black and white lines are hot ($T^* = 0.6$) and cold ($T^* = 0.3$) isotherms, respectively (T^* is the nondimensional temperature).

CMB. Intermittantly appearing regions of extremely low OC-concentrations ($< 20\%$) at the surface of the piles, which gets rapidly removed upwards, indicate entrainment by plumes.

In cases with $Br < 0.8$, OC-concentrations in piles interior is more homogeneous (compared to those with $Br > 0.8$), at a value between $\sim 80 - 90\%$ for cases with $\gamma = 1$ (**B1** and **C1**), and between $\sim 65 - 75\%$ for cases with $\gamma = 0.25\%$ (**B4** and **C3**). Piles in cases with $Br > 0.8$ exhibit more vertical stratification of OC-concentration in their interior. Two regions can be distinguished in these cases (least pronounced for case **D4** in Figure 6.12): a high concentration ($\sim 90 - 100\%$) region at the bottom, overlain by a low concentration ($\sim 40 - 60\%$) region. In cases with $\gamma = 1$ (**D1** and **F1**), the high concentration regions are thicker and the low concentration regions are thinner, compared to their counterpart-cases with $\gamma = 0.25$ (**D4** and **F4**).

Temperature: Temperature distribution in the piles interior can also be grouped between cases with $Br < 0.8$ and those with $Br > 0.8$: cases with $Br < 0.8$ exhibit close to a homogeneous thermal structure ($T \sim 0.8 - 0.9$, or $T' \sim 2850 - 3150K$), while cases with $Br > 0.8$ have a notable thermal gradient, with cooler pile-surfaces ($T \sim 0.6 - 0.7$ or $T' \sim 2200 - 2500K$). Note that due to the temperature-dependence of viscosity, a cooler pile-surface is also more viscous.

Net Buoyancy Anomaly: The net buoyancy of the piles with respect to the ambient mantle, shown in Figures 6.12 and 6.13, illustrates that neutrally buoyant thermochemical structures develop in all of the presented cases, and are persistent features that, once developed, survive for several billion years. For cases with $Br > 0.57$ the net buoyancy of the piles generally falls in the range between neutral and negative, with a negatively buoyant bottommost part, and buoyancy increasing upwards until it reaches the level of neutral buoyancy. The positively buoyant parts that intermittently appear at the piles surfaces readily rise away due to their excess buoyancy. In contrast, piles developing in cases with $Br = 0.57$ (**B1** and **B4**) are positively buoyant (albeit only slightly) in the largest fraction of their interior, except for the negatively buoyant bottommost part, and a neutrally buoyant uppermost part. Such buoyancy structure develops due to the variation of azimuthally averaged temperature with depth. Starting from the CMB, the value of azimuthally averaged temperature decreases upwards, until it reaches the depth of ~ 2600 km, at which point it starts rising again until it reaches its adiabatic value at ~ 1500 km depth. Thus, as the positively buoyant thermochemical pile rises through the mantle in the depth-range $\sim 2600 - 1500$ km, it is surrounded by an increasingly hotter mantle, which lowers the effective buoyancy of the pile until neutral (i.e. zero) buoyancy is reached. A positively buoyant lower part of a pile that underlies its neutrally buoyant part was also observed in *Tan and Gurnis* (2005), who suggested such buoyancy structure to be a plausible explanation for high topography yet gravitationally stable thermochemical piles at the bottom of the mantle. The mechanism that generated such buoyancy

structure in their case, however, was depth-dependence of the compositionally induced density anomaly due to the different equations of state used for the ambient and dense materials.

Piles in all of the presented cases exhibit oscillations in their topography over time. The cases with lower Br values (**B1** and **B4**) oscillate most frequently, with pile topographies ranging from below 500 km to over 2000 km above CMB. Time-variations of pile topography get more subtle for cases with increasing buoyancy ratio (**C1**, **C3**, **D1**, **D4**, **F1** and **F4**). In all cases, lowering the viscosity in the bottom 500 km of the domain results in more frequent topography-oscillations.

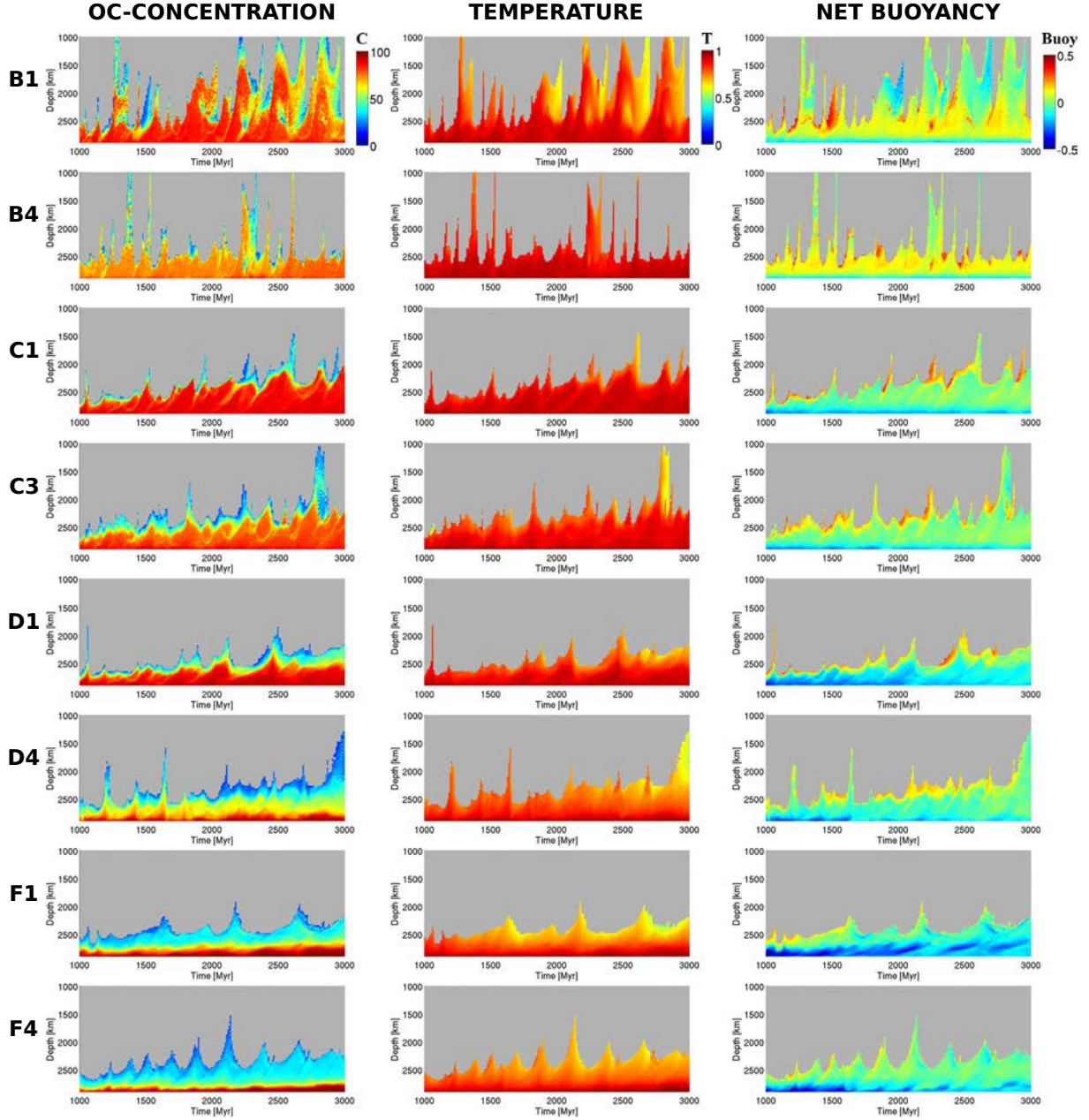


Figure 6.12: Time evolution of concentration of the oceanic crust material (left), temperature (center), and total buoyancy anomaly (right) in the thermochemical piles, as functions of time and depth. Results for the piles on the left side of the domain for eight different cases are shown, as indicated on the left of each row: *B1*, *B4*, *C1*, *C3*, *D1*, *D4*, *F1*, and *F4*.

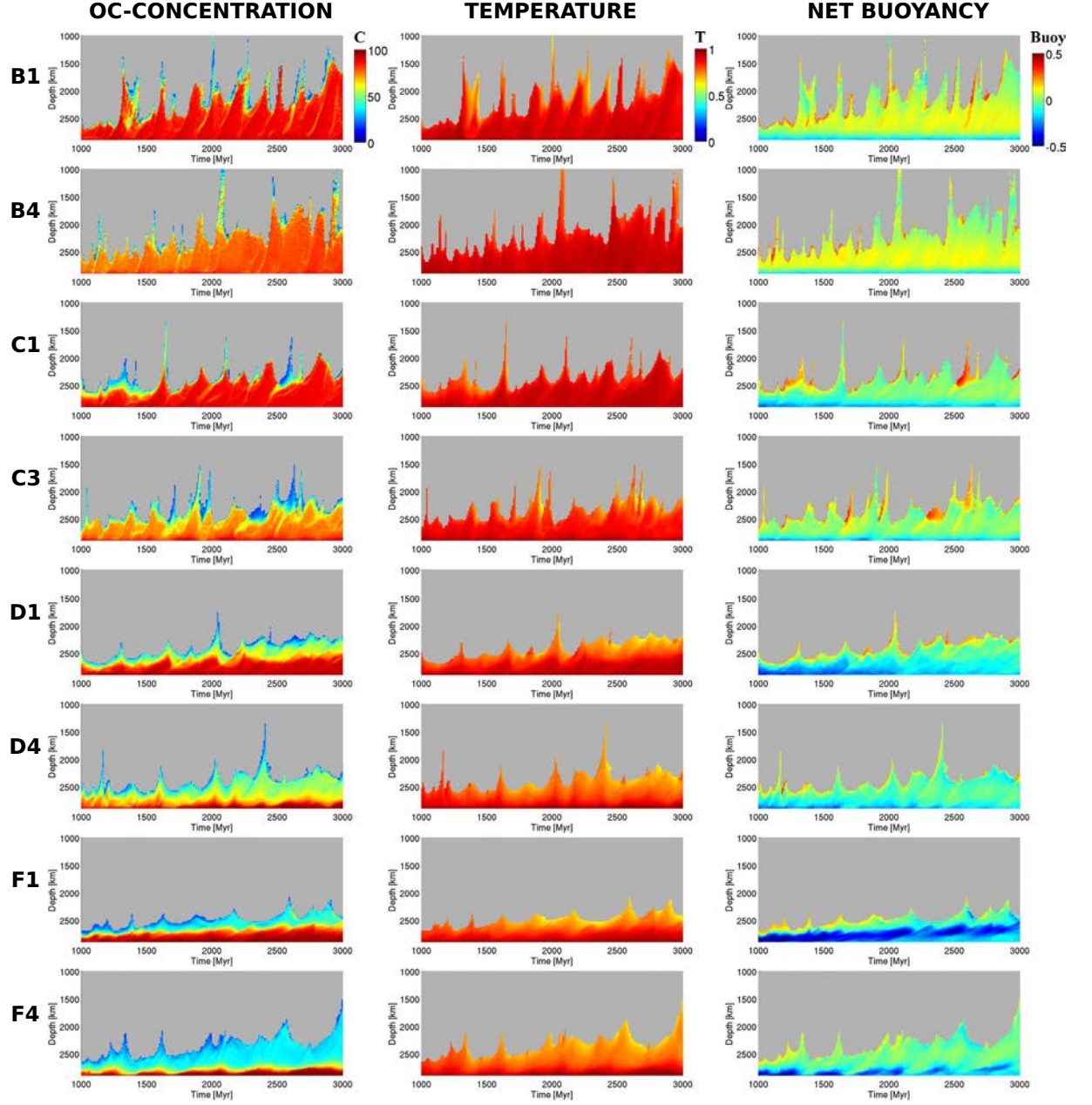


Figure 6.13: Same as Figure 6.12, but for the thermochemical piles on the right side of the domain.

Postprocessing: Distinguishing Thermochemical Piles from Ambient Mantle

In order to distinguish the piles in our numerical results from the rest of the domain, we borrowed some techniques from the field of image analysis. A structured quadratic mesh was superposed to cover the entire domain. The boxes of the structured mesh played the role of pixels in an image. Concentrations of dense material in each box of the structured mesh were treated as a one-dimensional brightness value (ranging from 0 to 1). Brightness values were thresholded to produce a binary ‘image’: all values below 0.1 were set to zero, and everything else set to 1. An inbuilt MATLAB function was used to find the connected components of the image-matrix. The two components that were found to occupy the largest number of ‘pixels’ were considered as piles. The best thresholding value (0.1 in our case) for conversion to a binary ‘image’ was found by visually assessing the results obtained with different thresholding values. Using different thresholding values, we checked how well the result of our algorithm (applied to simulation results from different cases and at different times) agreed with the result we would obtain if we were to manually outline the shapes of the piles. While acknowledging the qualitative and subjective nature of this approach, we found it to be robust for a large range of pile-geometries, and its results largely consistent with what could be obtained with a highly impractical and time-consuming manual approach. We would also like to point out that it is a non-trivial task to make a computer ‘see’ complex, internally heterogeneous geometrical structures, bordering with the challenges of pattern-recognition algorithms in the field of artificial intelligence.

6.2.3 Models Featuring Primitive Dense Basal Layer

We have illustrated that accumulation of large-scale compositional anomaly from thin subducted oceanic crust that segregates to the CMB is geodynamically feasible. To assess whether the supply of newly generated dense material is necessary for large thermochemical piles to survive for over 3 Gyr, we present simulation-results of thermochemical convection excluding the production of oceanic crust. We used model-parameters analogous to case **B1** ($Br = 0.57$, $\gamma = 1.0$), but where density anomaly refers to that of an initially prescribed (primordial) dense basal layer. We tested two different thicknesses of the primordial layer: 50 and 100 km, corresponding to ~ 1.1 and $\sim 2.2\%$ of mantle volume, respectively. Snapshots of the thermochemical evolution for these two cases are presented in Figures 6.14 (top two rows) and 6.15 (first two columns when the title of the plots is horizontal). For both cases, we observe blobs (characteristic length-scale of ~ 10 s– 100 s km) of dense material floating

in the mid-mantle in regions above the thermochemical piles. These blobs point to a step-wise destruction of the dense basal layer, with bigger blobs separating from the layer first, and subsequently getting deformed and mechanically mixed with the ambient flow.

Not surprisingly, the case with a thicker (100 km thick) primordial layer has larger structures surviving until the end of the simulation (for 3.5 Gyr). Figure 6.16 shows the volume fraction of the dense material present in the system (constant with time for these two cases, with small deviation from the initial value due to numerical discrepancies), and the pile-size evolution, in terms of the fraction of volume occupied by both piles, for the two cases. The apparent initial increase in the pile-volume fraction (first $\sim 100 - 200$ Myr) appears in this plot because of the way we measure the size of the piles (described in detail in the end of Section 6.2.2). Material that can potentially be considered as piles excludes the part of the mantle that is immediately below the downwelling regions. Thus, the initial increase in the pile-volume fraction in Figure 6.16 reflects the displacement of the dense basal layer from beneath the downwelling region.

For both cases, approximately half of the layer gets entrained away, with the rate of entrainment increasing with decreasing amount of material at the CMB (i.e., towards the end of the simulation). For the case with initial layer-thickness of 100 km, dense material that constitutes the remaining piles corresponds to $\sim 1\%$ of mantle-volume, while for the case with initial layer-thickness of 50 km, it is less than 0.5%. These results suggest that it is also geodynamically feasible that the large-scale compositional anomalies observed at the bottom of the mantle today are entirely made up of primordial material, since the entrainment by plumes is not efficient enough to homogenize it completely with the ambient mantle. The required initial volume-fraction of the primordial material depends on its material parameters, such as density, which were not explored in the presented study, but that have been observed to play a role for the rate of entrainment, and thus also for the survival time of the compositional anomaly.

We have observed that supply of newly generated dense material is necessary to maintain a given pile-size for several billions of years. We have also seen that a preexisting large-scale dense anomaly can survive in the deep mantle for billions of years, conditional on its initial thickness and material properties, but it shrinks at an increasingly higher rate over time due to entrainment. It is interesting to see the evolution of thermochemical piles when both of these components are at play: continuously generating dense oceanic crust and a preexisting dense basal layer. We present simulation results from two cases with such set-up, which are analogous to cases **B1** ($Br = 0.57$, $\gamma = 1.0$) and **B3** ($Br = 0.57$, $\gamma = 0.5$), but where density anomaly applies to the initially prescribed dense basal layer, as well as to the oceanic crust material (i.e., the prescribed density anomaly for primordial and OC-materials are the same, for

simplicity). Initial thickness of the dense basal layer is 50 km for both cases. Snapshots of the thermochemical evolution for the two cases are presented in Figures 6.14 (bottom two rows) and 6.15 (last two columns when the title of the plots is horizontal). The two cases don't exhibit any observable differences, also in their evolution of the volume fraction of the dense material present in the system, and the pile-size, shown in Figure 6.16. Thus, lowering the viscosity in the bottom 500 km of the domain for this set of parameters doesn't have any significant influence on the result. Similarly to what was observed for the two cases with primordial layer, but which didn't have OC-generation, there are blobs of dense material floating in the mid-mantle in regions above the thermochemical piles, indicative of the step-wise destruction of the piles: first a blob with a characteristic length-scale of $\sim 10\text{s} - 100\text{s}$ km gets separated from the piles, then it gets continuously deformed by ambient flow, and eventually homogenizes with the ambient mantle.

The large-scale compositional structures produced in case **B1** with a primordial layer and OC-generation (and which are largely similar to the ones produced in case **B3** with a primordial layer and OC-generation) can be compared to the structures evolving in case **B1** where there is no primordial layer (shown in Figures 6.3- 6.4, with their pile-size evolution shown in Figure 6.6(C)). Evolution of the size of the piles for the two cases with primordial layer and OC-generation is shown in Figure 6.16. The piles appear to be increasing in size at a rate that decreases with time, with their size reaching an approximate steady-state after ~ 3 Gyr, at volume-fraction of just over 3%. After ~ 1.3 Gyr piles occupy just over 2% of the total mantle volume, which is the approximate steady-state pile-size value for case **B1** where there is no primordial layer. Thus, it appears that the piles evolving in cases with a preexisting dense basal layer tend towards a dynamic steady state with piles that are larger than those in cases with no preexisting layer. Part of the explanation for this result is that the piles evolving in cases with a preexisting dense basal layer have a higher concentration of dense material in their interior, and are thus denser and more difficult to entrain, compared to piles evolving solely from the segregated crust. This is because in the latter case, viscous coupling opposes complete separation of oceanic crust from the ambient material, thus the forming pile consists of the mixture of the two materials.

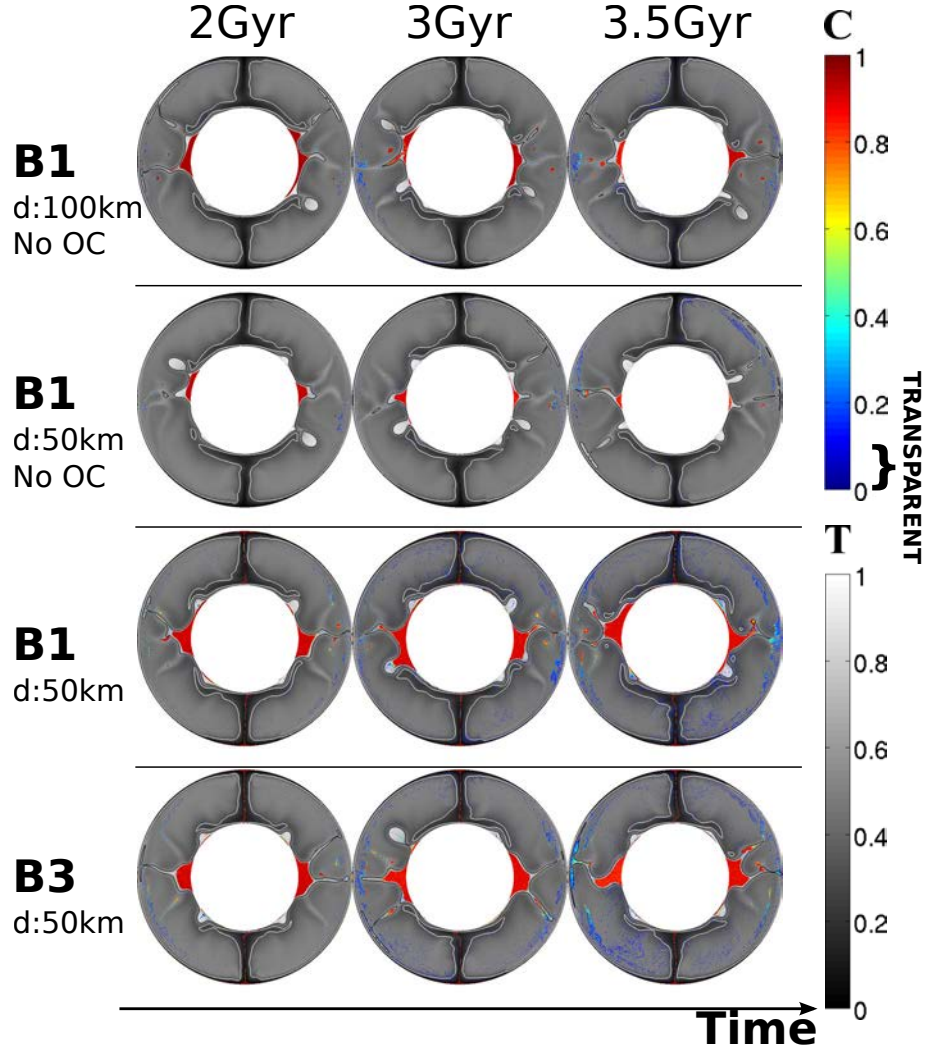


Figure 6.14: Snapshots of the thermochemical evolution at three points in time (2, 3, and 3.5 Gyr) for four different cases featuring a primitive dense basal layer (from top to bottom): B1 ($Br = 0.57$, $\gamma = 1.0$) with initial layer thickness $d = 100\text{km}$ and no OC-generation, B1 with initial layer thickness $d = 50\text{km}$ and no OC-generation, B1 with initial layer thickness $d = 50\text{km}$ and with OC-generation, and B3 ($Br = 0.57$, $\gamma = 0.50$) with initial layer thickness $d = 50\text{km}$ and with OC-generation. The gray-scale reflects the thermal field (bottom colorbar), and the red-blue scale reflects the concentration of oceanic crust material (top colorbar). Concentrations of OC material lower than 0.1 are made transparent. The black and white lines are hot ($T^* = 0.6$) and cold ($T^* = 0.3$) isotherms, respectively (T^* is the nondimensional temperature).

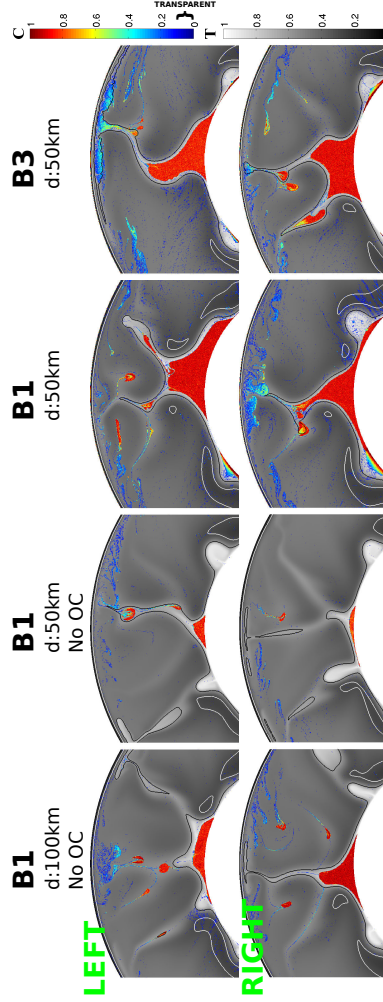


Figure 6.15: Snapshots at 3.5 Gyr for, zoomed in on the thermochemical piles that develop on the left (top row) and right (bottom row) side of the domain. Results for four different cases featuring a primitive dense basal layer are shown (from top to bottom): B1 ($Br = 0.57$, $\gamma = 1.0$) with initial layer thickness $d = 100\text{km}$ and no OC-generation, B1 with initial layer thickness $d = 50\text{km}$ and no OC-generation, B1 with initial layer thickness $d = 50\text{km}$ and with OC-generation, and B3 ($Br = 0.57$, $\gamma = 0.50$) with initial layer thickness $d = 50\text{km}$ and with OC-generation. The gray-scale reflects the thermal field (bottom colorbar), and the red-blue scale reflects the concentration of oceanic crust material (top colorbar). Concentrations of OC material lower than 0.1 are made transparent. The black and white lines are hot ($T^* = 0.6$) and cold ($T^* = 0.3$) isotherms, respectively (T^* is the nondimensional temperature).

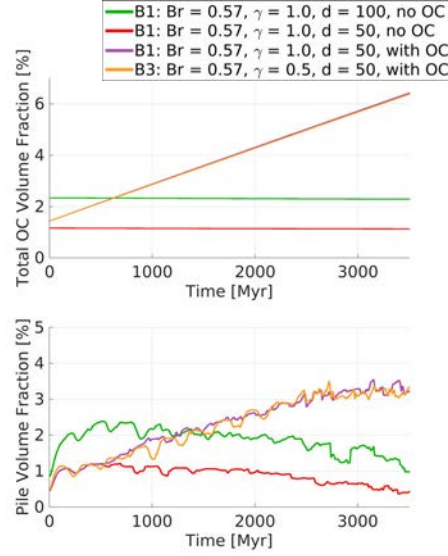


Figure 6.16: Volume-fraction of OC material present in the system over time and volume-fraction occupied by thermochemical piles over time for four different cases, as indicated by the legend.

6.3 Discussion

For a range of parameters tested in this study, a large-scale compositional anomaly forms at the CMB from the segregated oceanic crust, which is similar in shape and size to the seismically observed LLSVPs - high topography of over 1000 km with steep edges (Figures 6.3 - 6.4), and occupying a few % ($\sim 2\%$) of the total 2D-volume (Figure 6.6(C)).

Once formed, the large scale anomaly survives for several billion years. Formation and long-term survival of the thermochemical piles occur in our models despite the low influx-rate of oceanic crust material, which results from a low value of the tectonic plates velocity prescribed at the surface. Low influx of OC material together with excessively strong upwelling flow (due to absence of internal heating) constitute unfavorable conditions for the formation of the piles. On the other hand, the prescribed stable locations of the downwelling regions, where the dense OC material gets transported into the mantle depth, facilitates the formation and survival of thermochemical piles. Strong thermally induced viscosity variations present in our models also favor segregation of OC material to the CMB, and subsequent formation of thermochemical piles with highly heterogeneous internal structure.

In our simulations, neutrally buoyant thermochemical piles - those in which the thermally induced negative density anomaly is balanced by the presence of a fraction

of compositionally anomalous high density material - best resemble the geometry of LLSVPs. Interestingly, such neutrally buoyant piles tend to emerge and survive for a long time (several Gyr) in simulations that span a large range of parameters. In cases with moderate values of $Br = 0.57$ and 0.71 , the neutrally buoyant piles contain $\sim 80\%$ of dense OC material, which scales to a net compositionally induced density anomaly associated with the piles of ~ 80 and 100 kg/m^3 , respectively. For high values of $Br = 0.85$, 0.99 and 1.1 , a dense layer (concentration of OC $\sim 100\%$) forms at the base of the mantle, and a neutrally buoyant pile develops on top of it (concentration of OC $\sim 30\%$). This scales to a compositionally induced density anomaly associated with the dense layer of ~ 150 , 175 and 200 kg/m^3 , respectively, and that associated with the overlying neutrally buoyant piles of ~ 45 , 52 and 60 kg/m^3 , respectively. The dense basal layer and the neutrally buoyant pile on top of it are clearly separated by a jump in the concentration of the compositionally anomalous material (Figures 6.12 and 6.13). In cases with both moderate and high Br -values, the shapes of the neutrally buoyant piles vary through time between ridge-like and dome-like.

The observed spatial distribution of the OC material within the large-scale anomalies can be grouped into two categories: (i) large topography piles with sharp edges, which are highly mobile both laterally and vertically, have a homogeneous distribution of dense material in their interior, and have plumes rising from their surface and edges, occasionally entraining large bulks of the pile-material; (ii) high density basal layer covering nearly the entire CMB, overlain by high topography piles with a much lower fraction of OC material, and plumes rising from their interior and edges, entraining thin filaments of pile material. Scenario (i) is typical for the cases with moderate buoyancy ratio ($Br < 0.8$), while scenario (ii) is typical for high buoyancy ratios ($Br > 0.8$). The role of reduced viscosity in the bottom 500 km is to decrease the concentration of the OC material in the pile, resulting in a more diluted - and thus more positively buoyant - mixture (Figures 6.3 - 6.4, and 6.12 - 6.13).

Concentration and spatial distribution of dense material within the piles is strongly influenced by the motion in the piles interior. It can be induced by small-scale convective heat transport, due to heat flowing from the CMB, given that the piles Ra number is above critical (e.g. that the pile is sufficiently thick). Motion within the pile can also result from plumes rising in its vicinity - due to viscous coupling of the two. Lowering viscosity in the lowermost mantle is expected to increase the internal motion of the pile - both due to the resulting increase in the piles local Ra number, and due to higher velocity of the material rising in plumes in the vicinity of the piles. The effect of the latter can be somewhat compensated by the decrease in viscous drag, as drag itself is also proportional to viscosity. Looking at the results presented in Figures 6.3 - 6.4, we observe that for a given intrinsic density anomaly of OC-material, lowering the viscosity in the bottom 500 km of the mantle results in

lower concentration of the dense material within the piles, consistent with the above discussion.

Motion within the pile also affects the spatial distribution of dense and ambient materials in its interior, with more vigorous motion resulting in more homogeneous distribution. Distribution of the pile-materials towards a homogenized well-stirred mixture is opposed by the effect of buoyancy, that arises due to the intrinsic density difference between the materials. Buoyancy acts to create a higher concentration of dense material closer to the CMB, and a lower concentration closer to the surface of the pile. Increasing the buoyancy ratio is thus expected to result in more (vertically) heterogeneous compositional structure. This is, indeed, what is observed in Figures 6.3 - 6.4: for a given viscosity structure, increasing the density anomaly of the OC-material leads to a more vertically stratified distribution of dense material in the pile.

Analysis of spatial distribution of dense material within the thermochemical piles, together with the point in time when this material was converted from ambient to OC material, reveals that a thermochemical pile is constituted by the representatives of OC material of different ages. This further implies that when a mantle plume entrains pile-material, i.e. the previously subducted OC material, and brings it back to the Earth's surface - the geochemical signature of this compositionally anomalous material may vary from plume to plume, or even within the same plume. The property of a thermochemical pile to contain oceanic crust material that was formed at different points of Earth's history, and possibly at different locations on the surface, provides a plausible explanation for how one large scale reservoir of anomalous material (e.g. an LLSVP) can provide a wide range of isotopic signals in mafic deposits at the surface. To gain some physical intuition into the processes responsible for the observed behavior and evolution of thermochemical piles, it is helpful to think of the piles and the rest of the mantle as two separate systems. A pile represents a reservoir linked to the rest of the mantle through exchange of heat and material. Heat enters the pile by diffusion from the hot CMB. Heat escapes the pile through diffusion across the interface between the pile and the ambient material, as well as through (i) influx of the newly arrived cold dense material, (ii) influx of the cold ambient material by entrainment (due to the motion within the pile), and (iii) departure of the hot pile-material that gets entrained into hot rising plumes. Processes (i)-(iii) also describe the material exchange between the pile and the ambient mantle.

It is reasonable to assume that the rate at which dense OC material enters the pile (process (i)) is more or less constant throughout the simulation-time. This is because this process is governed by the rate of subduction, which brings the dense material to CMB, and which is controlled by the prescribed surface velocities. The rate at which ambient material enters the pile (process (ii)) is determined by the interior motion of the pile and viscosity in the vicinity of the interface between the pile and the ambient

material.

Formation of a dense basal layer takes place when process (i) - influx of the newly arrived dense material - completely dominates over processes (ii) and (iii) - influx of ambient mantle material into pile (or layer), and entrainment of pile-material into plumes. As the basal layer continues to grow - the temperature at its surface sinks, as it rises further away from the CMB. Lower temperature leads to higher viscosity at the surface of the layer - and thus stronger drag imposed on the layer by the thermal plumes rising off its surface. Increasingly strong viscous drag destabilizes the dense material at the surface of the layer. Plumes may not always manage to carry a thin filament of dense material all the way up to the surface, and the initially entrained filament collapses back onto the surface of the layer. The filament does not collapse alone, however, but with a fraction of ambient mantle material viscously coupled to it. Repeated action of this process of entrainment and collapse is responsible for the formation of a secondary thermochemical pile on top of the dense basal layer. Due to the elevated viscosity within this low OC-concentration secondary pile (compared to the low-viscosity and high temperature layer closer to the CMB), as well as the small thickness of the destabilized filaments (due to high buoyancy ratio - viscous drag is only capable of destabilizing very small volumes of dense material), the dense material within the secondary pile is prevented from segregating back to rejoin the dense basal layer. The observed stability of the neutrally buoyant low OC-concentration pile on top of the dense basal layer points to the balance in the rate at which new dense filaments are formed and start contributing to the pile, and the rate at which plumes manage to carry the pile-material away - all the way up to the surface.

Our modeling results suggest that the domains in the diagram from *Le Bars et al.* (2004, Figure 2), which classifies different patterns observed in thermochemical convection at different buoyancy and viscosity ratios (albeit in their case - both due to intrinsic material properties), are not model-specific. Rather, several domains can be present within one system: a thin dense basal layer where conduction is the dominant heat-transport mechanism, underlying a flat layer that is internally convecting, which is overlain by a high topography layer with yet lower concentration of dense material, and - the cherry on top - the neutrally buoyant oscillating dome topping off the large scale compositional anomaly. Compositionally dense material that fails to become a part of the aforementioned structures gets stirred and thinned by ambient flow, and eventually becomes dynamically indistinguishable from the ambient mantle. If the intrinsic density of compositionally anomalous material (OC in our case) is too low to form any of the dense basal layers - only the neutrally buoyant high topography pile is observed. For yet lower values of intrinsic density - no material manages to segregate, and the two materials mix and eventually form a homogeneous mixture.

6.4 Model Limitations

6.4.1 Boussinesq Approximation

Assuming incompressibility of the mantle across its depth is not a fully justified approximation for mantle-like thickness and material-properties (e.g. *Schubert et al.*, 2001). While some purely thermal mantle convection studies have shown that compressibility may not play a crucial role in determining its convective pattern (*Bercovici et al.*, 1992), other geodynamic studies demonstrated that including compressibility into mantle convection models, which introduces viscous heating and depth-dependence of material properties such as density, expansivity, diffusivity and heat capacity, tends to reduce the convective vigor of the system (*Tackley*, 1996). Of most relevance to our study are the effects that compressibility introduces in thermochemical convection, which are absent from our model. In particular, *Hansen and Yuen* (2000) have shown that the depth-dependence of thermal expansivity, i.e. its decrease with depth, facilitates the preservation of a compositionally dense basal heterogeneity. Additional effects of compressibility come from the notion that different materials (e.g. subducted MORB and ambient mantle) may have different bulk moduli, and consequently different adiabatic density profiles. This leads to depth-dependence of density contrast between these materials, and gives rise to thermochemical structures that can only be observed in compressible convection models, such as oscillating and stagnating plumes (*Samuel and Bercovici*, 2006) and metastable superplumes (*Tan and Gurnis*, 2005, 2007).

6.4.2 Cylindrical Geometry

Different ways of constructing two-dimensional models that can reflect physical processes occurring in a more Earth-like three-dimensional sphere have been proposed (e.g. *van Keken*, 2001; *Hernlund and Tackley*, 2008). The quantities often considered are heat flux, usually in terms of the Nusselt number (Nu), the characteristic flow velocity, usually in terms of the root-mean-square or surface velocity, and the characteristic length-scales of thermal structures, such as distance between neighboring upwellings or downwellings. For a two-dimensional hollow-cylinder geometry (such as in our model), geometrical parameters that need to be prescribed are inner (R_i) and outer (R_o) radii. Scaling R_i and R_o directly to the radii of the outer core (≈ 3486 km) and the surface of the Earth (≈ 6371 km), respectively, gives $R_i = 1.2083$ and $R_o = 2.2083$, where the nondimensional depth of the mantle is chosen to be 1. *van Keken* (2001) have shown that this choice of geometry results in an overestimation

of heat flux and flow velocity, and that a scaling with $R_i = 0.4292$ and $R_o = 1.4292$ produces results that more closely resemble thermal convection in a sphere. The fact that increasing the curvature of the cylinder (decreasing the ratio of inner to outer radii) leads to a decrease in heat flux has been previously demonstrated in a systematic numerical study of *Jarvis* (1993). An analogous effect of curvature on heat transport properties has also been demonstrated in models of mantle convection in three-dimensional spherical geometry (*Hosein Shahnas et al.*, 2008; *Deschamps et al.*, 2010). However, *Hernlund and Tackley* (2008) have pointed out that using such small inner radius for cylindrical geometry as proposed by *van Keken* (2001) leads to an artificial ‘crowding’ of thermal and compositional structures at the base of the mantle. Further, as was pointed out by *Hosein Shahnas et al.* (2008), mechanical boundary conditions (e.g. free slip or prescribed velocities) may also play a role in the resulting heat flux of a model. Similar observation was made in *van Keken and Ballentine* (1999), namely that one cannot independently adjust model-parameters such as plate-velocities and heat-flow.

With these limitations in mind, we choose to set the nondimensional inner and outer radii of our cylindrical domain equal to 1 and 2, respectively. It is an intermediate scaling compared to the ones studied in *van Keken* (2001). With this choice of model-parameters, including the geometrical parameters, the previously described mechanical boundary conditions (Section 6.1), and the viscosity model (Chapter 5), we observed that Nu (here measured as the non-dimensional conductive surface heat flux) in our models never exceeded the value of 16. This value is on the lower end of the range suggested for the surface of the Earth (Nu between 14 and 23, as summarised in *van Keken and Ballentine* (1999)). Just to get an idea of how the non-dimensional heat flow values obtained in our models relate to Earth, we dimensionalised the values of circumference-averaged conductive radial heat flux, measured at top and bottom boundaries of our models, and integrated these over the spherical surface-area of the Earth and CMB, respectively. Thus, in dimensional terms, the range of present-day surface heat flow values obtained in our models is 18 – 25 TW, which is somewhat smaller than the estimated mantle heat flow of 32 TW (*Jaupart et al.*, 2007). For further comparison, the present-day surface heat flow obtained in the ‘best fit’ thermochemical convection model of *Nakagawa and Tackley* (2014), who used a spherical annulus geometry as described in *Hernlund and Tackley* (2008), is about 30 TW. The range of the present-day CMB heat flow values obtained in our models is 7 – 13 TW, which is larger than the theoretical estimates of $\sim 2.1 - 3.4$ TW in *Buffett* (2002), but within the range of the more recent estimates of $\sim 5 - 15$ TW, as summarised in *Lay et al.* (2008). Conversely, the most successful thermochemical convection model of *Nakagawa and Tackley* (2005), who used a scaled cylindrical geometry as described in *van Keken* (2001), predicts a present-day CMB heat flow of 8.5 TW. The low surface heat flow values obtained in our models are likely due to our chosen value

for the prescribed surface velocity, which is lower than the typical tectonic velocities. The high CMB heat flow in our models is partially due to the choice of geometry, which overestimates the ‘surface’ of the hot CMB, and partially due to the absence of internal heating.

6.4.3 Prescribed Surface Velocity

The constant in time prescribed surface velocity in our models is an oversimplification of plate tectonics at the Earth’s surface, where plate boundaries migrate, new plate boundaries get created, and old boundaries stop being active, or get extinguished altogether. Rearrangement of plate boundaries with time leads to an unsteady mantle convection pattern, which, in turn, can lead to more chaotic mantle flow and more efficient stirring of chemical heterogeneities (*Gurnis and Davies, 1986a; Kellogg and Turcotte, 1990; Christensen, 1989*). Thus, our chosen constant in time surface boundary conditions facilitate the segregation and preservation of dense material at the base.

6.4.4 Internal Heating

For simplicity, we don’t include internal heating into our models. One of the consequences of excluding the internal heating mode are excessively hot and buoyant thermal plumes, compared to what is expected in a more Earth-like convection. While excess buoyancy contributes to faster ascent of the plume, and thus promotes entrainment and destruction of the compositionally dense anomaly, the hotter temperature of the plume also makes it less viscous, and thus lowers its ability to entrain the dense material. The net effect of excessively hot plumes on entrainment is thus difficult to assess.

Further, radioactive elements are distributed heterogeneously throughout the Earth’s mantle, giving rise to thermal variations that cannot be captured by our model. In particular, because radioactive elements preferentially enter the basaltic component upon mantle-melting at the surface, the oceanic crust has a higher concentration of these heat-producing elements compared to ambient mantle. Thus, a large scale compositional anomaly made up by segregated oceanic crust, as featured in our models, experiences more internal heating than the ambient mantle. The resulting excess heat of the piles would make them less gravitationally stable, compared to the ones produced in our models.

Further, lack of internally generated heat may lead to an excessively cool mantle. However, this effect may be somewhat compensated by our choice of the two-dimensional cylindrical geometry, with the hot inner boundary that is relatively large

compared to the cool outer boundary. On similar effects of model-geometry on the heating mode in convection simulations, see *O’Farrell and Lowman* (2010).

6.4.5 Stress Exponent

When the diffusion creep is the dominant deformation mechanism, the material behaves like a Newtonian fluid, and the dependence of strain rate on stress is linear, i.e. $n = 1$. When the fluid deforms predominantly by dislocation (or power-law) creep, this dependence is normally approximated to be given by $n = 3$ (e.g. *Karato*, 2008). Which values of n are appropriate in different regions of the mantle is not well constrained. Laboratory studies (e.g. *Karato et al.*, 1995; *Karato and Wu*, 1993) and inferences of mantle anisotropy structure from seismological studies (*Becker*, 2006; *Karato*, 1998) favor the dominance of dislocation creep in the shallow upper mantle, and possibly inside the D” layer, and dominance of diffusion creep in the lower mantle.

The effect of different mantle rheology models, linear or non-linear, on the mantle flow has been studied in *Christensen* (1983, 1984). The general effect of non-linear rheology has been found to reduce the viscosity variations associated with pressure- and temperature-dependence, compared to the linear rheology case. In the same study it has been demonstrated that the non-linear rheology can be closely imitated by a Newtonian flow with a reduced value of activation enthalpy, by a factor of 0.3 – 0.5. The main difference between a power-law flow imitated by a Newtonian flow with a reduced enthalpy, and an actual power-law, is the tendency of the latter to concentrate the deformation into certain regions. This effect is important for incorporating self-consistent plate-tectonics into mantle convection models, which may require weakening of the lithosphere in the subduction zones due to stress concentrations. However, our current model does not include this feature.

6.5 Conclusions and Outlook

We conclude from our numerical study that for a plausible range of values of density anomaly of OC material in the lower mantle - it is likely that it segregates to the CMB, gets mechanically mixed with the ambient material, and forms neutrally buoyant large scale compositional anomalies similar in shape to the LLSVPs. Magnitude of the compositionally induced density anomaly associated with the neutrally buoyant parts of these structures ranges from 45 – 100 kg/m³, depending on the intrinsic density anomaly of OC material in the lower mantle, and distribution of OC material

within the piles. Segregation and accumulation of subducted oceanic crust readily takes place in our models, despite some properties of the models that are unfavorable to these processes: such as absence of internal heating, and low prescribed surface velocities.

Once segregated, the dense material undergoes mechanical stirring that acts to create a large-scale compositional anomaly with a heterogeneous internal structure - both in terms of concentration of dense material and temperature.

In cases with moderate buoyancy ratios, the neutrally buoyant piles develop directly on top of the CMB. Their interior doesn't exhibit any significant radial trends in OC-concentration or temperature, but there exist, however, transient thermal and compositional heterogeneities. Further, in cases with moderate buoyancy ratios, neutrally buoyant thermochemical plumes are observed, which are efficient at transporting high density material upwards from the CMB, and thus at destroying the compositional anomaly. Such events are relatively rare, and require a preliminary action of mechanical stirring at the bottom of the mantle - to form a diluted mixture of ambient and dense materials that constitutes the thermochemical plume.

In cases with high buoyancy ratios, the neutrally buoyant piles develop on top of a high density (i.e. high OC-concentration) layer, which forms prior to pile-formation, and covers large fraction of the CMB. Plumes that develop in these cases are significantly colder than the ones developing in moderate buoyancy ratio cases, and only manage to entrain thin filaments of high density material as they rise.

In all of the studied cases we commonly observe plumes that consist of materials which, at least 500 Myr prior to being incorporated into the plume, were occupying two opposite sides of the domain: the surface and the bottom of the mantle. Strikingly, the axis of symmetry of some of these plumes clearly separates the materials that were initially at different depths. These results infer that plumes carrying materials with different geochemical signatures, and which remain unmixed throughout the plumes ascent through the mantle, are a common feature in thermochemical mantle convection.

As a possible outlook, these results, in addition to illuminating some of the complexity of deep Earth dynamics, can predict possible structures that may develop in the interior of the large scale heterogeneities, such as the LLSVPs. These predictions can then be tested against the results of seismological studies, and thus serve as an additional constraint on models of the deep mantle. Further building on these results, it would be interesting to look at the effect that various possible structures of LLSVPs have on the thermochemical plumes that rise in their vicinity: e.g. thermal anomaly associated with the plumes, amount of OC material that they bring up to the surface, and evolution of these plume-characteristics through time. Such quantities predicted from numerical models can be tested against surface-observations of basaltic volcanism that are thought to be manifestations of deep mantle plumes.

Bibliography

- Allègre, C. J., T. Staudacher, and P. Sarda (1987), Rare gas systematics: formation of the atmosphere, evolution and structure of the earth’s mantle, *Earth and Planetary Science Letters*, *81*(2), 127–150.
- Becker, T. (2006), On the effect of temperature and strain-rate dependent viscosity on global mantle flow, net rotation, and plate-driving forces, *Geophysical Journal International*, *167*(2), 943–957.
- Belytschko, T., Y. Y. Lu, and L. Gu (1994), Element-free galerkin methods, *International journal for numerical methods in engineering*, *37*(2), 229–256.
- Bercovici, D., G. Schubert, and G. A. Glatzmaier (1992), Three-dimensional convection of an infinite-prandtl-number compressible fluid in a basally heated spherical shell, *Journal of Fluid Mechanics*, *239*, 683–719.
- Blankenbach, B., F. Busse, U. Christensen, L. Cserepes, D. Gunkel, U. Hansen, H. Harder, G. Jarvis, M. Koch, G. Marquart, et al. (1989), A benchmark comparison for mantle convection codes, *Geophysical Journal International*, *98*(1), 23–38.
- Bower, D. J., M. Gurnis, and M. Seton (2013), Lower mantle structure from paleogeographically constrained dynamic earth models, *Geochemistry, Geophysics, Geosystems*, *14*(1), 44–63.
- Brandenburg, J., and P. Van Keken (2007), Deep storage of oceanic crust in a vigorously convecting mantle, *Journal of Geophysical Research: Solid Earth* (1978–2012), *112*(B6).
- Buffett, B. A. (2002), Estimates of heat flow in the deep mantle based on the power requirements for the geodynamo, *Geophysical Research Letters*, *29*(12), 7–1.
- Bull, A. L., M. Domeier, and T. H. Torsvik (2014), The effect of plate motion history on the longevity of deep mantle heterogeneities, *Earth and Planetary Science Letters*, *401*, 172–182.

- Burke, K., B. Steinberger, T. H. Torsvik, and M. A. Smethurst (2008), Plume generation zones at the margins of large low shear velocity provinces on the core–mantle boundary, *Earth and Planetary Science Letters*, *265*(1), 49–60.
- Cabral, R. A., M. G. Jackson, E. F. Rose-Koga, K. T. Koga, M. J. Whitehouse, M. A. Antonelli, J. Farquhar, J. M. Day, and E. H. Hauri (2013), Anomalous sulphur isotopes in plume lavas reveal deep mantle storage of archaean crust, *Nature*, *496*(7446), 490–493.
- Calderwood, A. (1999), Mineral physics constraints on the temperature and composition of the earths mantle, Ph.D. thesis, Ph. D. thesis, Univ. of Br. Columbia, Vancouver, BC, Canada.
- Christensen, U. (1983), Convection in a variable-viscosity fluid: Newtonian versus power-law rheology, *Earth and Planetary Science Letters*, *64*(1), 153–162.
- Christensen, U. (1984), Convection with pressure-and temperature-dependent non-newtonian rheology, *Geophysical Journal Of the Royal Astronomical Society*, *77*(2), 343–384.
- Christensen, U. (1989), Mixing by time-dependent convection, *Earth and planetary science letters*, *95*(3), 382–394.
- Christensen, U., and A. Hofmann (1994), Segregation of subducted oceanic crust in the convecting mantle, *Journal of Geophysical Research*, *99*(B10), 19,867–19.
- Coltice, N., and Y. Ricard (1999), Geochemical observations and one layer mantle convection, *Earth and Planetary Science Letters*, *174*(1), 125–137.
- Dabrowski, M., M. Krotkiewski, and D. Schmid (2008), MILAMIN: MATLAB-based finite element method solver for large problems, *Geochemistry Geophysics Geosystems*, *9*(4), Q04,030.
- Davaille, A. (1999), Simultaneous generation of hotspots and superswells by convection in a heterogeneous planetary mantle, *Nature*, *402*(6763), 756–760.
- Davaille, A., F. Girard, and M. Le Bars (2002), How to anchor hotspots in a convecting mantle?, *Earth and Planetary Science Letters*, *203*(2), 621–634.
- Davies, G. (2011), Dynamical geochemistry of the mantle, *Solid Earth*, *2*(2), 159–189.
- Davies, G. F. (2002), Stirring geochemistry in mantle convection models with stiff plates and slabs, *Geochimica et Cosmochimica Acta*, *66*(17), 3125–3142.

- Deschamps, F., and P. Tackley (2008), Searching for models of thermo-chemical convection that explain probabilistic tomography:: I. principles and influence of rheological parameters, *Physics of the Earth and Planetary Interiors*, 171(1-4), 357–373.
- Deschamps, F., and P. J. Tackley (2009), Searching for models of thermo-chemical convection that explain probabilistic tomography. iiinfluence of physical and compositional parameters, *Physics of the Earth and Planetary Interiors*, 176(1), 1–18.
- Deschamps, F., P. J. Tackley, and T. Nakagawa (2010), Temperature and heat flux scalings for isoviscous thermal convection in spherical geometry, *Geophysical Journal International*, 182(1), 137–154.
- Deschamps, F., L. Cobden, and P. J. Tackley (2012), The primitive nature of large low shear-wave velocity provinces, *Earth and Planetary Science Letters*, 349, 198–208.
- Deubelbeiss, Y., and B. Kaus (2008), Comparison of eulerian and lagrangian numerical techniques for the stokes equations in the presence of strongly varying viscosity, *Physics of the Earth and Planetary Interiors*, 171(1-4), 92–111.
- Duretz, T., D. May, T. Gerya, and P. Tackley (2011), Discretization errors and free surface stabilization in the finite difference and marker-in-cell method for applied geodynamics: A numerical study, *Geochemistry, Geophysics, Geosystems*, 12, 07,004.
- Dziewonski, A., and D. Anderson (1981), Preliminary reference Earth model* 1, *Physics of the earth and planetary interiors*, 25(4), 297–356.
- Dziewonski, A., V. Lekic, and B. Romanowicz (2010), Mantle Anchor Structure: An argument for bottom up tectonics, *Earth and Planetary Science Letters*, 299, 69–79.
- Garnero, E., and A. McNamara (2008), Structure and dynamics of Earth’s lower mantle, *Science*, 320(5876), 626.
- Gerya, T. (2010), *Introduction to numerical geodynamic modelling*, Cambridge University Press.
- Gerya, T., and D. Yuen (2003), Characteristics-based marker-in-cell method with conservative finite-differences schemes for modeling geological flows with strongly variable transport properties, *Physics of the Earth and Planetary Interiors*, 140(4), 293–318.

- Gonnermann, H. M., A. M. Jellinek, M. A. Richards, and M. Manga (2004), Modulation of mantle plumes and heat flow at the core mantle boundary by plate-scale flow: results from laboratory experiments, *Earth and Planetary Science Letters*, *226*(1), 53–67.
- Gurnis, M. (1986), The effects of chemical density differences on convective mixing in the earth’s mantle, *Journal of Geophysical Research: Solid Earth (1978–2012)*, *91*(B11), 11,407–11,419.
- Gurnis, M., and G. F. Davies (1986a), Mixing in numerical models of mantle convection incorporating plate kinematics, *Journal of Geophysical Research: Solid Earth (1978–2012)*, *91*(B6), 6375–6395.
- Gurnis, M., and G. F. Davies (1986b), The effect of depth-dependent viscosity on convective mixing in the mantle and the possible survival of primitive mantle, *Geophysical Research Letters*, *13*(6), 541–544.
- Hansen, U., and D. Yuen (2000), Extended-boussinesq thermal–chemical convection with moving heat sources and variable viscosity, *Earth and Planetary Science Letters*, *176*(3), 401–411.
- Hayden, L., and E. Watson (2007), A diffusion mechanism for core–mantle interaction, *Nature*, *450*(7170), 709–711.
- Hernlund, J. W., and C. Houser (2008), On the statistical distribution of seismic velocities in earth’s deep mantle, *Earth and Planetary Science Letters*, *265*(3), 423–437.
- Hernlund, J. W., and P. J. Tackley (2008), Modeling mantle convection in the spherical annulus, *Physics of the Earth and Planetary Interiors*, *171*(1), 48–54.
- Hirose, K., N. Takafuji, N. Sata, and Y. Ohishi (2005), Phase transition and density of subducted morb crust in the lower mantle, *Earth and Planetary Science Letters*, *237*(1), 239–251.
- Hofmann, A. (1997), Mantle geochemistry: the message from oceanic volcanism, *Nature*, *385*(6613), 219–229.
- Hofmann, A. W., and W. M. White (1982), Mantle plumes from ancient oceanic crust, *Earth and Planetary Science Letters*, *57*(2), 421–436.
- Hosein Shahnas, M., J. P. Lowman, G. T. Jarvis, and H.-P. Bunge (2008), Convection in a spherical shell heated by an isothermal core and internal sources: Implications

- for the thermal state of planetary mantles, *Physics of the Earth and Planetary Interiors*, 168(1), 6–15.
- Huang, J. (2008), Controls on entrainment of a dense chemical layer by thermal plumes, *Physics of the Earth and Planetary Interiors*, 166(3), 175–187.
- Huang, J., and G. F. Davies (2007), Stirring in three-dimensional mantle convection models and implications for geochemistry: 2. heavy tracers, *Geochemistry, Geophysics, Geosystems*, 8(7).
- Ishii, M., and J. Tromp (1999), Normal-mode and free-air gravity constraints on lateral variations in velocity and density of earth’s mantle, *Science*, 285(5431), 1231–1236.
- Jackson, M. G., R. W. Carlson, M. D. Kurz, P. D. Kempton, D. Francis, and J. Blusztajn (2010), Evidence for the survival of the oldest terrestrial mantle reservoir, *Nature*, 466(7308), 853–856.
- Jarvis, G. T. (1993), Effects of curvature on two-dimensional models of mantle convection: Cylindrical polar coordinates, *Journal of Geophysical Research: Solid Earth* (1978–2012), 98(B3), 4477–4485.
- Jaupart, C., S. Labrosse, and J. Mareschal (2007), Temperatures, heat and energy in the mantle of the Earth, *Treatise on Geophysics*, 7, 253–303.
- Jellinek, A., and M. Manga (2004), Links between long-lived hot spots, mantle plumes, d , and plate tectonics, *Reviews of Geophysics*, 42(3), RG3002.
- Karato, S. (1998), Seismic anisotropy in the deep mantle, boundary layers and the geometry of mantle convection, *Pure and Applied Geophysics*, 151(2-4), 565–587.
- Karato, S. (2008), *Deformation of earth materials: an introduction to the rheology of solid earth*, Cambridge Univ Pr.
- Karato, S., and P. Wu (1993), Rheology of the upper mantle: a synthesis, *Science*, 260(5109), 771–778.
- Karato, S.-i., S. Zhang, and H.-R. Wenk (1995), Superplasticity in earth’s lower mantle: evidence from seismic anisotropy and rock physics, *Science*, 270(5235), 458–461.
- Kellogg, L., and D. Turcotte (1990), Mixing and the distribution of heterogeneities in a chaotically convecting mantle, *Journal of Geophysical Research: Solid Earth* (1978–2012), 95(B1), 421–432.

- Kellogg, L. H., B. H. Hager, and R. D. van der Hilst (1999), Compositional stratification in the deep mantle, *Science*, *283*(5409), 1881–1884.
- Kobayashi, K., R. Tanaka, T. Moriguti, K. Shimizu, and E. Nakamura (2004), Lithium, boron, and lead isotope systematics of glass inclusions in olivines from hawaiian lavas: evidence for recycled components in the hawaiian plume, *Chemical Geology*, *212*(1), 143–161.
- Krotkiewski, M. (2013), Mutils - a set of efficient modeling tools for multi-core cpus implemented in mex, in *EGU General Assembly Conference Abstracts*, vol. 15, p. 7877.
- Kumagai, I., A. Davaille, and K. Kurita (2007), On the fate of thermally buoyant mantle plumes at density interfaces, *Earth and Planetary Science Letters*, *254*(1), 180–193.
- Labrosse, S., J. Hernlund, and N. Coltice (2007), A crystallizing dense magma ocean at the base of the earths mantle, *Nature*, *450*(7171), 866–869.
- Lay, T., J. Hernlund, and B. A. Buffett (2008), Core–mantle boundary heat flow, *Nature Geoscience*, *1*(1), 25–32.
- Le Bars, M., A. Davaille, et al. (2004), Whole layer convection in a heterogeneous planetary mantle, *J. geophys. Res.*, *109*, B03,403.
- Lee, C., P. Luffi, T. Höink, J. Li, R. Dasgupta, and J. Hernlund (2010), Upside-down differentiation and generation of a primordial lower mantle, *Nature*, *463*(7283), 930–933.
- Lenardic, A., and W. Kaula (1993), A numerical treatment of geodynamic viscous flow problems involving the advection of material interfaces, *Journal of geophysical research*, *98*(B5), 8243–8260.
- LeVeque, R. J. (2002), *Finite volume methods for hyperbolic problems*, vol. 31, Cambridge university press.
- Li, M., and A. K. McNamara (2013), The difficulty for subducted oceanic crust to accumulate at the earth’s core-mantle boundary, *Journal of Geophysical Research: Solid Earth*, pp. 1–10.
- Li, Y., F. Deschamps, and P. J. Tackley (2014), The stability and structure of primordial reservoirs in the lower mantle: insights from models of thermochemical convection in three-dimensional spherical geometry, *Geophysical Journal International*, *199*(2), 914–930.

- Lin, S.-C., and P. E. van Keken (2006), Dynamics of thermochemical plumes: 1. plume formation and entrainment of a dense layer, *Geochemistry, Geophysics, Geosystems*, 7(2).
- Masters, G., G. Laske, H. Bolton, and A. Dziewonski (2000), The relative behavior of shear velocity, bulk sound speed, and compressional velocity in the mantle: implications for chemical and thermal structure, *Earth's deep interior: mineral physics and tomography from the atomic to the global scale*, pp. 63–87.
- McNamara, A., and S. Zhong (2005), Thermochemical structures beneath Africa and the Pacific Ocean, *Nature*, 437(7062), 1136–1139.
- Moresi, L., S. Zhong, and M. Gurnis (1996), The accuracy of finite element solutions of stokes's flow with strongly varying viscosity, *Physics of the earth and planetary interiors*, 97(1), 83–94.
- Mosca, I., L. Cobden, A. Deuss, J. Ritsema, and J. Trampert (2012), Seismic and mineralogical structures of the lower mantle from probabilistic tomography, *Journal of Geophysical Research: Solid Earth (1978–2012)*, 117(B6).
- Mukhopadhyay, S. (2012), Early differentiation and volatile accretion recorded in deep-mantle neon and xenon, *Nature*, 486(7401), 101–104.
- Mulyukova, E., B. Steinberger, M. Dabrowski, and S. V. Sobolev (2015), Survival of llsvps for billions of years in a vigorously convecting mantle: Replenishment and destruction of chemical anomaly, *Journal of Geophysical Research: Solid Earth*.
- Nakagawa, T., and P. J. Tackley (2005), Deep mantle heat flow and thermal evolution of the earth's core in thermochemical multiphase models of mantle convection, *Geochemistry, Geophysics, Geosystems*, 6(8).
- Nakagawa, T., and P. J. Tackley (2014), Influence of combined primordial layering and recycled morb on the coupled thermal evolution of earth's mantle and core, *Geochemistry, Geophysics, Geosystems*, 15(3), 619–633.
- Nakagawa, T., P. J. Tackley, F. Deschamps, and J. A. Connolly (2009), Incorporating self-consistently calculated mineral physics into thermochemical mantle convection simulations in a 3-d spherical shell and its influence on seismic anomalies in earth's mantle, *Geochemistry, Geophysics, Geosystems*, 10(3).
- Nakagawa, T., P. Tackley, F. Deschamps, and J. Connolly (2010), The influence of morb and harzburgite composition on thermo-chemical mantle convection in a 3-d spherical shell with self-consistently calculated mineral physics, *Earth and Planetary Science Letters*, 296(3), 403–412.

- Ni, S., E. Tan, M. Gurnis, and D. Helmberger (2002), Sharp sides to the African superplume, *Science*, *296*(5574), 1850.
- Nutman, A. P. (2006), Antiquity of the oceans and continents, *Elements*, *2*(4), 223–227.
- O’Farrell, K. A., and J. P. Lowman (2010), Emulating the thermal structure of spherical shell convection in plane-layer geometry mantle convection models, *Physics of the Earth and Planetary Interiors*, *182*(1), 73–84.
- Ohta, K., K. Hirose, T. Lay, N. Sata, and Y. Ohishi (2008), Phase transitions in pyrolite and morb at lowermost mantle conditions: implications for a morb-rich pile above the core–mantle boundary, *Earth and Planetary Science Letters*, *267*(1), 107–117.
- Pető, M. K., S. Mukhopadhyay, and K. A. Kelley (2013), Heterogeneities from the first 100 million years recorded in deep mantle noble gases from the northern lau back-arc basin, *Earth and Planetary Science Letters*, *369*, 13–23.
- Ricolleau, A., J.-P. Perrillat, G. Fiquet, I. Daniel, J. Matas, A. Addad, N. Menguy, H. Cardon, M. Mezouar, and N. Guignot (2010), Phase relations and equation of state of a natural morb: Implications for the density profile of subducted oceanic crust in the earth’s lower mantle, *Journal of Geophysical Research: Solid Earth* (1978–2012), *115*(B8).
- Ritsema, J., A. Deuss, H. Van Heijst, and J. Woodhouse (2011), S40rts: a degree-40 shear-velocity model for the mantle from new rayleigh wave dispersion, teleseismic traveltimes and normal-mode splitting function measurements, *Geophysical Journal International*, *184*(3), 1223–1236.
- Samuel, H., and D. Bercovici (2006), Oscillating and stagnating plumes in the earth’s lower mantle, *Earth and Planetary Science Letters*, *248*(1), 90–105.
- Schmeling, H., G. Marquart, and T. Ruedas (2003), Pressure- and temperature-dependent thermal expansivity and the effect on mantle convection and surface observables, *Geophysical Journal International*, *154*(1), 224–229.
- Schmeling, H., A. Babeyko, A. Enns, C. Faccenna, F. Funiciello, T. Gerya, G. Golabek, S. Grigull, B. Kaus, G. Morra, et al. (2008), A benchmark comparison of spontaneous subduction modelstowards a free surface, *Physics of the Earth and Planetary Interiors*, *171*(1), 198–223.

- Schott, B., D. Yuen, and A. Braun (2002), The influences of composition-and temperature-dependent rheology in thermal-chemical convection on entrainment of the d -layer, *Physics of the Earth and Planetary Interiors*, 129(1), 43–65.
- Schubert, G., D. Turcotte, and P. Olson (2001), *Mantle convection in the Earth and planets*, Cambridge University Press.
- Shamos, M. I., and D. Hoey (1975), Closest-point problems, in *Foundations of Computer Science, 1975., 16th Annual Symposium on*, pp. 151–162, IEEE.
- Shewchuk, J. (1996), Triangle: Engineering a 2d quality mesh generator and delaunay triangulator, *Applied computational geometry towards geometric engineering*, pp. 203–222.
- Shirey, S. B., and S. H. Richardson (2011), Start of the wilson cycle at 3 ga shown by diamonds from subcontinental mantle, *Science*, 333(6041), 434–436.
- Sleep, N. (1988), Gradual entrainment of a chemical layer at the base of the mantle by overlying convection, *Geophysical Journal*, 95(3), 437–447.
- Sobolev, A. V., A. W. Hofmann, S. V. Sobolev, and I. K. Nikogosian (2005), An olivine-free mantle source of hawaiian shield basalts, *Nature*, 434(7033), 590–597.
- Sobolev, A. V., A. W. Hofmann, D. V. Kuzmin, G. M. Yaxley, N. T. Arndt, S.-L. Chung, L. V. Danyushevsky, T. Elliott, F. A. Frey, M. O. Garcia, et al. (2007), The amount of recycled crust in sources of mantle-derived melts, *Science*, 316(5823), 412–417.
- Sobolev, S., A. Sobolev, D. Kuzmin, N. Krivolutsкая, A. Petrunin, N. Arndt, V. Radko, and Y. Vasiliev (2011), Linking mantle plumes, large igneous provinces and environmental catastrophes, *Nature*, 477(7364), 312–316.
- Solomatov, V., P. Olson, and D. Stevenson (1993), Entrainment from a bed of particles by thermal convection, *Earth and planetary science letters*, 120(3), 387–393.
- Steinberger, B., and A. Calderwood (2006), Models of large-scale viscous flow in the earth’s mantle with constraints from mineral physics and surface observations, *Geophysical Journal International*, 167(3), 1461–1481.
- Steinberger, B., and R. Holme (2008), Mantle flow models with core-mantle boundary constraints and chemical heterogeneities in the lowermost mantle, *J. geophys. Res*, 113, 05,403.

- Stixrude, L., and C. Lithgow-Bertelloni (2012), Geophysics of chemical heterogeneity in the mantle, *Annual Review of Earth and Planetary Sciences*, *40*, 569–595.
- Tackley, P. (1996), Effects of strongly variable viscosity on three-dimensional compressible convection in planetary mantles, *Journal of geophysical research*, *101*(B2), 3311–3332.
- Tackley, P. (2002), Strong heterogeneity caused by deep mantle layering, *Geochem. Geophys. Geosyst.*, *3*(4), 1024.
- Tackley, P. (2011), Living dead slabs in 3-d: The dynamics of compositionally-stratified slabs entering a slab graveyard above the core-mantle boundary, *Physics of the Earth and Planetary Interiors*, *188*(3-4), 150–162.
- Tackley, P., and S. King (2003), Testing the tracer ratio method for modeling active compositional fields in mantle convection simulations, *Geochem. Geophys. Geosyst.*, *4*(4), 8302.
- Tackley, P. J. (2012), Dynamics and evolution of the deep mantle resulting from thermal, chemical, phase and melting effects, *Earth-Science Reviews*, *110*(1), 1–25.
- Tan, E., and M. Gurnis (2005), Metastable superplumes and mantle compressibility, *Geophys. Res. Lett.*, *32*(10.1029).
- Tan, E., and M. Gurnis (2007), Compressible thermochemical convection and application to lower mantle structures, *Journal of Geophysical Research: Solid Earth (1978–2012)*, *112*(B6).
- Tan, E., W. Leng, S. Zhong, and M. Gurnis (2011), On the location of plumes and lateral movement of thermochemical structures with high bulk modulus in the 3-d compressible mantle, *Geochemistry, Geophysics, Geosystems*, *12*(7).
- Thielmann, M., D. May, and B. Kaus (2014), Discretization errors in the hybrid finite element particle-in-cell method, *Pure and Applied Geophysics*, pp. 1–20.
- Torsvik, T., M. Smethurst, K. Burke, and B. Steinberger (2006), Large igneous provinces generated from the margins of the large low-velocity provinces in the deep mantle, *Geophysical Journal International*, *167*(3), 1447–1460.
- Trampert, J., F. Deschamps, J. Resovsky, and D. Yuen (2004), Probabilistic tomography maps chemical heterogeneities throughout the lower mantle, *Science*, *306*(5697), 853–856.

- Tsuchiya, T. (2011), Elasticity of subducted basaltic crust at the lower mantle pressures: Insights on the nature of deep mantle heterogeneity, *Physics of the Earth and Planetary Interiors*, 188(3), 142–149.
- Van der Hilst, R., S. Widiyantoro, K. Creager, T. McSweeney, et al. (1998), Deep subduction and aspherical variations in P-wave speed at the base of Earth’s mantle, *The Core-Mantle Boundary Region, Geodyn. Ser.*, 28, 5–20.
- van Keken, P. (2001), Cylindrical scaling for dynamical cooling models of the earth, *Physics of the Earth and Planetary Interiors*, 124(1), 119–130.
- van Keken, P., and C. Ballentine (1999), Dynamical models of mantle volatile evolution and the role of phase transitions and temperature-dependent rheology, *Journal of Geophysical Research: Solid Earth (1978–2012)*, 104(B4), 7137–7151.
- Van Keken, P., S. King, H. Schmeling, U. Christensen, D. Neumeister, and M. Doin (1997), A comparison of methods for the modeling of thermochemical convection, *JOURNAL OF GEOPHYSICAL RESEARCH-ALL SERIES-*, 102, 22–22.
- van Keken, P. E., E. H. Hauri, and C. J. Ballentine (2002), Mantle mixing: the generation, preservation, and destruction of chemical heterogeneity, *Annual Review of Earth and Planetary Sciences*, 30(1), 493–525.
- Wang, Z. (1999), The melting of al-bearing perovskite at the core–mantle boundary, *Physics of the earth and planetary interiors*, 115(3), 219–228.
- Xie, S., and P. J. Tackley (2004), Evolution of u-pb and sm-nd systems in numerical models of mantle convection and plate tectonics, *Journal of Geophysical Research: Solid Earth (1978–2012)*, 109(B11).
- Yamazaki, D., and S. Karato (2001), Some mineral physics constraints on the rheology and geothermal structure of earths lower mantle, *American Mineralogist*, 86(4), 385–391.
- Zerr, A., and R. Boehler (1994), Constraints on the melting temperature of the lower mantle from high-pressure experiments on mgo and magnesioüstite.
- Zhong, S., and B. Hager (2003), Entrainment of a dense layer by thermal plumes, *Geophysical Journal International*, 154(3), 666–676.
- Zindler, A., and S. Hart (1986), Chemical geodynamics, *Annual review of earth and planetary sciences*, 14, 493–571.

Erklärung

Hiermit versichere ich, dass ich die vorliegende Dissertation ohne unzulässige Hilfe Dritter und ohne Benutzung anderer als der angegebenen Literatur angefertigt wurde. Die Stellen der Arbeit, die anderen Werken wörtlich oder inhaltlich entnommen sind, wurden durch entsprechende Angaben der Quellen kenntlich gemacht. Diese Arbeit hat in gleicher oder ähnlicher Form noch keiner Prüfungsbehörde vorgelegen.